MRI MEASURES OF BRAIN INTEGRITY AND THEIR RELATION TO PROCESSING SPEED IN THE ELDERLY

by

Vijay Krishna Venkatraman

B.E., University of Madras, India, 2002

M.S., North Carolina A&T State University, 2004

Submitted to the Graduate Faculty of

the Swanson School of Engineering in partial fulfillment

of the requirements for the degree of

Doctor of Philosophy

University of Pittsburgh

2010

UNIVERSITY OF PITTSBURGH

SWANSON SCHOOL OF ENGINEERING

This dissertation was presented

by

Vijay Krishna Venkatraman

It was defended on

July 19th, 2010

and approved by

H.J.Aizenstein, M.D., Ph.D., Associate Professor, Departments of Psychiatry and Bioengineering

C.Rosano, M.D., M.P.H., Associate Professor, Department of Epidemiology

F.E.Boada, Ph.D., Associate Professor, Departments of Radiology and Bioengineering

G.D.Stetten, M.D., Ph.D., Professor, Departments of Radiology and Bioengineering

Dissertation Director: H.J.Aizenstein, M.D., Ph.D., Associate Professor, Departments of Psychiatry and Bioengineering

MRI MEASURES OF BRAIN INTEGRITY AND THEIR RELATION TO PROCESSING SPEED IN THE ELDERLY

Vijay Krishna Venkatraman, Ph.D.

University of Pittsburgh, 2010

A significant percentage of the elderly population experiences at least one geriatric disability. Previous studies have shown that geriatric disabilities are preceded by sub-clinical cognitive changes of aging and brain changes seen on magnetic resonance imaging (MRI). Decreased information processing speed has been identified as a common factor associated with age-related disabilities in gait, cognition, and mood. However, the current neurocognitive model of aging is incomplete; there remains uncertainty about the relationships between the different components of brain integrity and cognitive function. The goals of this dissertation are to characterize the relationships between different functional and structural MRI markers (for example: macro-structural, micro-structural, physiologic) with respect to cognitive aging and to improve the neuroimaging toolset for oldest old.

We studied the relationship between functional MRI markers, structural MRI markers, and information processing speed in a sample of twenty-five healthy elderly subjects. We found that recruitment of fronto-parietal brain areas was associated with higher performance. Also, greater structural damage (white matter integrity) was associated with lower activation in prefrontal and anterior cingulate regions. In the presence of underlying brain connectivity structural abnormalities, additional posterior parietal activation was found to be important for maintaining higher task performance.

We also studied MRI measures of brain structure in a sample of 277 community-dwelling older adults free from neurological diseases. This study used a set of neuroimage analysis pathways optimized for the MRI images and examined the macro- and micro-structural indices. The results indicate that both the macro- and micro-structural MRI indices may provide complementary information on neuroanatomical correlates of information processing speed. The micro-structural MRI indices of white matter integrity were found to be the strongest correlate of information processing speed in this sample.

While developing the image analysis pipelines for this dataset, we noticed that the diffusion tensor-imaging pathway was particularly sensitive to the approach of localizing the white matter tracts. We used both empirical and simulated datasets to confirm our hypothesis that the mean fractional anisotropy of the white matter tract is more sensitive to individual differences in the elderly when compared to a skeleton based approach.

TABLE OF CONTENTS

LIST OF TABLES

LIST OF FIGURES

PREFACE

I dedicate this dissertation to my parents and sister. My sincere gratitude goes to my mother, father, and sister for their continuous support and reinforcement without which this dissertation would not have been possible. I thank my uncles, aunts, cousins and grandmoms for their backing and reassurance during this process.

During my time as a graduate student at the University of Pittsburgh, I received help, advice, and support from many people. I especially thank Dr. Harvey Borovetz, Mrs. Joan Williamson, and Mrs. Lynette Spataro, all part of the Bioengineering Department, for guiding me through difficult times while changing between laboratories.

I also thank Dr. Howard Aizenstein and Dr. Caterina Rosano, my advisors, for providing a truly unique research environment. I appreciate their guidance and spontaneous support in times of difficulty and the numerous invaluable discussions that we have had. I thank Dr. George Stetten and Dr. Fernando Boada for serving on my dissertation committee and for guiding and motivating me through the process.

I deeply appreciate the past and present GPN lab members for their inspiration and support; Dr.Robert Tamburo (aka Rob) for his pep talks during our lunch together; Minjie and Meenal for being good fellow grad students; Dr.Lei Sheu for helping me understand statistics; Megan Nable for getting me started in the lab; and Dr. Miri Rabinowitz for her patience and encouragement.

Furthermore, I thank all the people who participated in these studies for their time and patience and all those individuals involved in data collection. Finally, thanks to my friends in Pittsburgh for their enjoyable company and special memories.

NOMENCLATURE USED

ADC	Apparent Diffusion Coefficient
ASL	Arterial Spin Labeling
AI	Atrophy index
ALP	Automatic Labeling Pathway
BOLD	Blood Oxygenation Level Dependent
CSF	Cerebrospinal fluid
DBM	Deformable-based Morphometry
DTI	Diffusion Tensor Imaging
DWI	Diffusion Weighted Imaging
DSST	Digit Symbol Substitution Test
sDSST	Digit Symbol Substitution Test in scanner
ECF	Executive Control Function
FLAIR	Fluid attenuated inversion recovery
FA	Fractional Anisotropy
fMRI	Functional Magnetic Resonance Imaging
GM	Gray Matter
MR	Magnetic Resonance
MRI	Magnetic Resonance Imaging
MP-RAGE	Magnetization Prepared Rapid Gradient Echo

MTI	Magnetization Transfer Imaging
MTR	Magnetization Transfer Ratio
MD	Mean Diffusivity
NAWM	Normal Appearing White Matter
PET	Positron Emission Tomography
ROI	Region of Interest
RPH	Relative Peak Height
TBM	Tensor-based Morphometry
TBSS	Tract-based spatial statistics
VBM	Voxel-based Morphometry
WM	White Matter
WMH	White Matter Hyperintensities

1.0 INTRODUCTION

The worldwide elderly population has experienced an increase. During the last 10 years, the percentage of individuals over 65+ in the United States has increased by 13%, and those over 85+ by 36% [1]. The growth of the aging population is projected to accelerate in the coming decades (36% increase for 65+ and 15% for 85+ in this decade). A significant percentage of the elderly population experiences at least one geriatric disability. The common disabilities of aging include impaired gait and balance, cognitive impairment, and geriatric depression, all of which significantly lower the individual's quality of life and present a greater risk of dementia, Alzheimer's disease, and mortality. A number of studies have shown that sub-clinical cognitive changes of aging and changes seen on magnetic resonance imaging (MRI) precede these disorders and disabilities.

Medical imaging has permitted clinicians and researchers to look beneath the surface of the skin to obtain critical diagnostic information and scientific insight. The most consistent cognitive change associated with non-demented related aging is a decrease in the information processing speed. This study used the digit symbol substitution test (DSST), a neuropsychological test; to measure the changes in information processing speed. Not only does a decreased speed of information processing emerge as a common factor associated with all of these age-related disabilities; but it is also identified as a marker for disruption of the central brain circuits responsible for gait, cognition, and mood.

1.1 MOTIVATION

The current neurocognitive model of cognitive aging is based on the direct and monotonical relationship between brain integrity and function. For example, as brain structural integrity deceases because of an unfavorable risk profile (hypertension, diabetes), neural activation decreases and information processing is impaired. The goals of this dissertation are to characterize the relationships between these different functional and structural MRI markers, with respect to cognitive aging, and to improve the neuroimaging toolset for oldest old (referring to the 79+ years old population). The study, therefore, has two goals: 1) to identify functional activation patterns during an information processing speed task 2) to better understand the relationship between structural MRI markers with the information processing speed.

Functional MR Imaging (fMRI) studies of cognitive aging have shown that older adults, unlike younger adults, have greater brain activation within the fronto-parietal regions and also activate additional regions. The first aim of this proposal was to identify the patterns of fMRI brain changes in relationship with DSST performance and with brain structural abnormalities (Aim 1, Hypotheses I and II). However, a significant minority of the oldest-old [‘resilient group’] still preserved their cognitive function, despite a high burden of macro-structural damage. In this proposal, we identified and understood their activation patterns (Aim1, Hypothesis III).

The second aim of this proposal was to understand the various MRI measures of brain structure in a large epidemiological dataset. Neuroimaging research in geriatrics has progressed rapidly over the past decade. There are now well-validated MRI pulse sequences for measuring gray matter (GM) volume, white matter (WM) volume, cerebrospinal fluid (CSF) volume, white matter hyperintensity volume, fractional anisotropy, apparent diffusion coefficient,

magnetization transfer ratio, functional activity, and resting-state functional connectivity. These measures provide complementary information about macro- and micro-structural brain integrity (Figure 1). Decreases in information processing speed are likely due to multiple inter-related neuropathological factors (including small and large vessel vascular changes, demyelination, and atrophy). To identify the specific changes associated with cognitive aging, we have chosen to use multiple MR imaging sequences. The second aim of this proposal is to characterize the specific micro- and macro-structural brain MRI markers associated with the information processing speed and to understand the interrelationship of the MRI markers (Aim 2, Hypotheses I, II and III). This understanding, which is essential for the development of better prevention and treatment strategies for cognitive aging in late-life, and is the focus of the current proposal using cross-sectional structural brain MR measures in the oldest old.

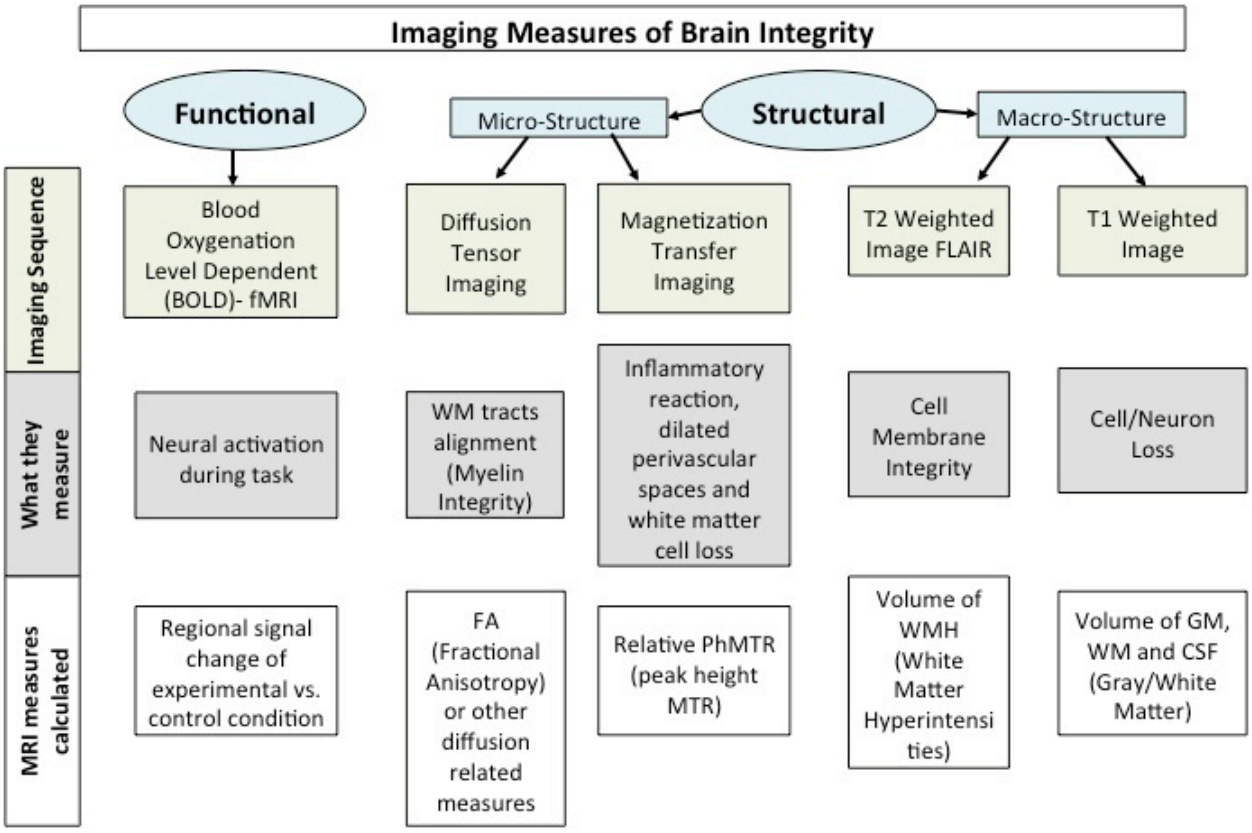

Figure 1. MRI Measures of Brain Integrity

In order to identify these brain changes and test our model, we needed to first develop a computational framework and toolset specific for our neuroimage analysis plan (Aim 3). In the elderly population, specific analysis was required for all the MRI sequences, including magnetization transfer and diffusion tensor imaging. The focus of this work was to compare diffusion tensor imaging (DTI) analysis methods within groups with various degree of macrostructural damage using empirical and simulated data in the oldest old.

1.2 SUMMARY OF GOALS AND HYPOTHESES

The goals of this dissertation are outlined below with each associated hypothesis:

Aim 1: Identify patterns of functional MRI brain changes associated with cognitive aging.

Hypothesis I: In older adults with greater task performance, the greater brain activation will be associated within task-related regions.

Hypothesis II: Greater brain structural abnormalities will be associated with lower activation within task-related regions.

Hypothesis III: Older adults above median WMH and greater performance [‘resilient group’] will recruit additional areas in the posterior parietal regions.

Aim 2: Identify and characterize the structural MRI indices associated with cognitive aging in the oldest old.

Hypothesis I: Micro- and macro-structural brain MRI markers are independently associated with DSST.

Hypothesis II: Micro- and macro-structural brain MRI markers correlate with each other.

Hypothesis III: Microstructural brain MRI markers are better predictor of DSST independent of other MRI markers and factors.

Aim 3: Develop and improve neuroimaging toolset for MRI imaging contrasts.

Objective I: Compare diffusion tensor imaging (DTI) analysis methods within groups with various degrees of macro-structural damage using empirical and simulated data in the oldest old.

1.3 DESCRIPTION OF CHAPTERS

Including the current chapter, this dissertation consists of 10 chapters and a bibliography.

Chapter 2.0	Background
Chapter 3.0	Cognitive Aging and its Theories
Chapter 4.0	MRI Sequences
Chapter 5.0	MRI Image Analysis
Chapter 6.0	MRI Research in Cognitive Aging
Chapter 7.0	Methods
Chapter 8.0	Results
Chapter 9.0	Discussion
Chapter 10.0	Conclusions and Future Work

2.0 BACKGROUND

The elderly population has experienced a worldwide increase; this is one of the most important demographic changes affecting societies throughout the global community. With the growth of the elderly population, policy makers, families, and health care providers face more challenges in meeting the needs of aging individuals [1]. In 2000, 420 million people in the world were 65 and older, or 7 percent of the world's population. The 65+ populations are projected to increase to 974 million by 2030. Most of the world's older population, 59 percent, lived in developing countries in 2000. By 2030, projections indicate that the proportions will rise to over 70 percent. By 2050, that number is expected to be close to 2 billion. At that time, older adults will outnumber children 14 and under for the first time in history.

Table 1. Aging Population worldwide

	0-14 years		**65+ years**		**80+ years**	
	2010	***2050***	***2010***	***2050***	***2010***	***2050***
World	26.9	19.6	7.6	16.2	1.5	4.3
Africa	40.3	27.3	3.4	7.1	0.4	1.1
Asia	26.2	17.9	6.7	17.3	1.1	4.4
Europe	15.4	15	16.3	27.4	4.2	9.6
South America	26.9	16.7	7	19.8	1.5	5.6
North America	19.8	16.9	13.1	22	3.8	8

Table 1 shows the increasing trends worldwide according to the United Nations: World Population Prospects- Revision 2008 [2]. In terms of proportions from age 65 and older, Europe and the Americas still have the highest proportion among major world regions and will continue to do so as the 21st century progresses. Based on a 2009 report by the Administration on Aging of U.S Department of Health and Human Services for the United States of America [1], the older population (65+) numbered 38.9 million in 2008; this shows an increase from 4.5 million in 1998. The 65+ older population increased by 13% since 1998, compared to an increase of 12.4% for the under-65 population. Since 1900, the percentage of Americans 65+ has tripled (from 4.1% in 1990 to 12.8% in 2008), and the number has increased more than twelve times (from 3.1 million to 38.9 million). The elderly continue to live longer. In 2008, the 65-74 age group (20.1 million) was over 9 times larger than in 1900. In contrast, the 75 - 84 age group (13 million) was 17 times larger, and the 85+ age group (5.7 million) was 47 times larger. This trend is projected to accelerate in the coming decades (36% increase for 65+ and 15% for 85+ in this decade). The population 65+ will increase from 35 million in 2000 to 40 million in 2010 (a 15% increase) and then to 55 million in 2020 (a 36% increase for that decade). By 2030, there will be about 72.1 million older persons, almost twice their number in 2008. The number of people ages 65+ is expected to grow to 19.3% of the population by 2030. The 85+ population has a projected increase to 6.6 million in 2020 from 5.8 million in 2010. Reductions in mortality during the 20th century have increased life expectancy. However, a healthy 65-year-old and a frail 90-year-old have quite different needs for health care, housing, and assistance with the functional activities of daily life. Recognizing this difference is important for researchers studying the 65 years and older population. As in most countries of the world, older women outnumber older men in the United States; this percentage increases with age.

In minority populations, the number of elderly is projected to increase from 8 million in 2010 to 12.9 million in 2020 (23.6% rise). Between 2008 and 2030, the 65+ populations are projected to increase 172% for older minorities, including Hispanics (224%), African-Americans (120%), Native Americans, Eskimos, and Aleuts (153%), and Asians and Pacific Islanders (199%). As the older population grows larger, it will also grow more diverse, reflecting the demographic changes in the overall U.S. population.

In 2008, 39.1% of non-institutionalized older persons assessed their health as excellent or very good (compared to 60.7% for all persons ages 18 and older). Researchers predict that increased longevity is likely to have implications for the financing of our health care systems. In 2008, older consumers averaged an out-of-pocket health care expenditure of $4,605, an increase of 57% since 1998. In contrast, the total population spent considerably less on health care, averaging only $2,976 in out-of-pocket costs. Older Americans spent 12.5% of their total expenditures on health, more than twice the proportion spent by all consumers (5.9%). The social and economic implications of this aging population loom as significant concerns for policy makers, the private sector, and all individuals. Research on genetic, biological, and physiological aspects of aging is likely to change the future for the older population. In the medical and public health arenas, research to understand chronic diseases, such as diabetes and Alzheimer's disease, may produce significant improvements for treatment and prevention. Arthritis, hypertension, heart disease, diabetes, and respiratory disorders are some of the leading causes of activity limitations among older people. According to the 2006 Census on the 65+ population in the United States [3], about 80% of older adults have at least one chronic health condition and 50% have at least two. This leads to a significant percentage of population with at least one geriatric disability.

2.1 GERIATRIC SYNDROMES

Geriatric Syndromes, groups of specific signs and symptoms that occur more often in the elderly, can affect patient morbidity and mortality. Normal aging changes, multiple co-morbidities, and adverse effects of therapeutic interventions contribute to the development of Geriatric Syndromes. Aristotle explained old age as a period when the body's heat dissipates and is no longer able to provide energy and balance; the loss of inward heat depressed the spirit, caused illness, and decreased strength resulting in human beings losing their passion for life and succumbing to death [4]. Because Geriatric Syndromes can cause difficulty in functioning, they increase the risk of death. Geriatricians have embraced the term ''Geriatric Syndrome,'' using it extensively to highlight the unique features of common health conditions in older people. Geriatric Syndromes, such as delirium, falls, incontinence, and frailty, are highly prevalent, multi-factorial syndromes associated with substantial morbidity and poor outcomes [5].

The following lists and summarizes the Geriatric Syndromes [6]:

Dementia, the most common cause of mental decline in old age, is a general term used to describe a significant decline in two or more areas of cognitive functioning. These cognitive changes are different from the benign changes associated with aging such as memory changes due to slowing in information processing.

Delirium has appeared in the medical literature for more than two thousand years, yet remains under recognized. Clinicians often define delirium as an acute confusional state.

Urinary Incontinence is a multi-factorial syndrome produced by a combination of pathology, age-related changes, and comorbid conditions.

Falls: A fall is considered to have occurred when a person comes to rest inadvertently on the ground or a lower level; it is one of the most common geriatric syndromes threatening the independence of older persons.

Gait Disturbances: Limitations in walking increases with age, causing older adults to have difficulty in walking or to require the assistance of another person or special equipment to walk. The age-related gait changes are most apparent past age 75 or 80; most gait disorders appear in connection with other underlying diseases.

Dizziness: In older adults, the prevalence of dizziness ranges from 13% to 38% and accounts for an estimated 7 million clinic visits.

Syncope: Approximately 80% of the patients hospitalized for syncope are 65 or older. Syncope is a sudden, transient loss of postural tone and consciousness not due to trauma; it usually has a spontaneous full recovery.

Hearing impairment: Hearing loss is the fourth most common chronic disease among the elderly population. Hearing impairment is often assumed to be benign, but it has profound effects on the individual's quality of life.

Visual impairment, which is defined as visual acuity less than 20/40, increases exponentially with age, thereby affecting 20% to 30% of the population 75 years and older.

Osteoporosis and Osteomalacia: Osteoporosis develops in older adults when the normal processes of bone formation and resorption become uncoupled or unbalanced, resulting in bone loss. Osteomalacia, an impairment of bone mineralization, is less common than osteoporosis.

Malnutrition: Older adults suffer a burden of malnutrition that spans the spectrum from under- to over nutrition. It affects many of the chronic disease processes that afflict older persons.

Eating and Feeding Problems: Normal aging and diseases common in the elderly affect swallowing, an important and complex task.

Pressure Ulcers: A pressure ulcer is any lesion caused by unrelieved pressure when it is compressed between a bony prominence and external surface over a prolonged period of time. This pressure damages the underlying soft tissue. Approximately one million people in the United States, many of whom are elderly, have this common but serious problem.

Sleep Problems: Older adults exhibit a high prevalence of sleeping problems. The elderly who live in community-dwellings often complain of difficulty falling asleep (37% of the sample), nighttime awakening (29%), and early morning awakening (19%).

Based on a review of the literature [5], four shared risk factors - older age, baseline cognitive impairment, baseline functional impairment, and impaired mobility- were identified across five common geriatric syndromes (pressure ulcers, incontinence, falls, functional decline, and delirium). Apart from these geriatric syndromes, the older adults experienced psychiatric disorders such as depression, substance abuse, mental retardation and disorders such as mood, anxiety, and personality. Other chronic illness, including hypertension, cardiovascular disorders, neurologic disorders and other health concerns contribute towards the Geriatric Syndromes.

Understanding basic mechanisms involved in Geriatric Syndromes is critical for advancing research and developing targeted therapeutic options. National strategic initiatives are then needed to overcome impediments and to achieve clinical, research, and policy advances that will improve the quality of life for older persons.

2.2 BRAIN CHANGES IN AGING

Because the most common condition that affects the brain is aging, knowledge of age-related changes in the brain is essential. However, not all the older adults age with similar patterns [7]. First, age-related abnormalities do not occur in all the older adults. Some older adults experience successful aging by having a perfectly healthy brain and minimal physiologic loss that is indistinguishable from that of a young person. The normal aging is defined as the presence of disturbance of physiologic functions (such as hypertension) without any observable neurologic symptoms. Secondly, the age-related changes seen on conventional imaging methods (such as brain lesions) do not always have functional consequences; those individuals with such changes are still capable of having a normal, independent life. Thirdly, normal aging and neurodegenerative disorders, it may be difficult to distinguish between.

The abnormalities associated with these conditions may only differ in pattern or by the degree of abnormality in relation to a patient's age; making the conditions indiscernible, then, is problematic [8]. Another phenomenon that complicates distinguishing these conditions is that different conditions co-exist in the elderly. While it may be impossible to separate the abnormalities in terms of their origin, to do so emerges as an important challenge.

2.2.1 Structural Changes

Brain volume is one of the obvious aspects of age-related changes of brain structure. Postmortem studies indicate that with aging, the weight and volume of the brain shrink at a slow but persistent rate of about 2% per decade [9]. This atrophy may reflect neuronal death and/or neuronal atrophy due to dendritic "debranching" and synaptic loss [9]. The in-vivo MRI studies

[10] also showed significant negative correlations (r=-0.41) between overall brain volume and age. The age-related atrophy affects some brain regions more than others (for example, pre-frontal cortex (-0.47) and parietal (-0.29) cortices).

Age-related atrophy in white matter is probably due to a loss of myelin. Volumetric MRI analyses show white matter atrophy primarily in the pre-frontal cortex regions [10]. The difference is greater in the parietal cortex when compared to the pre-frontal regions for white matter atrophy. In an MRI image the white matter hyperintensities (WMHs) reflect a reduction in white matter density [11] and result from a variety of vascular and nonvascular causes.

Aging is also associated with an accumulation of certain chemicals and pathological structures inside or outside the brain neurons. Age-related aggregation of iron increases the chemical processing of the cytotoxic effects of free radicals leading to changes [12]. The gross accumulation of amyloid plaques and neurofibrillary tangles are other histologic features also present in a normal aging brain [13]. Because age-related structural changes are due to different mechanisms, it is not always easy to identify the primary source of the change.

2.2.2 Functional Changes

Age-related changes in brain function include alterations in neurochemistry, blood flow, and the metabolism of oxygen and glucose. Changes in the number of receptors and/or concentration of enzymes and neurotransmitters have been reliably observed for serotonin, acetylcholine, and dopamine [14]. Serotonin function is associated with mood regulation; the depressive mood in older adults could contribute to their cognitive deficits [15]. Changes in cholinergic and dopaminergic function could underly age-related deficits in memory and frontal functions [16]. Because age-related functional changes could be interpreted differently based on various

phenomena or mechanisms, further studies are required to better understand the underlying mechanisms.

3.0 COGNITIVE AGING AND ITS THEORIES

Cognitive aging involves the study of age-related decline in cognitive functions like visual perception and attention, language/semantic processing, maintenance and manipulation, implicit memory, episodic memory and priming, and working memory and executive functions [17]. Cognitive aging encompasses a diversity of topics since in its broadest sense it refers to the effects of aging on all aspects of cognition, ranging from pathological or abnormal cognition to social cognition. Using behavioral methodologies cognitive psychologists have focused on measuring and explaining the age-related decline of cognitive functions in older individuals. This section uses functional neuroimaging studies to illustrate the effects of aging in the areas of (a) visual perception and attention, (b) episodic memory and priming, and (c) working memory and executive functions. In this section, we also discuss the four major cognitive aging theories, which are usually interpreted in terms of reduced sensory resources, attentional resources, processing speed, or inhibitory control.

3.1 COGNITIVE DOMAINS

Here are few examples of cognitive domains and summary of results from imaging studies of each cognitive domain [17]:

3.1.1 Visual Perception and Attention

Traditionally, psychologists have paid little attention to age-related changes in sensory and perceptual processes. Newer studies, however, have shown evidence of strong correlations between age-related sensory/perceptual decline and cognitive decline [18]. Three scenarios explain this: (a) perceptual decline causes cognitive decline; (b) cognitive decline causes perceptual decline; and (c) perceptual and cognitive decline have a common cause. Studies of perceptual processes have shown age-related reductions in activation in the visual cortex regions, as well as in more anterior regions of the ventral pathway [19]. Other studies have shown increases in more anterior brain regions such as the prefrontal cortex [20]. The sensory deficits are primarily due to the decline of eye structure, including the cornea, iris, and lens [21]. Although aging does not markedly alter the visual pathways, but it does cause deficits found in such higher-order visual processes as peripheral vision [22].

3.1.2 Episodic Memory and Priming

Episodic memory refers to the encoding and retrieval of information about personally experienced past events [23]. Priming occurs when a past experience facilitates cognitive performance in the absence of a conscious intention [24]. While the effects of aging are

considerable on episodic memory, they are negligible in priming. A few forms of episodic memory are affected more than others [25], but priming tests occasionally show significant age effects [26]. Age-related episodic memory deficits may reflect difficulties during encoding, retrieval, or both.

3.1.3 Working Memory and Executive Functions

The commonly used model for working memory consists of four components [27] – a central executive and three slave systems (the phonological loop, the visuo-spatial sketchpad, and the episodic buffer). The central executive, assumed to have a supervisory role, controls the flow of information from and to its slave systems; the slave systems maintain verbal or visuo-spatial information for short- and long- term memory. A meta-analysis study [28] indicated that the effect size of aging is -0.31 for an auditory digit span task but -0.81 for tasks involving executive operations. Working memory involves a composite of cognitive operations, including maintenance of information over a brief delay, manipulation and monitoring of information, and executive processes involved in problem solving and reasoning tasks. The effects of aging on brain activity associated with executive functions have been measured with tasks that tap such processes as inhibitory control, task switching, dual-task performance, and reasoning. The most consistent finding across studies shows age-related increases in prefrontal cortex activation [29].

3.2 COGNITIVE AGING THEORIES

We focused on the considerable age-related differences during various cognitive tasks. Here we will discuss the cognitive aging theories, which were originally developed to account for age-related differences in behavior and to explain deficits in cognition. Specifically, we will emphasize four major cognitive aging theories.

3.2.1 Sensory Deficit Theory

According to this theory, age-related deficits in sensory processing play a major role in age-related cognitive decline [18]. Consistent with this view, older adults show considerable deficits in basic sensory functioning, including simple vision and auditory processing. The findings of strong correlations between age-related differences in sensory and cognitive measures provide evidence supporting the sensory deficit theory [30].

3.2.2 Resources Deficit Theory

A limited supply of attentional resources fuel cognitive processes [31]. The resource deficit theory is derived from the environmental support hypothesis [32], which predicts that age-related differences should be smaller when a task is accompanied by a supportive environment. That the memory performance of older adults resembles that of young adults under divided attention conditions substantiates this theory[33]. In addition, the resources deficit theory gains validity when younger adults, faced with reduced attentional resources, show cognitive deficits that resemble those of older adults [33].

3.2.3 Speed Deficit Theory

One of the most popular cognitive aging theories is that the cognitive deficits of older adults reflect a general reduction in the speed of their cognitive processes [34, 35]. Lower processing speed is assumed to impair cognitive performance because of two mechanisms: the time required by early operations reduces the time available for later operations (limited time mechanism), and the products of early operations are lost or irrelevant by the time later operations are completed (simultaneity mechanism). The speed deficit theory is supported by evidence that processing speed declines steadily with age, that this slowing shares considerable variance with age-related deficits in cognitive measures, and thus processing speed is a strong mediator of cognitive decline [35, 36].

3.2.4 Inhibition Deficit Theory

A fourth theory of cognitive aging is the inhibition deficit theory, which attributes age-related cognitive deficits to a decline in the inhibitory control of working-memory contents [25]. Such control involves three functions: 1) the stopping of partially activated goal-irrelevant information from entering working memory (access function); 2) the lessening of the activation of information that is no longer relevant to current task (suppression function); and 3) the blocking of strong inappropriate responses, thereby allowing weak appropriate responses (restraint function). When this control fails, goal-irrelevant information gains access to working memory and impairs the working-memory operations [25].

3.3 PROCESSING SPEED

In this section, we will discuss the concept of processing speed and the various measurements of processing speed. This study uses processing speed measured using the digit symbol substitution test as a measure of cognitive changes due to aging.

Processing speed is the maximum rate at which elementary cognitive operations can be executed. It is considered a general-purpose resource that limits performance on higher-level operations [37]. An important aspect in studies of the psychology of cognitive differences is the speed with which mental processes can be executed. Studies [38] have demostrated that with increasing age, individuals undergo changes in the speed with which they process and respond to information; these changes slow down all aspects of cognitive domains. The rate at which information can be processed and the rate at which it becomes obsolete or unavailable are the two critical factors affecting cognitive operations. If steps are carried out too slowly, the products of earlier operations may be lost or no longer relevant by the time later operations occur. The speed at which basic operations are completed also determines the amount of simultaneous active information available for higher-level processes. Many higher-order processes (for example, language processing) require multiple sources of information to do simultaneous processing. If processing is too slow, not all information may be available at the time it is needed and, therefore, the subject may be forced to repeat the processing steps. Changes in processing speed, not just the time required to complete the task, disturb the internal dynamics of the overall processing system.

Researchers have suggested that two distinct mechanisms are responsible for the relation between speed and cognition [35]. The limited time mechanism is based on the assumption that the execution of early operations occupies the available time and greatly restricts later

operation's performance. With simple cognitive tasks, this mechanism can represent the speed of processing as the primary indicator of individual differences. Thus, "if processing is slow the operations may not be completed" [39]. In more complex tasks, the mechanism affects the number of minor operations the individual can carry out in the available time. The second hypothesized mechanism, called "simultaneity mechanism," proposes that slow early processing reduces the amount of simultaneous available information needed for higher level processing. The later operations may not receive the necessary information for subsequent processing, i.e. "if the processing is too slow, then not all relevant information will be available when needed, leading to impairments of critical operations that could result in either a high rate of errors or time-consuming repetitions of critical operations" [39]. The simultaneity mechanism assumes that the quality or quantity of available information is reduced over time because of decay or displacement of information. The age-associated effects in this mechanism are due to a slower speed of activation of information than the rate of information loss [40].

3.3.1 Changes in Processing Speed with Age

Early cognitive studies attributed the generalized slowing of information processing as the common source of many of the cognitive decrements associated with normal aging [35]. Research has suggested that age decrements in working memory arise partly from a slowing of information processing [41]. Slowing with age is "one of the best-documented and least controversial behavioral phenomena of aging" [35]. Other superlatives reinforce age-related slowing as "the most striking," "the most pervasive," and "the most reliable" phenomenon in the psychology of aging [36]. The processing speed is considered one of the major causes of age-related declines in other cognitive functions. Studies [35, 36] have reported a median correlation

of 0.45 between age and measures of speed across a wide range of behavioral activities. Both cross-sectional and longitudinal comparison have found age and a variety of perceptual speed tests from psychometric batteries to be negatively and linearly related [42]. Some recent models show processing speed as one domain of cognition that ages alongside others, with no speculation of underlying cause for age-related changes [43]. Others studies have also shown the same results [44]. Moreover, the processing speed's attenuating influence on age-cognitive ability is less when using longitudinal data [45]. The age-related slowing occurs with any of the processing speed tasks: psychometric, cognitive– experimental, or psychophysical. Studies [46] have described speed of information processing as a "fundamental property of the nervous system," one that provides a foundation for the efficient implementation of other cognitive functions. Within the hierarchical structure of cognitive abilities and within cognitive aging, some [47] have suggested processing speed as a biomarker of cognitive aging.

3.3.2 Measurement of Processing Speed

The processing speed tasks typically examine how efficiently people can complete a series of items with simple cognitive content. The measurement of processing speed in humans is examined at different levels of description [48]. First, Processing speed is assessed at the molar level using psychometric tests such as the Digit Symbol-Coding and Symbol Search subtests of the Wechsler Intelligence Scales. In these tests (for example, Digit Symbol-Coding), each item requires a simple decision; given unlimited time, most people would correctly complete all items. In the digit symbol coding, the subject enters a simple symbol below each number in a long series; the look-up code for each number is printed on the same page as the test items. Scores are based on the number of items completed correctly in the time given. The second and

third levels of description in processing speed are assessed using tasks derived from cognitive experimental psychology and psychophysics, respectively. Experimental psychology uses simple and choice reaction time tasks to assess processing speed, while psychophysics uses inspection time to assess processing speed. These measures have a significant correlation with higher-level cognitive functions [49].

Several criteria [50] are used for assessing processing speed; one of the primary criterion is “most of the individual differences in performance are attributable to how quickly one can carry out the relevant operations rather than to variations in amount of knowledge or in other cognitive abilities.” Some of the measures do not exclusively represent particular processes, but they also reflect “duration of relevant cognitive operations.” Researchers have relied on various combinations of seven measures designed to assess processing speed [35]. One measure is a speeded decoding test (Digit Symbol Substitution Test; DSST) [51]. Two perceptual speed measures require comparisons of pairs of letters (Letter Comparison) or pairs of line patterns (Pattern Comparison). The two available paper-and-pencil tests [51] involve minimal cognitive operations, but with similar stimulus and response requirements to the perceptual speed tests. Researchers have also used two computer-administered reaction time tasks (Digit Symbol and Digit Digit) based on the DSST to assess processing speed. Studies [35, 36, 52] have reported moderate to large age-relations for all these measures and “respectable” test-retest reliabilities. Within samples of 240 and 131 participants ranging in age from 19 to 82 and 17 to 79, respectively, the test-retest correlations were 0.93 and 0.89 for Digit Symbol reaction time, and 0.61 and 0.69 for Digit Digit reaction time. Performance on the Digit Symbol Test, one of the subtests in the widely used Weschler Adult Intelligence Scale (WAIS) intelligence battery, is one of the best psychological correlates of chronological age currently available [51].

3.3.3 Digit Symbol Substitution Test

The Digit Symbol Substitution Test (DSST) is a test of psychomotor performance. To perform successfully, it requires incidental memory, perceptual organization, visuo-motor coordination, and selective attention to filter out irrelevant information (for example, symbols that may look alike). The pencil and paper version of the DSST is frequently employed in epidemiological studies of older adults [53].

The subject is given a key grid of numbers and matching symbols and a test section with numbers and empty boxes. The test consists of filling as many empty boxes as possible with a symbol matching each number within a 90 seconds time limit; and the score is the number of correct number–symbol matches. The strategy to solve the DSST consists of sequential encoding and retrieval of numbers and matching symbols. First, the number in the test section is encoded in short-term memory and temporarily stored. Then, while the subject visually scans the key grid to search for the number–symbol match, the number in the short-term memory is repeatedly retrieved and compared with the numbers of the key grid. Once the number is recognized, the matching symbol is encoded in short-term memory. Finally, the attention is turned toward the test section again, and the symbol is retrieved from short-term memory and copied below the number. Incidental memory, perceptual organization, visuomotor coordination, and selective attention are important factors that determine the final score [35, 51]. The ability to filter out irrelevant information (for example, symbols that may look alike) also influences performance.

3.4 COGNITIVE NEUROSCIENCE OF AGING

The goal of cognitive neuroscience of aging is to reveal the relationships between age-related changes in the brain and age-related changes in cognition. There are three basic approaches (Figure 2, modified from [54]). First, the neuropsychological approach compares cognitive changes in individuals with healthy aging and in patients with brain damage due to degenerative disorders. Second, the correlational approach associates neural measures to independently obtained cognitive measures. The activation imaging approach, the third approach, measures the brain activity in young and older adults during cognitive performance [54].

In this work, we have used a combination of correlational and activation-imaging approaches to study the effects of structural damage while performing a DSST task using functional MRI imaging. We also used the correlational approach to study the interrelationship of structural MRI markers of the aging brain.

3.4.1 Neuropsychological approach

This approach is generally used for comparing neurocognitive changes in healthy aging to those associated with brain damage [55]. In this approach, inferences about neural mechanisms are based on comparisons between healthy aging and brain-damaged populations. If patients with damaged brains have similar brain regions to the ones displaced by elderly adults, then age-related cognitive deficits may be related to those specific regions. This approach helps identify age effects on brain regions that are necessary for cognitive performance and clarifies the neural mechanisms (such as dopamine deficits) of age-related neural decline. This approach cannot easily identify compensatory changes in the aging brain.

3.4.2 Correlational approach

This approach [11, 56] involves associating a neural measure, such as structural imaging measures, to a cognitive measure, such as processing speed. The relationship between these cognitive tests and the anatomical and functional integrity of the brain region of interest is uncertain. The studies using direct measures, such as neurochemical imaging, can provide a more direct link between cerebral and cognitive aging. This approach uses neural measures that are indicative of the neural mechanisms underlying age-related cognitive changes and likely reflect neurogenic changes rather than psychogenic changes. The weakness of this approach is that the neural measures are only an indirect indicator of age-related changes in cognitive performance and cannot be used to easily identify compensatory changes in the aging brain.

3.4.3 Activation imaging approach

This approach assesses the effects of aging on brain activity and cognitive performance in direct relation to each other. A variety of cognitive functions has investigated this approach [57]. The compensation mechanism is explained as greater activity in older adults, whereas generally the lower activity is generally attributed to deficits in neurocognitive processing. In the older adults, Hemispheric Asymmetry Reduction in Older Adults (HAROLD) model [58] and recent studies [59, 60] emerge as evidence to support the compensation mechanism. An alternative view of age-related asymmetry reductions suggests that it may reflect age-related difficulty in engaging specialized neural mechanisms resulting in poorer performance [18]. Other discoveries about aging are frontal compensation [11] and default network alterations [61]. The neural-based theories in cognitive aging involve increased noise [62], proactive versus reactive control [63],

compensation-related utilization of neural circuits hypothesis (CRUNCH) [64], and the Scaffolding Theory of Aging and Cognition (STAC) [65]. Recent work has proposed evidence of favoring plasticity and compensation [66]. The strengths of this current approach comes from understanding that age-related changes in brain activity are directly related to age-related changes in cognitive performance and can be used to detect compensatory changes in the aging brain. However, because the brain activity measures are farther away from the neural mechanisms' underlying age-related cognitive changes, as they are not direct measures as used in the correlational approach. The age-related changes in brain activity may reflect neurogenic as well as psychogenic changes.

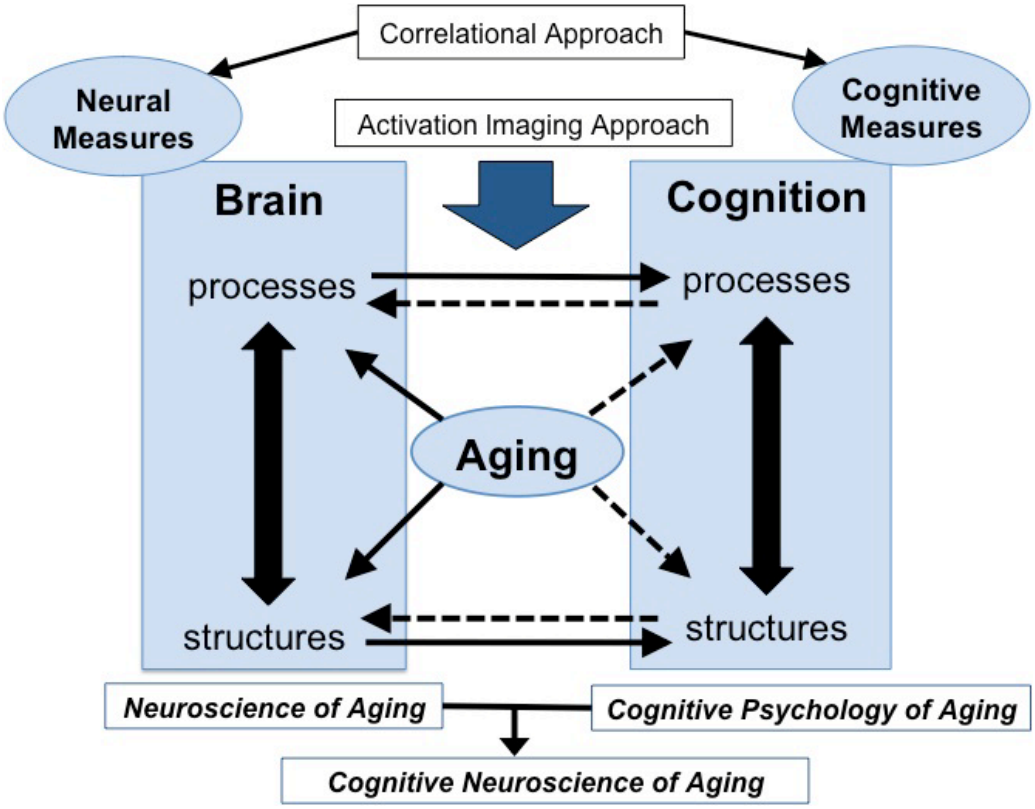

Figure 2. Cognitive Neuroscience of Aging (adapted from Cabeza et al., 2004)

4.0 MRI SEQUENCES

4.1 INTRODUCTION TO MR IMAGING

In 2003, Paul C Lauterbur and Peter Mansfield received the Nobel Prize in Medicine for their work implementing a practical method of Magnetic Resonance Imaging (MRI). MRI has been used for about 30 years in various clinical applications. MR imaging revolutionized in-vivo human brain imaging, allowing for remarkably clear high-resolution images of the brain. Magnetic Resonance Imaging is based on the concept of nuclear magnetic resonance (NMR), which measures the signals coming from the nuclei in response to radio waves with the same frequency. A brief synopsis of magnetic resonance physics is provided below [67, 68].

The behavior of biological protons in the presence of a magnetic field is important for the concept of MRI. The protons have a magnetic axis whose orientation is random in nature. The presence of an external magnetic field aligns the protons' spin axis along the applied magnetic field, causing the protons to continue to spin around the axis (called precession). The spinning protons give rise to secondary magnetic fields or magnetization. The average magnetization of the protons along the direction of the magnetic field is called the longitudinal net magnetization. This net magnetization is smaller than the main magnetic field in order to measure the net tissue magnetization to form an MRI image; a radio pulse (excitation pulse) is used to disturb the equilibrium. A radio pulse of appropriate frequency rotates this longitudinal magnetization away

from equilibrium into the transverse plane, producing transverse magnetization. With the radio pulses, the MR signal is obtained, but locating the source of the MR signals is a complex problem.

To produce useful MRI images requires a variety of techniques used in combination to resolve the collection of radio signals in three dimensions. Additional magnetic field gradients are used to determine the location of the sources. The gradients create variations in the magnetic field, causing the protons to spin slower or faster depending on their location. These gradients are produced by gradient coils within the bore of the main magnet and are applied in three orthogonal axes that, at different times, allow three-dimensional localization of MR signal origin. There are three major types of gradients:

Slice or Section Selection: Slice selection gradient is applied in three dimensions (Gx, Gy, Gz) to select the required slice with the help of the shaped RF pulse.

Frequency Encoding: This makes the oscillation frequency of the MR signal linearly dependent on its spatial origin along a particular axis. The process of encoding the spatial location is called Frequency Encoding and the gradient is called Frequency-Encoding Gradient or Readout Gradient.

Phase Encoding: The Phase-Encoding Gradient is used to map the location of the sources of MR signals based not on their frequency at readout, but on their phase. This gradient is applied along the phase encoding axis at different strengths.

The combination of spatial encoding and the Fourier transform data provide the necessary information for obtaining the MR image using image reconstruction. The relaxation time (T1) is a property of a tissue at a given magnetic field strength. With each excitation pulse, the longitudinal magnetization begins to recover before reducing to a steady state after several

pulses. The time between repetitions of the excitation pulse is called the repetition time (TR). The repetition time (TR) and flip angle are the two major parameters varied to control the T1 weighting of an image. The transverse magnetization decays at the rate of T2 relaxation time. The delay between the creation of the transverse magnetization and the measurement of the resulting echo is called echo time (TE). The images where signal intensity is largely dependent on T2 differences (or TE values) are called T2-weighted images.

An MR pulsing sequence involves the acquisition of multiple spin echo signals. For a 256 x 192 image (pixels in the frequency direction x pixels in the phase direction) with two excitations, 384 separate spin echoes are acquired. During the time between acquisitions, the longitudinal magnetization "relaxes" along the z-axis. Longitudinal recovery is identical to the process of initial magnetization when the body was first placed in the magnet and occurs between spin echo acquisitions. In the first step of a spin echo pulsing sequence, a 90° RF pulse flips the existing longitudinal magnetization from the z-axis 90° into the transverse xy-plane. Whenever transverse magnetization is present, it rotates at the Larmor frequency and induces an oscillating MR signal in a receiver coil. The magnitude of the transverse magnetization after the 90° pulse is essentially equal to the magnitude of the longitudinal magnetization which had recovered during the interval between 90^0 pulses. This interval, called the "repetition time" (TR), is one of the programmable sequence parameters. In the process of flipping the longitudinal magnetization 90° into the transverse orientation, the longitudinal component of magnetization is totally lost and must be allowed to recover before another signal can be generated. The amount of longitudinal magnetization that is recovered depends on the rate of recovery (T1) and the time allowed for recovery to occur, which is the TR. The magnitude of the signal detected depends not only on longitudinal recovery between repetitions but also on how well the signal persists, or

alternatively, on how slowly the transverse magnetization decays from its initial maximum value. This decay depends on the T2 of the substance. The amount of time allowed for decay to occur (the time between the initial 90° RF pulse and the detection of the spin echo) is called the echo delay time (TE) and is another programmable sequence parameter.

The intensity of the MR signal increases as hydrogen density and T2 increase as T1 decreases. It should also be noted that T1 and T2 influences are both subject to TR and TE, the programmable sequence parameters. Thus, the effect of the T1 and T2 relaxation times of the substance on signal intensity is subject to the specific values of TR and TE selected, before the image is acquired. The various pulse sequences are designed based on TR, TE, and other parameters to obtain the necessary contrast variation in the MRI image. The MRI image can have different artifacts, including the following: motion-induced artifacts, susceptibility, wrap around, edge artifacts (partial-volume, chemical shift edge, truncation, relaxation), ghost artifacts, altered signal intensity, stripes and image distortion. The different pulse sequences used in imaging sequences are T2*, Echo Planar Imaging used in Blood Oxygenation Level Dependent (BOLD) fMRI; Fluid-attenuated inversion-recovery imaging (FLAIR); Diffusion Weighted Imaging; and Magnetization Transfer Imaging; these, are variations obtained from the optimization of the various parameters explained above.

The structural MRI is useful for studying the patterns of neuroanatomical changes in geriatric research [17]. The structural MRI, which is important for studies in normal aging, late-life depression, dementia, Alzheimer's disease, and other cognitive disorders, examines how age-associated changes in neuroanatomy are associated with specific age-related changes, such as the changes in cognition. In the 1960 s and 1970 s, a number of investigators showed that not only could MRI be used to visualize neuroanatomy and structural pathology, but by appropriately

tuning the MRI contrast, MR could also be used to visualize the dynamic changes in blood oxygenation across the brain; this was the beginning of functional MRI. Over the subsequent years, a number of studies have shown that this BOLD signal could be used to map brain activity on a variety of cognitive and affective tasks. Functional MRI has been a major advance for the fields of cognitive and affective neuroscience by allowing investigators to test theories of the underlying neural pathways controlling cognitive and emotional processes [17]. This approach is often referred to as 'human brain mapping.' In addition to studying 'normal' human brain functions, fMRI can also be used to characterize the functional activation patterns in patient groups.

There has been a tremendous increase in the use of MRI (functional and structural) in studying the brain [69]. The neuroimaging studies have provided insight into normal aging and the neuropsychiatric diseases of aging. With the quantification of MRI, technology can move from a process of picture taking, where reports are made on the basis of unusual identifications, to fundamental research into biological changes in disease and how these diseases respond to potential treatments.

4.1.1 Differences between 1.5 T, 3 T vs. 7T images

Typically the MRI scanner is built around a permanent magnet, which is the most expensive and important component of the scanner [67, 68]. The strength of the main magnet and its precision (homogeneity of the field strength) are important factors. Magnetic field strength is an essential factor in determining image quality. Higher magnetic fields increase the signal-to-noise ratio, permitting higher resolution or faster scanning. However, unlike lower field strengths, the higher field strengths have drawbacks such as more costly magnets, higher maintenance costs, increased

safety concerns, and increases in certain artifacts compared. The 1.0 - 1.5T field strengths are a good option for general medical use. The field strengths up to 3.0 T may be desirable for research (such as brain imaging); the latest research studies use 7T field strengths.

4.2 T1- WEIGHTED IMAGE

The use of T1-weighted images in clinical MR imaging is common [67, 68]. In these images, the signal is generally inversely related to the longitudinal relaxation time (T1) in a nonlinear manner; it also depends on other factors such as proton density. However, T1 is an intrinsic biophysical property of the tissue that is important for tissue characterization and for contrast agent uptake studies.

As the longitudinal relaxation time, T1 indicates the time required for the proton to become magnetized after first being placed in a magnetic field or the time required for the recovery of longitudinal magnetization following an RF pulse. T1 is determined by thermal interactions between the resonating protons and other protons or magnetic nuclei. The interactions allow the energy absorbed by the protons during resonance to be dispersed to other nuclei in the lattice. All molecules have natural motions due to vibration, rotation, and translation. The smaller molecules like water generally move more rapidly than the larger molecules like proteins. The T1 relaxation time reflects the relationship between the frequency of these molecular motions and the resonance (Larmor) frequency – which depends on the main magnetic field of the MR scanner. When the two are similar, T1 is short and recovery of magnetization is rapid; when they are different, T1 is long. For example, water molecule are small and move too rapidly for efficient T1 relaxation, but larger proteins move slowly. Both

have natural frequencies significantly different from the Larmor frequency and thus have long T1 relaxation times. Water in the bulk form (for example, cerebrospinal fluid, CSF) has a long T1 relaxation time because the frequency of its natural motions is much higher than the range of Larmor frequencies used clinically. However, when this same CSF is forced out into the periventricular white matter (as interstitial edema due to ventricular obstruction), its T1 relaxation time is much shorter. T1-shortening is produced by a dipole-dipole interaction between unpaired electrons on the paramagnetic iron and water protons in the solution. For example, the subacute hemorrhage appears brighter than brain. The difference in T1 values between brain parenchyma (shorter T1) and CSF (longer T1) can be used to the enhance contrast between the two. This is important when seeking abnormalities at the brain-CSF interface. The contrast in short TR/short TE sequences is based primarily on differences in T1 and is called "T1-weighted" images. The tissues with lower values of T1 have the highest signal intensity on T1-weighted images.

A 3-D magnetization prepared rapid gradient echo (MP-RAGE) T1-weighted sequence [70] is used to obtain high-resolution structural brain scans. Following an inversion pulse and a delay TI, a single segment of a 3-D gradient echo (GRE) image is acquired. After a further relaxation delay TD, this process is repeated for the next segment. Each segment usually comprises all partition-encoding gradients, so the number of echoes acquired per segment equals the number of partitions; the strength of the 2-D phase encoding gradient differs for each segment. Application of 3-D MP-RAGE to the imaging of the abdomen [71] and the brain has been reported. Structural brain imaging requires the optimization of the WM/GM signal difference to achieve high quality anatomical images and to allow precise image segmentation.

4.3 T2- WEIGHTED IMAGE

T2, the "transverse" relaxation time, measures how long transverse magnetization would last in a perfectly uniform external magnetic field [67, 68]. Alternatively, T2 is a measure of how long the resonating protons remain coherent or precess (rotate) "in phase" following a 90° RF pulse. T2 decay is due to magnetic interactions that occur between spinning protons. Unlike T1 interactions, T2 interactions do not involve a transfer of energy but only a change in phase, which leads to a loss of coherence.

The tissues with longer T2 times will generate stronger signals than those with shorter T2 times, if both are acquired at the same TE and if proton density and T1 are comparable. When multiple spin echoes are acquired, the signal strength generally decreases as TE is lengthened due to increasing T2 decay. Raising the echo delay time (TE) maximizes the differences in the T2 decay curves between tissues and increases the T2-weighting. Images obtained with a sufficiently long TR and TE such that the CSF is more intense than brain tissue are regarded as T2-weighted images.

A typical cystic lesion has a longer T1 and a longer T2 than brain tissue. On T1-weighted images, these lesions will appear dark (i.e. will have a negative contrast). On T2-weighted images they will appear bright and have a positive contrast. An awareness of the difference in relaxation times and the appropriate selection of TR and TE times can enhance the differentiation of lesions from normal tissues. T2 relaxation depends on the presence of static internal fields in the substance. Local field non-uniformities cause the protons to precess (rotate) at slightly different frequencies. Thus, following the 90° pulse, the protons lose coherence and transverse magnetization. This results in both T2* and T2 relaxation.

T2* relaxation is similar to T2 but includes additional dephasing effects caused by magnetic field inhomogeneities and susceptibility effects. The T2* effect leads to a rapid loss of signal because the frequency of precession increases causing it to move out of phase faster,. When paramagnetic substances are compartmentalized, they cause a rapid loss of coherence and have a short T2* and T2. This compartmentalization of substances with different degrees of induced magnetization leads to magnetic non-uniformity with shortened T2*, causing the free induction decay (FID) to decay more rapidly. Since gradient echo images are essentially rephased FID images, this also leads to signal loss on gradient echo images. Thus, acute and early subacute hemorrhage appears dark on T2-weighted gradient echo images.

Fluid attenuation inversion recovery (FLAIR) MR images are heavily T2 weighted, allowing easy detection of small and relatively low contrast lesions. At the same time, the long inversion recovery (IR) pulse nulls or greatly reduces the CSF signal, which minimizes artifacts arising from CSF motion and partial volume effects of CSF. Therefore, FLAIR sequences [72] are superior to conventional or fast spin echo T2 weighted sequences in visualizing a wide range of lesions, particularly those in the periventricular or subcortical areas. FLAIR images also disclose anatomical details and have the advantage of allowing disease detection in the white matter tracts within the brainstem. FLAIR images were used to identify and quantify white matter hyperintensities (WMH).

4.4 MAGNETIZATION TRANSFER IMAGING (MTI)

Magnetization transfer is a new technique in MR technology that may have many potential applications in clinical imaging [73, 74]. Magnetization transfer imaging (MTI) provides a way to generate a contrast in a magnetic resonance (MR) image that reflects parameters in addition to those of conventional T1, T2, and T2*. MTI [73-75] is based on interactions between a pool of free water protons and one that is bound to macromolecules. The term “cross-relaxation” describes spin lattice (T1) relaxation coupling between the macromolecular protons and free water protons. These interactions are achieved by the application of a saturation radio frequency pulse. This process gives rise to a reduction of the signal intensity in the MR image, with a correspondingly greater effect in regions where the transfer phenomenon is more efficient. The signal intensity reduction that results from this magnetization transfer process may be quantified by comparing the signal intensity of an image with and without the MT saturation pulse. The amount of MT, which is expressed as a magnetization transfer ratio (MTR), can be assessed for each pixel of an image.

Magnetization transfer in the MRI context was first discovered accidentally by Balaban et al, while attempting to perform a spin transfer experiment by selective saturation of the urea. Instead of finding a small signal suppression in water, the researchers identified a significant loss of image intensity; this generalized signal suppression is now known as MT. This unique contrast in the MRI has many advantages in a variety of clinical applications, including gradient-echo imaging and MR angiography. The magnetization transfer contrast was responsible for reduced signal intensity in the brain and muscle relative to that of fat, water, and paramagnetic contrasts agents. The contrast enables the semi-quantitative characterization of tissue and pathologic entities, which could substantially improve the specificity of MR imaging.

The physical mechanism responsible for magnetization transfer is explained here. By immobilizing the hydrogen bonds the molecular rigidity provides the necessary time for magnetization to occur. The rigidity separates the tissue proton line widths. An off-resonance pulse can selectively saturate these restricted protons. The T2s of the macromolecular protons (approx < 200μsec) are drastically shortened compared with free water (>10 msec). In a standard MR image, the macromolecular protons would be "invisible." The off-resonance pulse should saturate the immobile proton completely without directly affecting the free water protons. The magnetization transfer involves the exchange of longitudinal magnetization between the restricted protons and free water protons. The off-resonance irradiation selectively saturates the immobile protons; thus, initial magnetization occurs between the macromolecular protons and the transiently bound hydration protons. The efficiency of this interaction is directly related to the number of irradiation sites (hydrogen bonds) and their mobility. The diffusion of the saturated protons mixes with the free and bound protons and results in a decreased signal from the free water.

Using the off-resonance pulse is referred to as magnetization transfer contrast; the image obtained looks has a superficial resemblance to a T2-weighted image. T2 and MTI, which are sensitive to long correlation times, can be implemented on any scanner. However, T2 and MTI differ as follows: 1) the magnetization transfer contrast is related to structure and surface chemistry; 2) the standard imaging field strength appears more sensitive to long correlation times; and 3) the MTI is insensitive to susceptibility gradients unlike T2. The magnetization transfer appears to be a more reproducible measurement [74].

4.5 DIFFUSION TENSOR IMAGING (DTI)

Diffusion MR Imaging of the brain was first adopted in the early 1990s for use in clinical neuroradiology [76-78]. It was found to have immediate utility for the evaluation of suspected acute ischemic stroke. Diffusion is the translational movement of molecules, driven by thermally induced Brownian random motion; it refers to the constant random microscopic molecular motion due to heat. The Einstein equation describes the rate of diffusion at a fixed temperature:

$$\left\langle r^2 \right\rangle = 6 \bullet D \bullet t$$

where $<r^2>$ refers to the mean squared displacement of the molecules, t is the diffusion time, and D is the diffusion constant of proportionality for the particular substance being measured. Clinical Diffusion Imaging investigates water self-diffusion, i.e., the thermal motion of water molecules in a medium that itself consists mostly of water. The diffusion constant (units in square millimeters per second) relates the average displacement of a molecule over an area to the observation time. The higher the value of this constant, the water molecule is more mobile. In biological tissues, the self-diffusion of water molecules is not free but is instead hindered and restricted by the presence of various types of barriers. By introducing spatial magnetic field gradients, it is possible to obtain MR sequences that are sensitive to the diffusivity of water along a chosen direction, obtaining a so-called diffusion-weighted images (DWI) [79].

From the ratio of DWI images acquired at different levels of diffusion sensitization (known as b-value, and expressed in s/mm^2), it is possible to compute a quantitative measure of mean diffusivity, known as the apparent diffusion coefficient (ADC) expressed in mm^2s^{-1}. The diffusion-weighted images are constructed using a pulse sequence by adding a pair of diffusion-sensitizing gradients, also known as motion-probing gradients, to a T2-weighted spin-echo

sequence. These gradients are applied along the same directional axis both before and after the 180° refocusing pulse. This is known as Stejskal-Tanner diffusion encoding. The molecular motion thus results in loss of signal intensity due to the incomplete rephasing of water proton spins. This diffusion-weighted contrast can be fit to an exponential model, where Si is the diffusion-weighted signal intensity observed at a given voxel with the diffusion sensitizing gradients applied along direction i, So is the signal intensity at the same voxel without the gradient, and ADCi is the ADC in the i direction:

$$S_i = S_0 * e^{-b*ADC_i}$$

The b factor is a measure of diffusion weighting that is a function of the strength, duration, and the temporal spacing of the diffusion sensitizing gradients. As b increases the degree of diffusion weighting, it is apparent that boosting the gradient amplitude and gradient duration also increases the diffusion weighting as it has quadratic dependence of b. For clinical applications, the typical values of b range from 600 to 1500 secs/mm^2.

In a clinical setting, imaging molecular water diffusion confers the ability to probe the microstructural properties of biologic tissues. The typical diffusion times used for clinical DWI are 10–50 ms, corresponding to the average molecular displacements on the order of 10 μm. This microscopic spatial scale is in the same range as that of cellular dimensions. Such sensitivity to cellular processes has been exploited clinically (for example, acute cerebral ischemia). However, ADC maps and attenuation coefficient (AC) maps remain less sensitive than DWI signal hyperintensity for detecting small acute infarcts because they lack the multiplicative effect of T2 prolongation combined with the reduced diffusion that produces the “lightbulb” effect on DWI.The diffusivity of water in white matter is hindered primarly by axonal membranes and myelin sheaths. In axonal bundles, the diffusivity of water is much larger along the direction of

the bundle when compared to other directions—a condition known as anisotropic diffusion. Pure water at body temperature demonstrates isotropic diffusion, where the molecular motion is equal in all directions. In the human brain, isotropic diffusion may be found in the CSF spaces. The gray matter of the cerebral cortex in adults is also thought to exhibit isotropic diffusion at the clinical range of b-values. When diffusion is isotropic, the choice of direction for the diffusion-sensitizing gradient is not important because ADC_i is identical for all directions *i*. The molecular mobility is not equal for all directions due to anisotropic diffusion. White matter tracts with tightly packed, coherently-oriented fiber bundles hinder water displacement perpendicular to the direction of the fibers, resulting in larger ADC_i values parallel to the tracts rather than orthogonal to them. Hence, more than one diffusion-encoding direction is required to characterize regions of anisotropic diffusion.

Changes in the orientation of the patient's head would affect the interpretation of the DWIs by causing a probing in only a single diffusion direction. To avoid this problem that might confuse clinical interpretation, measures can be computed that will mathematically eliminate any directional dependence ('rotational invariance') [80]. Commonly used rotationally invariant measures, such as the geometric mean DWI ("isotropic DWI") and the trace ADC, require at least four separate image acquisitions: one without diffusion-sensitizing gradients (b=0 s/mm^2), and three probing motion along three mutually orthogonal directions. However, it is preferable that the diffusion-encoding directions not be pointing in opposite directions along the same axis and that they be as widely distributed in 3-D space as possible (mutual orthogonality). Stejskal-Tanner diffusion encoding cannot distinguish diffusion along one direction from diffusion in the polar opposite direction, a property known as "antipodal symmetry" [78]. Because two collinear diffusion-sensitizing gradients do not contribute independent information, collinearity should be

avoided in DWI acquisitions. Another rotationally invariant measure is the anisotropic diffusion of coherently oriented axonal fibers exploited for quantitative measures of white matter tracts. To calculate the diffusion tensor, this measure needs at least six diffusion-encoded image sets that are acquired along non-collinear directions in addition to at least one b=0 s/mm^2 image set.

Diffusion tensor [77], a mathematical model of the 3-D pattern of diffusion anisotropy of white matter tracts, which corresponds to an ellipsoid in space and is commonly used to model anisotropic diffusion in white matter (hence the name diffusion-tensor imaging, DTI). For isotropic diffusion, the diffusion ellipsoid is a sphere, because the ADC in every direction is equal. Anisotropic diffusion is modeled with an elongated ellipsoid, indicating a greater mean diffusion distance along the longest axis of the ellipsoid. The tensor shows a "conjugate symmetry" because the brownian motion shows an antipodal symmetry. The diagonal terms of the tensor indicate the magnitude of diffusivity in each of the three orthogonal directions. A number of diffusion tensor metrics (for example, fractional anisotropy) are used to characterize the dimensions and shapes of the diffusion ellipsoid associated with the microstructure of a particular voxel.

4.6 FUNCTIONAL MRI (FMRI)

Roy and Sherrington first reported coupling neural activity and changes in blood flow in 1890. Since then, researchers have shown that MR imaging could be used to visualize the dynamic changes in blood oxygenation across the brain; this was the beginning of functional MRI. Functional MRI has marked a major advance for the fields of cognitive and affective neuroscience by allowing investigators to test theories of the underlying neural pathways

controlling cognitive and emotional processes [81]. The functional MRI approach is often referred to as 'human brain mapping'[82]. In addition to studying the 'normal' human brain function, fMRI can also be used to characterize the functional activation patterns in patient groups. Group neural activity is accompanied by a hemodynamic response - by a transient increase in blood flow peaking after about 3 to 5 seconds before returning to baseline values. When the increased flow outweighs increased oxygen consumption, the vascular bed fills with a larger ratio of hemoglobin versus deoxyhemoglobin. The increase in blood flow with neural activation leads to an increased ratio of oxygenated versus deoxygenated Hemoglobin (Hb); because oxygenated Hb has a stronger MR signal, it is used as a proxy of relative brain activity. The hemoglobin is weakly diamagnetic and the deoxyhemoglobin is strongly paramagnetic, thus causing a local distortion of the magnetic field. The hemoglobin/deoxyhemoglobin ratio, therefore, modulates the magnetic field homogeneity within each voxel.

Gradient-echo MR sequences can be used to obtain a type of contrast, known as T2* contrast, which is dependent on the homogeneity of the magnetic field within each voxel. As first reported by Ogawa et al. [83], the intensity of signal in each voxel is modulated on the resulting images, on the order of a few percentage points, by the hemodynamic response following neural activation. This form of contrast is commonly referred to as Blood Oxygenation-Level-Dependent, or BOLD, contrast. The relationship between neural activity and hemodynamic response is uncertain. The BOLD signal had a stronger correlation with local field potentials than with unit recordings, suggesting that it could be more representative of synaptic input and intracortical processing than of spiking output. Given that the BOLD signal is superimposed to anatomical contrast, the alternation of stimulations states is needed for its detection.

The paradigms in use for fMRI experiments normally alternate within a reference resting state with sensory, motor, or cognitive activity. From the paradigm, a reference task is constructed; statistical techniques based on linear modeling theory are used to determine the degree of correlation between the temporal fluctuations of signal intensity in each voxel and the paradigm. Scan time has traditionally been a major issue in magnetic resonance imaging, functional imaging needed a rapid acquisition of the large (from tens to hundreds) number of volumetric image. Sir Peter Mansfield, who in 1977 introduced a new form of readout known as echo-planar imaging (EPI) [67], enabled the whole *k*-space to be acquired following a single excitation. By using EPI, fMRI studies can image the whole brain volume about every two seconds; the temporal resolution of fMRI is limited by the time constant of the hemodynamic response, whereas its spatial resolution may approach that of the morphological MRI. The area of clinical fMRI research has recently led to a number of new insights into the nature of psychopathology and treatment. The functional imaging can help identify the circuit involved in a particular task by contrasting the MR images acquired while someone is doing the task versus when that person is doing a control task. This can be done by block design, where the subject performs several minutes on a task followed by several minutes of control; the images during these blocks are then compared.

More recently it has become somewhat common to do event-related fMRI [84], in which images are acquired over the course of the individual trials of the task. In this case, control trials are interspersed with experimental trials. There are two primary advantages of event-related fMRI over block design fMRI. The first advantage is that for certain types of tasks, an event-related design more closely mimics the structure of the particular cognitive or affective task that was previously used in other (i.e., non fMRI) research studies. The other primary advantage of

event-related designs is that event-related fMRI allows the investigator to visualize the BOLD signal over the course of individual trials and to potentially capture the dynamics of the regional activity. This is in contrast to a standard block design study where the focus is on the overall level of activity averaged throughout a block of trials. An important issue in interpreting event-related fMRI is recognizing that the time course of the BOLD HRF signal is not instantaneous, but rather is smoothed over time. A short burst of synaptic activity suggests that a BOLD signal would last roughly 12-14 seconds and peak at between 4-6 seconds. Several studies have examined the statistical advantages between block-design and event-related fMRI, and the general view is that for the same amount of time spent scanning, the observed effect-size is larger for a block-design study as compared to an event-related study [85].

Functional MRI is, therefore, a powerful tool for investigating the localization of activations, but it is not useful for determining the sequence of events. Functional MRI output images are usually presented in the form of color maps superimposed on morphological images; non-significant correlations are not shown, and in some cases, different colors may be used to visualize both positive correlation (greater activation during task) and negative correlation (reduced activation during task).

The concern that the BOLD hemodynamic response is inherently relative creates a significant limitation in BOLD fMRI. Specially, the raw BOLD signal does not provide a reliable estimate of regional blood flow in a region; instead, there is a contrast of the BOLD signal on alternating experimental task versus control task that provides the meaningful signal. In contrast to this limitation, positron emission tomography (PET) imaging with an O15 radioligand is capable of providing quantitative blood flow measures. In MR imaging, a technique analogous to the O15 PET is also available; it is referred to as Arterial Spin Label (ASL) imaging, or

perfusion imaging [86]. In perfusion MR imaging, the MR excitation signal is inverted to provide a ‘tagged’ image, which is alternated with an ‘untagged’ image. Comparing the tagged image with the untagged image provides a quantitative measure of the perfusion of the region. The resultant full-brain voxel-wise perfusion images can provide a quantitative image of the perfusion across the brain. In addition to providing quantitative resting perfusion, ASL has also recently been used for investigating the blood flow changes associated with tasks. The two primary methods for perfusion imaging are referred to as Continuous Arterial Spin Labeling (CASL) and Pulsed Arterial Spin Labeling (PASL). CASL is believed to provide a better signal quality, but it generally requires special hardware for providing the continuous tagging pulse.

5.0 MRI IMAGE ANALYSES

5.1 INTRODUCTION TO MEDICAL IMAGE ANALYSIS

The medical image analysis provides useful information from images of various modalities that assist doctors with the diagnosis and treatment of disease. Advances in brain MRI image analysis have lead to a deeper understanding of pathological and physiological changes. For example, brain image analysis can be used to detect the presence of strokes or brain tumors. With rapid improvement in technology to provide high resolution of the human anatomy, the medical image analysis has slowly evolved as a method for extracting information with accuracy and efficiency using manual, semi-automated, or automated methods. The field of image analysis covers a large number of areas of interest, such as segmentation, registration, classification, object recognition, and shape representation [87].

In general, early radiologists based their diagnoses on manual methods where the user's direct interaction made the procedures subjective and time-consuming. The accuracy depends on the reliability and expertise of the users and the inter- and intra- user variability. The manual methods, often referred to as the 'gold' standard, are still used to validate the semi-automated and automated results. The automated image analysis procedures, which require no user interaction, tend to be computationally intensive because of image noise and structural variations. The semi-automated method is a hybrid of the manual and automated procedures and

is usually faster than the manual methods. In brain imaging, the common image analysis procedures used are the segmentation and registration of structural images. Before discussing the image analysis used for various MRI image sequences, the following section presents a brief summary of image segmentation and registration.

5.1.1 Medical Image Segmentation

The goal of image segmentation is to isolate anatomical features (like structures) of interest from the background and surrounding features [88]. This involves labeling voxels to indicate what each voxel corresponds to in the real world. For example, in brain imaging an algorithm can be used to label any structure (such as the hippocampus) and to give an image with voxels labeled as either hippocampus or not hippocampus. Another commonly used procedure in brain imaging is tissue classification, which varies from the segmentation and falls within the broad group of image classification. Image segmentation has a wide application in medical research in terms of , anatomical structures and tracking changes over time.

Although, the field of image segmentation has been an active area of research for several decades, it continues to raise difficulties due to non-homogeneous boundaries from data acquisitions or the variability of the structures. The image segmentation approaches can be categorized as follows: threshold, histogram, region, edge, contour, model, texture, and hybrid-based; these image segmentation approaches can also be semi-automated or automated methods. A straightforward segmentation approach is a manual one with the hand tracing the boundary of the structure of interest. In radiology, an expert with knowledge of anatomy performs using a visualization interface. These tracings of experts are frequently used as the gold standard to validate new algorithms of automated segmentation [87].

5.1.2 Medical Image Registration

Image registration, another important image analysis group, is a necessary process for comparing or integrating information from multiple images [87, 88]. Registration has the goal of spatially aligning two images so that correspondences are established between the image voxels. Image registration is used in medical imaging in many different ways: combining information of multiple imaging modalities, relating an individual patient to standardized atlases, and basing surgical plans on pre-operative images. The basic registration approaches use intrinsic information that relies only on patient data and on aligning segmented structures, voxel and landmark-based approaches. The segmentation-based registration methods either rely on a rigid or deformable model. The rigid models are generally used for intra-subject registration, and the deformable approaches are necessary for inter-subject and atlas registration. The accuracy of the provided segmentation from both images limits the rigid model approach. In the deformable approach, the extracted structures are represented as snakes or contours; they minimize an energy function and permit local transformations.

The voxel-based registration, which operates directly on the intensity values of the image voxels, uses two distinct approaches. The automated approach reduces the number of voxels to be considered and uses a computed center of gravity and principal axes, but the results are not accurate; it is used in pre-processing procedures. The second landmark approach, based on voxel properties, uses the whole image and optimizes transform parameters while minimizing the cost function (like histogram entropy difference) or maximizing a reward function (like cross-correlation, mutual information). This approach considerably increases the computational costs. The landmark-based registration methods attempt to identify a global transform that maximizes the mapping of landmarks for each other. The landmarks can be anatomical locatable points on

an anatomical structure or geometrical features such as boundary points. The optimum transform is obtained by minimizing a distance measure using optimizing methods such as the iterative closest point. Although, the landmark approach is typically fast and efficient due to the sparse number of voxels involved, the landmark extraction is manual.

5.2 TYPES OF MRI IMAGE ANALYSIS

The anatomical MRI is used to measure quantitative changes in geometric characteristics (usually size, volume, atrophy) and other measures (such as diffusion measures or magnetization transfer ratio). The functional MRI (fMRI) claims the complementary ground and provides changes arising from carrying out particular cognitive functions.

The biological changes at the cellular level require an imaging resolution order of 1–100 μm, but the resolution is much finer than the spatial resolution of the MRI (which is about 1 mm). Therefore, the MRI parameters are observed at spatial resolution of about 1 mm. These MRI parameters are generally more quantitative than those of the fMRI in terms of their reproducibility and correlation to underlying physiological changes. To obtain these measures, three different approaches (region of interest, histogram, and voxel based) were used to extract measures from a set of images or maps from 3-D volumes and subjects.

5.2.1 Region of Interest (ROI) Analysis

If the study focuses on measures from a particular region of the brain, then ROIs are drawn for each subject. The region can be of any shape, including circular, oval, square, rectangular, or irregular, and can be defined in one slice or over several slices. The ROI size is a compromise between reducing noise and reducing partial volume effects. The creation of the ROIs involves a learning process; inter-observer variation can be reduced by carefully defining the procedure to be used. For example, to obtain the magnetization transfer ratio (MTR) of lesions, the ROIs can be directly drawn on the MTR map and can also be defined on the conventional MR images before being transferred to the maps [74, 89]. The ROIs can be transferred between images when various images and maps are all spatially registered.

5.2.2 Histogram Analysis

One of the disadvantages of the ROI analysis is the placement of the region, but testing the whole brain removes this bias. The histogram analysis [74, 89] is appropriate for whole brain analysis and studies where the effects are widespread. After segmenting the brain (i.e. skull stripped), a histogram analysis follows. For example, studies have used histogram analyses to analyze such sub regions of the brain as large tumors or the grey and white matter. One of the disadvantages of histogram analysis is that localization information is lost; if disease only affects part of the region, then pooling data from the whole region will reduce the sensitivity.

5.2.3 Voxel-based Analysis

The voxel-based analysis [89] combines the ability of ROIs to be spatially specific with the ability of histograms to be unbiased. In the first step, the image datasets are spatially normalized to all lie in the same space. Once a particular ROI (whole brain or specific location) is identified, appropriate statistical tests are then carried out on all the selected voxels. Image datasets from all the subjects are spatially registered to the same stereotactic space followed by non-uniformity correction. The images are segmented into white matter, grey matter, and CSF (lesions, if present, are not dealt with). To reduce the effects of incomplete registration and residual inter-subject differences, the Gaussian smoothing is applied (typically with full-width half maximum 12 mm). A generalized linear model is applied, enabling a variety of statistical tests to be carried out. Group comparisons and correlations with an external parameter (such as age) can be done using this approach. This approach also allows the testing of all locations without prejudice; it only finds the locations of significant group difference. The disadvantages of this approach are that non-uniformity correction can cause the signal intensity to be altered and the localization of a difference using group comparison does not necessarily provide clear insight into the group's biological origin.

5.3 TYPES OF STATISTICAL ANALYSIS

Statistical analysis of the measurements is an increasingly complex procedure [90]. Below is a brief summary of the statistical methods used in comparing MR measures.

5.3.1 Group Comparisons: t-Tests and their Nonparametric Equivalents

The t-test, a commonly used approach, tests the usefulness of MR parameters to differentiate patients and control subjects. In such a comparison, it is important to check for type -I error (test will come out positive by chance) and account for multiple comparisons. A strict hypothesis-driven study set up before analysis can control for tyoe-I and type-II errors. Thus, an exploratory analysis using a hypothesis-driven study on different dataset would be useful to examine the errors. The results can produce positive or negative outputs. The future of image analysis lies in using non-parametric and multi-parametric methods to study appropriate clinical scores and in using localized analysis to increase the performance of MR parameters in characterizing disease.

5.3.2 Correlation with Clinical Score

In many studies, MR parameters are tested for correlation with a clinical measure. A parameter with a high correlation coefficient with statistical significance is thought to be a good candidate for a surrogate MR marker of the disease. The correlation values are dependent on the imperfect reliability (i.e. scatter) of the measures. This method implies association not casuality.

5.3.3 Classification of Individual Subjects and ROC Curves

When a measurement performs well in separating two groups of subjects, then it is valuable to understand its performance on individual subjects. A binary classification which chooses between two classes, needs a threshold to assign the classes [90]. The choice of threshold in a classifier is crucial for balancing out false-positive and false-negative errors. Receivers operating characteristic (ROC) curves [90] are often used in a binary classification to optimize the balance. To take into account the differing characteristics of the radiologists, radiological reporting may become increasingly ROC-oriented.

5.4 CHALLENGES IN GERIATRIC NEUROIMAGING

5.4.1 Significant Variability in Brain Structure

As explained in section 2.2.1, there is a well-established pattern of structural brain changes associated with aging. With increasing age, the brain decreases in overall volume, the cortical gyri become smaller, and the sulci and ventricles become larger. These changes in brain volume vary across individuals and may occur in individuals who are otherwise apparently healthy. A number of large epidemiologic studies have described these changes; they report the most prominent decreases in volume occuring in the frontal cortex of the brain [10]. The various image analysis procedures used in younger subjects would need improvements before becoming effective on an aged-brain. Many of the standard approaches for performing group comparisons of brain images depend on aligning all the brain images into a common stereotactic space.

Different software packages offer different computational methods for aligning the brain: landmark-based deformation, linear affine deformations [91-93], and several smooth non-linear deformations [93, 94]. Although these alignment methods may work well for certain young adult populations, where the variability in brain structure is limited, these methods seem insufficient at accurately aligning elderly brain images [95]. An alternative approach is to use a more highly parameterized deformation, such as the demons-based algorithm [87]. Studies have shown that this approach can lead to a more accurate alignment of brain images than the methods employed in the other neuroimaging software packages mentioned above.

5.4.2 The Influence of Brain Morphometric Changes on fMRI

The changes in brain volume and shape with age and with the diseases of aging present a particular challenge for functional MR studies [96] in these populations: How should these structural changes be accounted for when comparing the functional signal? In standard fMRI analyses, the functional information from all the subjects in a study are aligned with each other (sometimes referred to as alignment, cross-registration, warping, or normalization). Any variability in brain shape and size surpassing the capability of the alignment process may bias the results by contributing more CSF (due to the larger sulci and ventricles) in the more atrophic brains, as compared to more gray matter from the less atrophic brains. As noted above, the standard alignment algorithms differ in their ability to account for the variability in brain structure [95]. Some investigators [97] have addressed this problem by using a larger smoothing kernel in studies of aging subjects (for example, 10 mm instead of standard smoothness of 6 or 8 mm full-width half-maximum Gaussian). This approach recognizes that the alignment may be worse in the elderly population and corrects for this potential problem by blurring the images.

This allows the statistical voxel-wise comparison to find group differences, even if there is some discrepancy in the spatial co-localization. An alternative approach involves using a single-subject region of interest (ROI)–based analysis, rather than a voxel-wise analysis [98].

5.5 T1-WEIGHTED IMAGE ANALYSIS

The goal of the T1-Weighted Image Analysis is to compare the structural changes, such as volume changes, sulci span, or cortical thickness, among subjects. Many studies have noted volume changes in the gray, white, or cerebrospinal fluid across groups of subjects. These studies different approaches to characterize differences in the shape and neuroanatomical features of various brains. In this section, we discuss some of those approaches for T1-Weighted Image Analysis: Tensor-Based Morphometry (TBM), Deformable-Based Morphometry (DBM), Voxel-Based Morphometry (VBM) [99], and Automatic Labeling Pathway (ALP). These approaches can be categorized based on the computational neuroanatomic techniques used: some use the deformation fields themselves, which others use these fields to normalize images that are then entered into an analysis of regionally specific differences.

5.5.1 Tensor-Based and Deformable-Based Morphometry

Both approaches [99] involve studying brain shapes that are based on deformation fields obtained by the nonlinear registration of brain images. Tensor-Based Morphometry (TBM) refers to those methods that localize differences in the local shape of brain structures. Deformable-Based Morphometry (DBM) uses deformation fields to identify differences in the relative

positions of structures within the subjects' brains. The TBM approach is used to produce statistical parametric maps of regional shape differences and to localize structure. The deformation field, which maps one image to another, is considered as a discrete vector field. A Jacobian matrix field is obtained by using the gradients at each element of the field; at each element is a tensor describing the relative positions of the neighboring elements. One such measure is when the field is obtained by taking the Jacobian determinants at each point to obtain a map of the structure volumes relative to those of a reference image. Then, statistical parametric maps of these determinant fields are used to compare groups of subjects. The various morphometric measures derived from this tensor field can be used to identify regions with variations in shape. The DBM works at a global level, it treats the entire field as a single observation, or as a voxel-by-voxel basis, to make inferences about regionally specific differences. In addition to the shape information that is of interest, the vector fields also contain information on position and size that is likely to confound the analysis. The features of the field, such as global rotations and translations, are used to remove the confounding factors. Generally, a single multivariate test is performed using the parameters that describe the deformations - usually after parameter reduction using singular value decomposition. The alternative approach to analyze DBM involves producing a statistical parametric map that locates any regions of significant among the groups of subjects.

5.5.2 Voxel-Based Morphometry (VBM)

Voxel-Based Morphometry [99] is a commonly used image analysis approach for analyzing MRI data. As discussed in section 5.2.3, it involves spatially normalizing all the images to the same template space, extracting the specific area of interest (for example, gray matter) from the

normalized images, smoothing, and performing a statistical analysis to localize and make inferences about group differences. The output from the method is a statistical parametric map showing regions where the groups significantly differ. VBM is a computationally-efficient approach to addressing small-scale differences within the imaging capabilities.

5.5.3 Automatic Labeling Pathway (ALP)

Automatic Labeling Pathway (ALP) is an alternative approach for the analysis of T1-weighted images and a variation from voxel-based morphometry. ALP spatially normalized the subjects to template space and uses region segmentation to obtain measures characterized as region and tissue. This procedure helps determine regional gray, white, and CSF brain volumes; it can also be applied on a series of functional and structural MRI studies to automatically label specific anatomic ROI. The following presents a brief description of the procedure implemented in this study [95]. The pathway combines a series of publicly available software packages (AFNI, BET, FLIRT, and ITK) as well as some of our own custom programs to implement an atlas-based segmentation of MRI images. Using ALP, anatomic ROIs defined on the reference brain (MNI, colin27) are transformed to fit each individual's anatomic image; they are then segmented into gray, white, and CSF tissue types. The anatomic regions of interest are from the AAL atlas (90 manually traced regions), the Brodmann atlas (82 regions, included with the MRIcro software package), from locally generated regions defined from functional MRI studies, and from manual tracing. ALP is used to register the colin27 template brain to a 3-D T1-weighted high-resolution image of each subject (an SPGR or MPRAGE). Prior to the registration, the skull and scalp are stripped from both colin27 and the subject's 3-D T1-weighted image using the Brain Extraction Tool (BET)[92]; this is followed by a semi-automated erosion and dilation to remove additional

skull and scalp. The fully deformable registration model [95] was implemented using the registration library in ITK [87]. After registration of the template to the individual subject space, the ROIs from the template were applied to label regions on the subject's MRI. The number of gray, white, and CSF voxels in each of these regions was then counted to produce a table of ROI volumes for each region and each subject.

5.6 T2-WEIGHTED FLAIR ANALYSIS

White matter hyperintensities (WMH) are commonly found on T2-weighted FLAIR brain MR images in the elderly and are also associated with various syndromes of aging and a number of neuropsychiatric disorders, including vascular dementia, Alzheimer's disease, and late-life depression. Previous MRI studies of WMHs have primarily relied on the subjective and global (i.e., full-brain) ratings of the WMH grade. There are many manual, semi-automated, and automated procedures for segmenting and quantifying WMHs.

In this section, one of the automated methods for quantifying and localizing WMHs used in this study is explained [100]. The fuzzy connectedness algorithm was adapted to automate the segmentation of WMHs; it used a demons-based image registration to automate the anatomic localization of the WMHs based upon the Johns Hopkins University White Matter Atlas. The method was validated and compared with the accepted gold standard (manual ratings). The method also described the anatomic localization of the WMHs and detected the ROIs specific for the WMH burden. The major steps of the automated WMH segmentation and localization procedure involved 1) image preprocessing, 2) automated WMH segmentation, and 3) automated WMH localization. Image pre-processing included skull stripping of the T1-weighted high-

resolution image and FLAIR T2-weighted brain images, which improved the accuracies of the WMH segmentation and localization. For the skull stripping on the FLAIR images, we used the Brain Extraction Tool (BET) [92] on the T1-weighted images, which were acquired at the same location and voxel-size as the FLAIR images. The resulting stripped T1-weighted image was then used as a brain mask to remove the skull and scalp from the FLAIR image.

The automated WMH segmentation method (step #2 of the segmentation and localization procedure) involved four steps: 1) automatically identifying WMH seed based on intensity histogram of the FLAIR image; 2) using a fuzzy connected algorithm to segment the WMH clusters; 3) iteratively updating the set of seeds; and 4) combining the WMH clusters into the final WMH segmentation. The histogram of the skull-stripped FLAIR image was then used to define a threshold (mean + 3*SDs) for seed selection; voxels beyond this threshold were classified as WMHs, which were used as seeds in the fuzzy algorithm to segment surrounding WMH voxels. The background of the FLAIR images was excluded when calculating its intensity histogram, mean intensity, and standard deviation.

In the fuzzy connected algorithm, the fuzzy adjacency and affinity, both between 0 and 1, were defined for each pair of voxels: the fuzzy adjacency defined how close the two voxels were, while the affinity (determined by adjacency degree and intensity similarity) indicated how strong the two voxels “hang together” in space and intensity. For each selected WMH seed, the fuzzy connected algorithm [101] generated a fuzzy object, and within which each pair of voxels was a strong fuzzy connectedness or affinity (above certain threshold, 0.5 in this study). The system automatically delineated a 3-D WMH cluster containing the respective seed. Multiple 3-D FLAIR image WMH clusters were generated from the set of automatically selected seeds and

then combined to form an overall WMH segmentation volume. The fully automated WMH segmentation system was implemented in C++ and ITK [87].

5.7 MAGNETIZATION TRANSFER IMAGING (MTI) ANALYSIS

The MTI is based on interactions between a pool of free water protons and one that is bound to macromolecules and the reduced magnetization of the macromolecular proton pool. MTI, which is used clinically to characterize tissue, has been shown to be a unique measure [73]. The amount of MT is expressed as magnetization transfer ratio (MTR) [74, 75] and can be assessed for each pixel of an image:

$$MTR = \frac{(M_s - M_o)}{M_0} * 100$$

In the absence of saturation (M_o), the initial signal is obtained, and in the presence of saturation pulse applied to the bound proton pool (M_s), an image is obtained. MTR is the percentage reduction in the signal when the saturation is applied and expressed in percentage units (pu). The free water and CSF have MTR values close to 0 pu. The white matter has a high MTR (30–60 pu), and the grey matter has intermediate values. For example, the multiple sclerosis white matter lesions have reduced MTR values due to demyelination and loss of bound protons. Thus, the MTR values depend on the MTI saturation scheme used and also on the tissue characteristics. Tissue characteristics that determine MTR are a concentration of macromolecules (such as phospholipids), surface chemistry, and the biophysical dynamics of macromolecules.

5.7.1 Regional MTR analysis

The regional MTR analysis [74, 75] is performed by calculating the mean MTR in a number of pixels that constitute a region of interest (ROI) drawn on an image (for example, multiple sclerosis). Due to changes in the concentration and biophysical characteristics of the brain's macromolecules, this method is used to find abnormal MTR values resulting from a variety of diseases affecting the brain. These MTR values reflect better histologic heterogeneity (for example, wallerian degeneration) and are more sensitive to the presence of disease than conventional MR imaging.

5.7.2 Volumetric MTR analysis: MTR histogram analysis

Studies have explored the Volumetric MTR [74, 75] analysis based on three-dimensional MTI images. Here we explain one approach of doing MTR histogram analysis. We subjected the data to a segmentation program designed to separate the brain from its surroundings, and then we calculated MTR values on a pixel-by-pixel basis. From this data set, the mean MTR value was calculated and an MTR histogram was obtained. Finally, MTR histograms were normalized for brain size. The volumetric measures used to compare the groups of subject included: mean MTR of the whole brain; the MTR histogram parameters peak height; location of the peak on the spatial axis; and the 25th, 50th, and 75th percentiles. Some of these parameters were normalized for brain size. Studies have demonstrated that the MTR histogram's peak height was the volumetric MTR parameter that was most discriminative in comparing groups.

5.7.3 Quantitative Magnetization Transfer (qMT) Imaging

It has recently been possible to estimate the MT model parameters using quantitative imaging such as pulsed MT imaging. Measures, including the fraction of bound protons or T2-relaxation time, appear to be very specific and sensitive for loss of myelin, and can be expected to transform the role of MTI. When compared to MTR, the macromolecular proton fraction provides a more direct indication of myelin content in white matter. The quantitative measurements of the MT model parameters (qMTI) [74, 75] have shown great promise in terms of their biological sensitivity and specificity, although the implementation of qMTI can be complex. The qMTI requires a standardization of terms- clear definitions of models to compare measures across centers and the optimization of techniques.

5.8 DIFFUSION TENSOR IMAGING (DTI) ANALYSIS

Section 4.5 focused on diffusion weighted imaging (DWI) [79, 80, 102]. The diffusion-weighted signal intensity, caused by the anisotropy of white matter tracts, can be difficult to interpret for clinical DWI, unless rotationally invariant geometric mean DWI and trace ADC maps are computed. The diffusion tensor is a mathematical model formulated for non-collinear diffusion gradients by linear regression methods. The diagonal terms of the tensor indicate the magnitude of diffusivity in each of three orthogonal directions. The principal axes of the diffusion tensor, known as “eigen vectors”, can be calculated by diagonalizing the diffusion tensor.

$$\Lambda = \begin{vmatrix} \lambda_1 & 0 & 0 \\ 0 & \lambda_2 & 0 \\ 0 & 0 & \lambda_3 \end{vmatrix} = R \cdot D \cdot R^T$$

The diagonal matrix is obtained when the diffusion tensor (D) multiplied by matrix R and its transpose matrix. The eigenvectors describe the directions of the diffusion ellipsoid axes, and the corresponding length is represented by the rotationally invariant eigenvalues λ_1, λ_2, λ_3, in descending order of magnitude. For example, the primary eigenvector indicates the orientation of axonal fiber bundles and greatest water diffusion – essential for fiber tractography. The λ_1, which specifies the rate of diffusion along the orientation of the fibers, is known as "longitudinal diffusivity." The other two eigenvectors are orthogonal to the primary eigenvector. The magnitude represents the diffusion in the plane transverse to axonal bundles known as "radial diffusivity."

From the eigenvalues, various rotationally invariant diffusion metrics can be derived to describe the microstructure in a particular voxel. The mean diffusivity (MD) is the mean of the eigenvalues and represents the directionally averaged diffusivity of water within a voxel

$$MD = \frac{\lambda_1 + \lambda_2 + \lambda_3}{3}$$

The trace of D is the sum of the 3 eigenvalues and is another measure of orientationally averaged diffusion

$$trace(D) = \lambda_1 + \lambda_2 + \lambda_3$$

To measure the degree of directionality of intravoxel diffusivity, fractional anisotropy (FA) and relative anisotropy (RA) indices are defined.

$$FA = \frac{\sqrt{(\lambda_1 - \lambda_2)^2 + (\lambda_2 - \lambda_3)^2 + (\lambda_3 - \lambda_1)^2}}{\sqrt{2} \cdot \sqrt{\lambda_1^2 + \lambda_2^2 + \lambda_3^2}}$$

$$\text{(or) } FA = \sqrt{\frac{3}{2}} \cdot \frac{\sqrt{(\lambda_1 - MD)^2 + (\lambda_2 - MD)^2 + (\lambda_3 - MD)^2}}{\sqrt{\lambda_1^2 + \lambda_2^2 + \lambda_3^2}}$$

$$RA = \frac{\sqrt{(\lambda_1 - \lambda_2)^2 + (\lambda_2 - \lambda_3)^2 + (\lambda_3 - \lambda_1)^2}}{\lambda_1 + \lambda_2 + \lambda_3}$$

$$\text{(or)}\quad RA = \frac{\sqrt{(\lambda_1 - MD)^2 + (\lambda_2 - MD)^2 + (\lambda_3 - MD)^2}}{\sqrt{3}\cdot MD}$$

The anisotropy measures (FA and RA) are high when the primary eigenvalue is larger than the other two eigenvalues. The anisotropy measure indicates the preferred direction of diffusion. Fractional anisotropy, the most widely used measure of anisotropy in the literature, has a value that varies from zero (isotropic diffusion) to a maximum of 1 or 1.22 (perfect linear diffusion occurring only along the primary eigenvector). The metric maps (such as FA maps) are then used in the analysis to obtain an index from a brain tissue type or tract of interest. The FA map can be visualized using the primary eigenvector fiber orientation information by assigning a color - usually red to left-right, green to anteroposterior, and blue to up-down [79, 80]- to each of the three mutually orthogonal axes. Other measures include normalized total length in quantitative tractography. We will briefly discuss below some of the analysis methods used to compare these DTI measures: Voxel-Based Morphometry, Region of Interest, Tract Based Spatial Statistics (TBSS), and Tractography.

5.8.1 Voxel-based Morphometry

Diffusion metrics can globally compare the different subjects by using histogram- based summary measures, but this approach cannot be used to localize. Voxel-Based Morphometry (VBM) [103], as explained in section 5.5.2 for T1-weighted image analysis, is used for DTI analysis. Each subject's FA image (similar metric maps) is registered into a standard space, and then voxel-wise statistics are carried out to find areas for a group comparison. The common approach as follows:

- Align all subjects' diffusion related images to a chosen template, either directly or using the structural high-resolution images. Then, the registered output is smoothed.
- Carry out voxelwise statistics, using any relevant covariates for the design matrix.
- Threshold the resulting statistical T, F, or Z image, taking into account multiple comparison corrections.

Several other freely available packages have also been used for ''VBM-style'' analyses. The VBM analysis does not require the defining of regions or features of interest. The smoothing is done before the statistics and theresholding steps using 8-mm, 12mm FWMH smoothing. Different studies have reviewed the strengths and limitations of VBM [78, 104, 105]. VBM analyses have two major limitations: alignment issues and smoothing issues. Some of the alignment issues are poor tissue specificity and the difficult of differentiating between differences in morphometry from image misregistration and smoothing. A recent study [104] discussed a modified VBM analysis known as the Tissue-Specific, Smoothing-Compensated (T-SPOON) method that showed an improvement compared to the VBM analysis in a DTI study of white matter. Various normalization procedures, such as using different contrasts (single- and multi-contrast) in the registration approaches, have been used to improve the alignment issues.

5.8.2 Region-based DTI analysis

An alternative to VBM analysis is to specify a region of interest or tract of interest. This is usually carried out by hand and separately for each subject [78]. Then, specific diffusion measures are taken from the ROI(s) and compared across subjects. This approach is reliable in the largest tracts, but it is harder for smaller/ thinner tracts, particularly those with partial volume

issues; it is possible in regions where ROIs can be drawn. The ROIs can also be defined by using a white-matter tract atlas or tractography methods.

5.8.3 Tract-based Spatial Statistics (TBSS) processing

The localized statistical testing of diffusion-related data offers an alternative approach to VBM analysis by alleviating the alignment problems. The individual subject's data are projected into a standard space without being dependent on perfect nonlinear registration. A projection onto an alignment-invariant tract representation (the ‘‘mean FA skeleton’’) follows. This approach does not need spatial smoothing in the image processing. The following presents a brief summary of the tract-based spatial statistics (TBSS) [105] method used for multi-subject analysis of diffusion data. TBSS is distributed as a part of the FSL package to perform DTI analysis. The initial step is the creation of diffusion-related data (for example, fractional anisotropy) using the diffusion tensor. In the next step, all the FA images are nonlinearly aligned to a target brain. To improve the alignment process a target is created by warping all individual brain images in the group to each other; this minimizes the amount of the required deformation between the images. Apart from creating a study specific target image, it is possible to create a standard template to be used for alignment. Next, the individual FA images are averaged to produce a group average anisotropy image used to form a groupwise skeleton of white matter tracts. The skeletonization procedure is a morphological operation, which extracts the medial axis of an object. The skeletonization is used to encode the medial trajectory of the white matter fiber tracts with one-voxel thin sheaths [105]. Finally, FA values, accounting for misalignment, are projected onto this skeleton of white matter structures. For every subject image, FA values are analyzed along the normal projection for each point of the skeleton image; the peak value is assigned to the

skeleton. This is a very important process as it lines up the center of individual white matter tracts, which effectively corrects for the misalignment of individual fiber tracts. The FA values rapidly vary perpendicular to the tract direction but very slowly along the tract direction. The projection operation is performed under two constraints: 1) a distance map, created by equally dividing the distance between two nearby tracts, is used to establish search borders for individual tracts; and 2) a multiplicative 20-mm full width at half-max Gaussian weighting is applied during the search to limit maximum projection distance from the skeleton. This methodology has been used in clinical application such as schizophrenia, ALS, and multiple sclerosis.

This approach does have limitations. First, moving away from the larger tracts makes it very difficult to determine whether a reduction in FA is due to within-tract FA change or a change in tract thickness. Secondly, the effects, such as within-scan head motion which cause increased image blurring and biased FA, cannot be removed completely using this approach. Thirdly, the regions of crossing or tract junctions need to be carefully interpreted in this analysis. Finally, there is the possibility that pathology could so strongly reduce FA that potential areas of interest may be wrongly excluded from the analysis.

5.8.4 Fiber Tracking /Tractography

The primary goal of fiber tracking [78, 80, 102, 106] is to obtain the intervoxel connectivity on the basis of the anisotropic diffusion of water and to provide elaborate information about orientation and curvature of white matter pathways. This approach, applied in many clinical areas such as diagnostic neuroradiology, is used for the localization and the quantitative assessment of specific tracts. Fiber tracking uses the diffusion tensor (such as primary eigenvector) of each voxel to follow an axonal tract in 3-D from voxel to voxel through the

human brain. This “virtual dissection” makes it possible to depict human neuroanatomy noninvasively. The algorithms can be divided into deterministic and probabilistic methods. The results from fiber tracking can be visualized and portrayed graphically using curved lines or glyphs, such as hyper streamlines.

Using constraints on the maximum turning angle of the streamline between voxels and on the minimum FA within a voxel, the fiber tracking can be controlled to represent realistic white matter pathways. The user-defined regions of interest, based on prior anatomic knowledge, can be used to drive the tractography algorithms. The imaging artifacts, such as noise, patient movement, and distortion, produce uncertainty in the orientation of the diffusion ellipsoid and are detrimental for fiber tracking.

The deterministic methods, which use the eigenvectors to fiber track, initiate the fiber trajectories from user-defined voxels. One commonly used deterministic method is fiber assignment by continuous tracking (FACT). The probabilistic fiber tracking methods produce a connectivity metric for every voxel by incorporating the expected uncertainty into the algorithm. For example, by using statistical approaches such as the bayesian model or bootstrap statistics, the probability density function of the orientation of a neuronal fiber can be estimated with an empirical function based on the FA. The probabilistic DTI fiber tracking methods are considered to have the potential to delineate a greater portion of a white matter tract. The accuracy of the method used to estimate the probability density function determines the results of probabilistic fiber tracking method.

The diffusion tractography approach [80, 102, 106] has a few limitations: 1) it cannot distinguish antegrade from retrograde along a fiber pathway; 2) it only shows the path of least resistance to water diffusion; 3) the size of imaging voxels is typically a few millimetres cubed

so a single voxel could contain tens of thousands of axons; and 4) the methods perform poorly in regions of fiber crossing or small pathways. Diffusion tractography also produces false positives and negatives so the presence or absence of a particular pathway in a tractography result should always be interpreted with care. However, this is the only non-invasive technique for tracing white matter pathways that acquires the data in minutes and gives the opportunity for novel clinical investigations.

The tractography approach [78, 80, 102, 106] can be used to demonstrate qualitative changes in a specific tract to provide novel information on anatomy for making clinical decisions, but it can also be used as a quantitative tractography approach to provide a marker for degeneration. For a quantitative approach, a simple strategy would be to use tractography to extract a specific pathway and then to calculate diffusion measures along that pathway (such as FA) or use the values provided by the tractography algorithms, such as path probability. Some of the quantitative tractography metrics obtained directly from tractography algorithms for quantifying cerebral white matter integrity in whole brain white matter and in specific white matter tracts-of-interest are the following: curvature; torsion; parallel diffusivity; perpendicular diffusivity along bundle length normalized volume (NV); total length (TL); total weighted length (weighted for linear anisotropy) (TWLCL); total weighted length (weighted for FA) (TWLFA); number of streamtubes (NS); normalized total length (NTL); normalized total weighted length – linear anisotropy (NTWLCL); normalized total weighted length – FA (NTWLFA); normalized number of streamtubes (NNS); and average length (AL).

An alternative strategy would be a hybrid approach that guides the tractography algorithm by using the location of changes inferred from other approaches, such as regions of interest analyses, voxel-wise comparisons, or TBSS, to obtain quantitative scalar measures (such

as FA or TL). Some of the DTI analysis packages, including DTIStudio, MedINRIA, or PRIDE, provide the necessary tools for quantitative tractography, tract selection, and overlay on T1 image or other FA maps.

5.9 FUNCTIONAL MRI ANALYSIS

Because the spatial resolution is approximately 1-4 mm for fMRI images, it makes it possible to form maps of task-related cortical activity and to track brain activity in small areas within the resolution capabilities. The following summarizes the mechanism of BOLD: 1) the neurons receive synaptic input; 2) the neurons send signals to the vascular system to provide more oxygenated blood and makes it less magnetic; 3) the local MRI signal increases. The fMRI data analysis [81, 82, 94] has evolved over the years, as have all aspects of fMRI-based research; yet, no de facto standard approach to data analysis has yet emerged. One of the commonly used paradigms is the hypothesis-driven voxel-based approach where activation responses to a behavioral brain function across repeated observations and detect multiple subjects. The inferential statistics provide estimates of certainty in the experimental hypothesis; this process on whether differences between conditions are likely to be due to chance is known as significance testing. The testing is expressed as significance of the probability that the results could occur under the null hypothesis. Those voxels, whose probability levels are below a threshold probability, known as an alpha value, are labeled as significant, while those voxels whose probability is above the threshold are labeled as non-significant. The alpha value provides the probability of a Type I error – the decision that the null hypothesis is false when it is really true. In terms of fMRI a Type I error means that a voxel was labeled as active when it was not (i.e., a

false positive); this makes it challenging to decide upon an appropriate alpha value. Since the approaches are generally conservative, they exclude inactive voxels more than detecting all active voxels. Therefore, a high rate of Type II error in fMRI, or accepting the null hypothesis when it is really false (i.e., a false negative), occurs. The fMRI image analysis requires the processing of large quantities of data and performing enormous numbers of statistical tests. The analysis consists of various steps (Figure 3) that include movement correction, coregistration of anatomical and functional data, spatial normalization, spatial filtering, statistical analysis (“statistical parametric maps") [81, 82, 94], and data visualization. A number of publicly available packages, such as SPM, FSL, AFNI [91, 92, 94], provides the fMRI processing steps. These packages also provide other tools (such as “detrending”), image processing, and visualization functions.

All imaging methods have artifacts (for example, small movements of the head) that lead to erroneous results. The data need to be carefully reviewed to identify and correct these artifacts before using them for statistical analyses. The echo-planar imaging is a high-speed imaging technique used in fMRI to minimize the effects of movement in any one image. This technique allows volume to be collected in each run; Many runs occur in a typical session depending upon the length of the session; approximately 40-200 brain volumes per session can be captured. Since the fMRI-based signal modulation is very small (typically 0.5-5%), it is important that the images within and across runs are properly aligned to gain statistical power. Subject movement is generally regarded as the biggest problem for getting consistent data in fMRI-based experiments. The head motion during the fMRI scanning makes this process a challenge, because the pulsatile flow of arterial blood causes movement virtually everywhere in the brain, especially in the subcortical structures. When the movement is not too large or too fast,

the motion can be detected and the data can be transformed to compensate for the effects. These algorithms detect key features of many different kinds of movement, including stimulus-correlated movement. However, there is no good way to detect and correct the movement that could create MR signal artifacts that appear as a false activation signal. Typically, as much as 20-30% of data may be discarded because of head motion. The algorithms help to minimize physical motion during data acquisition and to detect and possibly correct for it, but none of these methods would completely compensate for the motion. Apart from using software packages to correct for the movement, experienced subjects who use bite bars in the scanner yield data free of serious motion artifact. Other artifacts, including scanner hardware drift, residual head motion, cardiac effect, and respiratory confound, further complicate modeling of the fMRI signal. These noise features need to be properly accounted for to make correct statistical inferences.

The statistical approaches [81, 82, 94] are variants of the standard statistics used for behavioral data such as ANOVA. The analysis is done using the contrasts from magnitude of the BOLD response at different conditions for every location in the brain. A voxel is the smallest distinguishable part of a three-dimensional image. A large number of statistics were performed on 10,000 voxels, with each voxel appearing 4x4x4 mm cube in the image. For every voxel, multiple statistical tests were typically done to determine if activity changed across conditions in that voxel. Therefore, a voxel-wise analysis of a typical brain imaging experiment requires running tens of thousands of statistical tests. The fMRI packages can perform the statistical tests in a few minutes, but the humans have great perceptual skills and can look at images, rapidly identifying bright spots. When evaluating whether a voxel has a different level in conditions, the common t-test is appropriate. The Kolmogorov-Smirnov (K-S) test is used to evaluate the variability or shape in the distribution. If a hypothesis makes specific predictions about the form

of the activity change (such as using a model for the expected hemodynamic response), then a correlation analysis may be useful. The fourier analyses are useful for identifying changes in the fMRI data occurring at the task frequency with designs that are alternating blocks. The most commonly used approach to the detection of effects in fMRI data is the general linear model, which uses a correlational analysis. The formula for the linear model is

$$y = a_0 + a_1 x_1 + a_2 x_2 + \ldots + a_n x_n + e$$

The basic idea behind a linear model is that the observed data (y) are equal to a weighted combination of several model factors (x_i) plus an additive error term (e). The parameter weights (a) indicate how much each factor contributes to the overall data. The term 'a' reflects the total contribution of factors that are held constant throughout the experiment. For fMRI data, this would include the raw T_2^* values recorded in particular voxels in the absence of BOLD activation, as well as any activity that is constant throughout the experiment. In solving the linear model equation, there is only one known experimental data quantity. Given the data and a specified set of model factors makes it possible to calculate what combination of weights serves to minimize the error term. The minimum error term after solving the linear model is known as the residual. Having only one dependent variable (for example, predicting income based on age and education) is known as a univariate multiple model. For the fMRI study, the same equation can be extended to include a large number of dependent variables, such as the many time points through the general linear model [82, 94].

A simple analysis takes the images of the brain during each of the designed experimental conditions and subtracts the average of the images collected during one condition from the average of the images collected during another condition. The "difference image" showed areas that were brighter, indicating a greater MR signal during one condition than another. The more

general approach is to compute a statistic based on the collection of values at each specific spatial voxel. These generic statistical computations on grouped images are more accurately described as “contrasts” rather than "subtractions." There are many different variations of this commonly used approach as well as various other approaches [107], such as multiple regressions, nonlinear regressions, small-world networks, pattern analysis, and machine-learning classifiers on fMRI data.

A “statistical map” of brain activation results when these statistics are computed for each voxel in the brain and when the resulting collection of statistics is presented in the form of an image in which color or intensity is used to represent the value of that statistic. The data visualization can be done using neurological or radiological convention. The “statistical map” can be displayed through a variety of methods, such as rendered image, glass-brain view, and inflated brain. The data visualization programs display the numbers in graphic form and allow the user to cut into the brain and see what lies inside. Generally, the researchers display the activation as color overlays to see these areas that are significantly more active (that would occur less than 1% of the time by chance). The general color scheme is that any positive activity is represented as yellow shifting to red. Negative activity is usually represented as blue shifting to green.

The fMRI results can be interpreted by identifying regions of interest (ROIs), a specified part of the cortex representing a 3-D space. The ROIs are either structurally defined or statistically defined. Instead of looking at activity from the hundreds of thousands of voxels in a typical image, it is much easier to look and interpret at activity from ROIs. Yet, it can be problematic defining a ROI due to selection bias problems. The activity at any given ROI can be examined over time. These plots represent the mean change in the BOLD signal for all the

voxels in a given ROI over time and across conditions. The plots can help represent differences across conditions and can realize the hemodynamic delay in the plotted data. Due to the slow response of the vascular system responding to increased neuron firing, the presented stimulus produces the maximal BOLD activity in approximately four seconds after the stimulus occurred. In order to report the results, it is critical to have a common reference coordinate system (for example, in degrees longitude and latitude). This system enables the researchers to determine if the area activated in one experiment is the same as the area activated in different experiments. One such coordinate system is called the Talairach Coordinate System. The coordinates are in millimeters, with X being right to left, Y front to back, and Z top to bottom. The interpreting of brain-imaging data is far more than looking at pretty pictures; it instead requires careful consideration of the control conditions and the contrasts. For example, an experiment comparing subjects viewing pictures of faces versus shapes needs to find the area in the brain that shows more activity when viewing faces. To conclude that this is the only “face area” in the brain, however, might not be appropriate. Carefully planned and implemented contrasts of related interpretations will improve the functional imaging results.

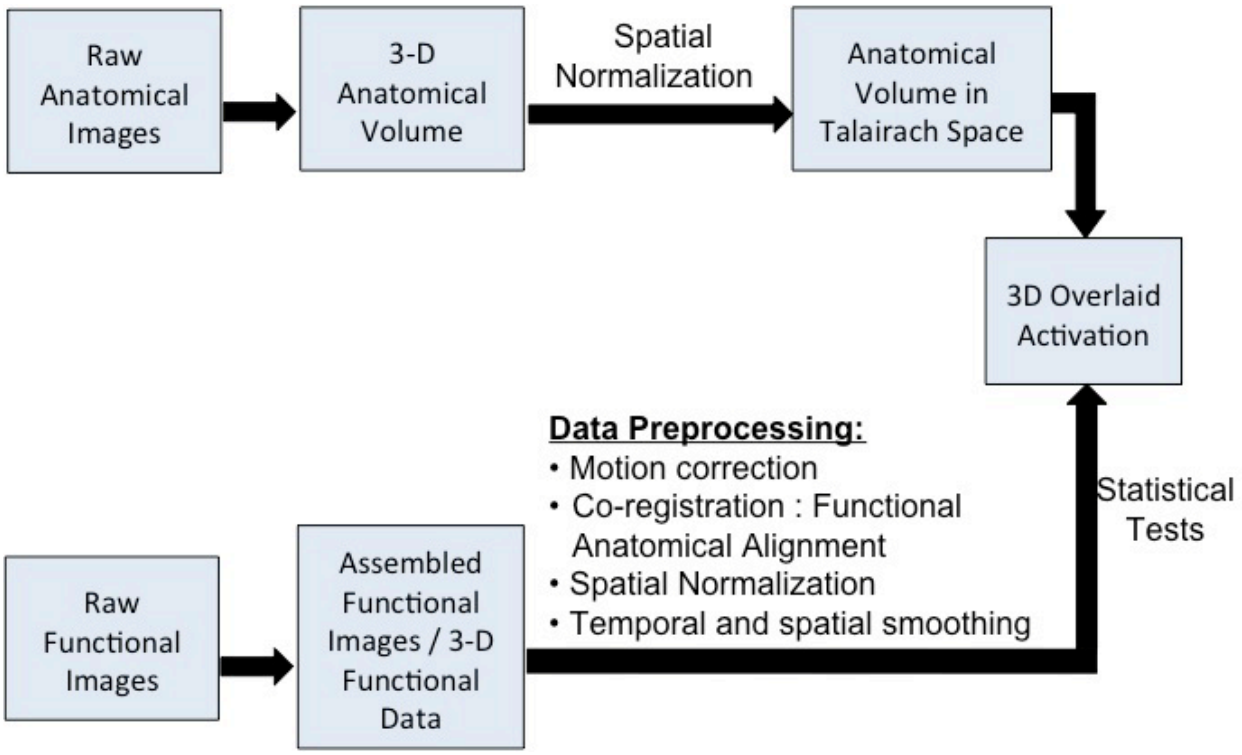

Figure 3. Scheme for Functional MRI Image Analysis

6.0 MRI RESEARCH IN COGNITIVE AGING

6.1 EFFECT OF STRUCTURAL DAMAGE ON FUNCTIONAL ACTIVATION

Functional neuroimaging studies of executive control function (ECF) have shown that older adults have greater brain activation within the fronto-parietal regions and also activate additional regions compared to younger adults [108-113]. This increased activation in the aging brain is well documented for various processes [58, 114, 115] including motor control [110, 113] and working memory [29]. Despite previous substantial work, [29, 65, 114-118] it is not clear whether increased brain activation in older adults is a response to underlying age-related brain structural abnormalities and whether it is important to maintain higher performance.

Previous neuroimaging studies indicate that greater brain activation occurs when there is an imbalance between the difficulty of the task and the neural/behavioral resources of the individual. For example, young adults have greater brain activation in response to tasks of greater difficulty [119, 120]. Similarly, work done by us [112] and others, [111, 121] indicate that older adults performing ECF tasks sometimes have greater brain activation compared to younger adults. The decline of neural resources with age can be detected on brain structural MRI as white matter hyperintensities and greater atrophy. Such brain structural abnormalities may be responsible for the patterns of neural activation observed during performance of ECF tasks in older adults. In the presence of such abnormalities, the brain may respond to the task either with

greater activation within ECF-related fronto-parietal regions or more “diffuse” activation with recruitment of non-ECF regions, or both. However, it is not known whether these changes in brain structure and activation are associated with better or worse ECF performance. If greater brain activation in individuals with brain structural impairment is associated with greater accuracy, then this would indicate that older adults' brain activation may be a compensatory strategy to maintain performance.

With the exception of a few studies of memory [122, 123], previous reports of ECF-related activation could not answer this question because they did not examine the relationship of brain activation with behavioral performance concurrently with brain MRI abnormalities. Studies examining each of these associations individually report that greater fMRI activation in older adults is associated with better performance [112, 121], while greater brain MRI structural abnormalities are associated with poorer cognitive function [124]. Recently, a few studies [125, 126] have begun to examine the interaction of fMRI brain activation with structural abnormalities, but did not account for performance. The objective of this work is to determine whether brain activation in older adults with brain structural impairment is associated with better performance on an ECF task. We will examine fMRI patterns of activation in the whole brain to assess whether greater activation is localized within ECF-related regions or it extends to recruit additional non-ECF regions or both.

6.2 RELATIONSHIP OF MACRO- AND MICRO- STRUCTURAL CHANGES

A number of studies have shown that geriatric disorders and disabilities are preceded by sub-clinical cognitive changes of aging and also by changes in MR imaging markers. To further understand the progression of age-related change and effectiveness of drugs and intervention, there is need for sensitive measures of the cerebral aging process. Thus, understanding the normal variation of markers would provide clues to detect early signs of aging, which could further be applied to study other neurodegenerative disorders. Noninvasive imaging like magnetic resonance imaging (MRI) would provide us insight into understanding the normal variation of markers and neurobiology of cognitive decline. Combining noninvasive imaging markers and cognitive measures would provide a broad perspective to better understand cerebral aging.

Postmortem and in vivo studies have shown that the brain shrinks with normal aging [127, 128]. Age-related changes in the normal aging have been studied using conventional MRI or macro-structural measures, which shows a decline in total brain volume, white matter (WM) tissue volume, and gray (GM) matter tissue volume [129-131]. These macroscopic brain changes that are visible with conventional MRI usually appear in the later-stage of the aging process.

Conventional MRI does not provide information about the earlier underlying micro-structural modifications occurring with aging. Magnetization transfer [73] (MT) and diffusion tensor [132] (DT) MRI are techniques that have the ability to provide information about the underlying subtle microscopic changes occurring in the normal aging brain that are not possible using the conventional MRI.

Each of the MRI measures, macro- and micro-structural, has a different relationship to age and provides complementary information. They may provide additional information on the pathophysiological processes and also be useful for quantifying damage in clinical trials. DT MRI is a technique that exploits the molecular diffusion of water within biologic tissue that is influenced by the characteristics of the surrounding medium [132]. The two commonly used parameters are Mean Diffusivity (MD) and Fractional Anisotropy (FA). The mean diffusivity is the average magnitude of molecular motion or measure of structural damage [133] and fractional anisotropy is a marker of tract integrity [134]. Increases in MD and reductions in FA have been reported with increasing age [135] and in patients with cerebral small vessel disease [136]. Recent studies [137-139] have shown that age related changes in FA are significantly correlated with changes in other indices of cerebral integrity and executive function. Studies showing age related white matter damage correlates with cognitive status [140].

MT MRI is based on the exchange of magnetization within the tissue between the protons bound to macromolecules and the protons of free water molecules. The MT ratio (MTR), which reflects the efficiency of this exchange, has been shown to decrease in the presence of brain tissue damage due to pathology like multiple sclerosis [141] or aging [142, 143]. MT has been found to be more sensitive than conventional MRI techniques in measuring age-related micro-structural abnormalities changes [89]. Few studies have investigated the relationship between MTI and cognition [140, 144].

The white matter hyperintensities (WMH) volume has recently emerged as an important neuroimaging marker of cerebral health in aging. WMH have been identified on T2-weighted FLAIR images in both normal aging and neurodegenerative disorders. Studies suggest that causation of WMH could be due to ischemia from small vessel disorder, trauma, inflammatory

response, and other causes [145]. A study showed that the WMH incidence rate could be as high as 60–100% in normal subjects aged above 60 years in large group of subjects [146]. Studies have shown that an increase in WMH volume is correlated with reduction in cerebral white matter volume and gray matter volume [147]; with severity of neurocognitive deficits in neurological disorders [148]; and with executive function [137]. Large-scale cognitive networks are dependent on intact white matter connections. The lack of integration of information across gray matter regions can lead to cognitive dysfunction caused by the disruption of specific white matter circuits. Further support is provided by the demonstration that functional connectivity is lost or changed in older adults [149, 150]. Advanced age is associated with substantial alterations of the cerebral white matter [9, 151], and age-related deterioration of the white matter integrity has been linked to declines in processing speed, memory, and executive functioning [152, 153]. The effect of age on cognitive abilities occurs over decades with mixed patterns in normal aging [154]. The neurobiological mechanisms underlying this relationship remain uncertain [155]. Thus, the issue of the relative importance of different indices of white matter and gray matter integrity in detecting age differences remains unresolved and calls for a direct comparison of the above mentioned measures within a single sample.

Previous studies have looked at the interrelationships of different MR indices with respect to cognitive function in aging. Benedetti et al. 2006 [155] looked at conventional MR indices such as volume, DT MRI (mean diffusivity) and MT MRI in gray and white matter. The study showed gray matter volume and average MD as independent predictors of age using a multivariable regression analysis including both tissue measures. A magnetic resonance spectroscopy (MRS) study found that the micro-structural metabolite alterations were associated with age-related changes in a broad range of cognitive domains (executive function, working

memory, information processing speed, long-term memory and fluid intelligence) [156]. Kochunov et al. 2008 [138] looked at the global trends and interrelationship for three indices (gyral GM thickness, dilation of sulcal spaces with CSF and volume of T2-WMH lesions) of cerebral health in a group of 31 normally aging subjects aged 57–82 and found that dilation of cortical sulci were primarly related to increases in WMH volume and secondarily related to the reductions of the cortical GM thickness. Kochunov et al. 2009 [137] explored the relationship between structural neuroimaging-based indices of cerebral integrity from the superior frontal and anterior cingulate regions and executive control function (ECF) in the older group (38 subjects). A large fraction of the variability in ECF (62%) can be explained by variability in the structural indices from these two regions. Schiavone et al. 2009 [157] compared micro-structural measures of white matter in 64 subjects to determine which technique correlated strongly with cognitive function (executive function, working memory, episodic memory and information processing speed) and FA was the most strongly related with age-related cognitive decline. Kochunov et al. 2010 [158] explored relationships between decline in cognitive processing speed (CPS) and change in frontal lobe MRI/MRS-based indices of cerebral integrity in 38 healthy adults (age 57–90 years). The study concluded that a substantial fraction of the variance in the psychomotor component of CPS (58%) could be attributed to atrophic changes in frontal WM, observed as increases in sulcal span, declines in FA values and reductions in concentrations of NAA and choline-containing compounds. A smaller proportion (20%) of variance in the psychophysical component of CPS could be explained by bilateral increases in frontal sulcal span and increases in WMH volumes. Burgmans et al. 2010 [159] investigated differences associated with age and hypertension in 93 subjects (age 50-77 years) using three markers of white matter integrity — gross regional volumes of the white matter, volume of the white matter hyperintensities (WMH)

and diffusion properties in seven brain regions: frontal, temporal, parietal and occipital white matter, and the genu, body and splenium of the corpus callosum. The study found robust age-related differences in DTI indices of WM integrity and age-related increase in the WMH volume, but no age differences in the gross regional volumes of the white matter. Hypertension was associated with decline in FA and exacerbated age differences in FA more than those in volume of WMH.

These findings indicate that of all of the examined measures, diffusion-based indices of white matter integrity may be the most sensitive indicators of global and regional declines and vascular damage in the aging brain. Limitations of the previous studies include that MRI regional and global markers for only white matter integrity have been used to understand the relationship of the markers, some studies did not look at cognitive changes and all studies were done using a smaller sample with age range (50-90 years). In this study we analyzed an epidemiologic sample using various macro-structural and micro-structural MRI global indices of gray matter integrity (atrophy index, relative peak height MTR and mean diffusivity) and white matter integrity (white matter hyperintensities, relative peak height MTR and fractional anisotropy) to look at information processing speed using digit symbol substitution test (DSST). We studied the relationship between MRI indices and DSST, and the interrelationships of MRI indices.

6.3 COMPARISON OF DTI ANALYSIS METHODS

Researchers adopt a particular diffusion image analysis approach based on the type of diffusion acquisition technique used and their analysis plan. In this section, we briefly discuss the various diffusion techniques and discuss the benefits of each approach discussed in section 5.8. This

section would provide background [80, 102] and motivation to one of our goals (Aim 3). One of the first techniques was diffusion weighted imaging (DWI), which provides diffusion measurements in one direction and so, it is easy to interpret but provides limited information. For trace and ADC imaging (>=3 gradient directions) diffusion coefficients are easily estimated and it is suitable for a hypothesis-driven approach. For diffusion tensor imaging techniques, the diffusion tensor is estimated from DWI images obtained in multiple directions and provides information about diffusion orientation and anisotropy. This technique requires a minimum of six gradient directions and typically takes 1-3 minutes to acquire. Scan time increases with an increase in the number of gradient directions acquired, 12-24 direction sequences typically take 5 - 10 minutes. For diffusion tensor data with 12-24 directions probabilistic tractography can be used, but the results are vulnerable to artifacts in the data. The diffusion tensor imaging can be done using multi tensors approaches (30 - 60 gradient direction), which typically take 10 - 15 minutes. Both probabilistic and deterministic tractography can be used with multi-tensor data. Advanced diffusion technique such as PASMRI, q-ball imaging and diffusion spectrum imaging can provide detailed information about diffusion orientation and anisotropy. The PASMRI technique is used with 60 - 128 gradient directions. The q-ball technique is used with 128 - 256 gradient direction (25 - 35 minutes). Q-ball imaging estimates a map of orientation distribution values. The accuracy cannot be guaranteed for all regions. Diffusion spectrum imaging is used with more than 256 gradient directions and provides a 3D diffusion probability density function map. This approach provides good specific angular resolution for fiber crossing, but whole-brain studies can take take a long time, and may not tolerable for certain patients. With such a variety of diffusion techniques, the corresponding analysis approach is selected based on the requirements for a study and there is no standard approach. The criterion for selecting an

approach is an active area of research and it remains uncertain which approach would work the best for aging or pathological changes. Many of the epidemiological imaging studies like ours use a 12-gradient directions technique, as it provides a good tradeoff between shorter acquisition duration and quality of data.

The region-of-interest (ROI) methods [133] using manual or automated approaches are appropriate when the hypotheses are defined in regions defined by manual-tracing or automated templates. The alternative is to use tractography to define the ROIs. The limitations of tractography approach for this purpose are: only tracts that are reliably traced can be used, identifying the effective ends of the tracts, and finally partial volume effects in ends of the tract. Most of the ROI methods are usually applied in the original image space and do not need any image processing alterations. The disadvantage of this approach is the accuracy of the ROI definitions.

Another commonly used approach is the voxel-based approach [103], two major limitations of this approach include poor image co-registration and weak statistical power from the large number voxels being tested. This approach is widely used in DTI studies because it allows whole brain studies without initial hypotheses. Spatial normalization accuracy is one of the major drawbacks, it introduces additional partial volume averaging and smoothing into the image data sets, and may alter the distribution of the DTI measures in a region. These drawbacks exist irrespective of the spatial normalization method (for example, higher dimensional) used. Some registration approaches lead to breaking the ‘‘topology’’ of the image being distorted, for example two distinct tracts could be merged into one. So these consistent differences in anatomical morphology can lead to misregistration errors that show up as apparent differences in the DTI measures during the voxel-based approach. Spatial smoothing is a commonly used step

after spatial normalization to correct for the variations. The smoothing extent is arbitrarily chosen and this creates problem for some of the applications such as aging. Smoothing increases the partial voluming problem in the DTI data, i.e. signals from GM, WM, and CSF will be mixed together leading to significant differences. Segmenting tissue or regions prior to smoothing can reduce this partial volume problem.

To address problems associated with voxel-based analysis for DTI data, slightly modified approaches have been used, such as applying single and multi-contrast registration approaches [160]. Sometimes, a one-hemisphere registration is used, which is particularly advantageous for analyzing hemispheric asymmetries. Lee et.al (2009) [104] have proposed a modified approach called tissue-specific, smoothing-compensated (T-SPOON) VBA. The various steps involved in this approach are: (a) segment the image data into tissue types. (b) DTI maps and tissue masks are then spatially normalized to a brain template. (c) spatial smoothing is then applied to all normalized maps including the masks. (d) Divide the smoothed DTI maps by the smoothed mask. (e) average normalized WM mask at the 20% level. (f) statistical testing and parametric mapping are subsequently applied. This approach minimizes the effects of partial volume averaging by performing tissue segmentation before normalization. The drawbacks of smoothing are compensated in this approach by dividing using a smoothed mask, so it produces DTI measures in the normalized maps, which is similar to original data and reduces the potential confound of the morphological differences. The significant clusters from VBA are used as seed points to drive the tractography algorithms.

Another widely used “whole” brain DTI analysis is the tract-based spatial statistics (TBSS) [105] to solve the alignment issues and issues with choosing smoothing extent. This approach estimates a ‘‘group mean FA skeleton’’, which represents the centres of all fiber

bundles that are generally common to the subjects. TBSS is freely available as part of FSL (FMRIB Software Library—www.fmrib.ox.ac.uk/fsl). This approach combines the strengths of voxel-based analyses with tractography-based analyses. With this approach the cross-subject FA becomes more gaussian and has lower variability. One of the major drawbacks of this approach is that there is the possibility that pathology could reduce FA so strongly that potential areas of interest may be wrongly excluded from analysis. The various steps involved in this approach were explained earlier in section 5.8.3, here we will discuss in detail how the individual subject's FA is projected onto the skeleton. The mean FA from all subjects is obtained and then fed into tract skeleton generation algorithm to obtain a skeleton, which aims to represent all tracts "common" to all subjects. The skeleton is obtained in a two-stage process, using estimate of the local surface perpendicular direction and then using second derivative of FA image. To project the individual subject's FA at each point in the skeleton, we search a given subject's FA image in the perpendicular tract direction to find the maximum FA value and assign this value to the skeleton voxels. This will remove need for perfect preregistration and not bias the comparison of FA values between the groups. The smallest misalignments in perpendicular direction have great effect in final FA statistics, but changes in direction parallel to the tract are relatively slow (i.e. initial registration is sufficient). Two constraints are used in this search: (a) the search to remain closer to the starting section of skeleton than to any other section of skeleton, the sections are defined using a skeleton distance map. The map is filled with a value encoding the distance to the nearest skeleton point and the search is enforced to be outwards from a given point with the distance measure increasing. (b) maximum search distance is used by using wide Gaussian function (FWHM 20 mm) when carrying out the search for maximum FA. When the local skeleton topology is tubular rather than sheet-like (for example, inferior part of the cingulum), a

circular space is used for the search rather than one perpendicular direction. Thus, for each subject the FA values from the centres of the nearest relevant tracts is filled. TBSS allows using other crossing fibers measures during the analysis instead of FA. Then, the voxelwise cross-subject statistical analysis is calculated.

For large clinical studies, typically diffusion tensor imaging with 12 gradient directions are acquired. A combination of the above mentioned approaches are used for image analysis. For aging population, the skeleton based approach does not detect the subtle changes due to age-related white matter integrity (such as WMH) [161] due to the projection of the maximum FA onto the skeleton. The goal is to obtain whole-brain white or gray matter integrity diffusion measures for individual subjects in aging population; in this study we compare the diffusion measures of white matter integrity obtained using skeleton based and automated template-based methods. This comparison was done using empirical and simulated data.

7.0 METHODS

7.1 EFFECT OF STRUCTURAL DAMAGE ON FUNCTIONAL ACTIVATION

7.1.1 Participants

Participants for this study were recruited from a larger group of older adults, who had completed a 1-year physical activity randomized controlled trial LIFE-P (Lifestyle Interventions and Independence For Elders—Pilot) [162] (www.ClinicalTrials.gov, registration # NCT00116194). The design of the LIFE-P has been described in detail elsewhere [162]. The primary mode of exercise for the intervention group was walking for at least 150 mins/week, and the active comparison group attended education sessions on nutrition, medications, foot care, and recommended preventive services at different ages. Group assignment of the intervention or active control was treated as a covariate in all analyses.

LIFE-P participants were screened for interest of participation in this brain fMRI study during a follow-up phone call 1.7 years±1.7 months after close-out of the intervention study. MR eligibility was assessed by self-report and review of medical records. Participants were eligible if they had no history of metallic fragments, cardiac pacemaker, aneurysm clip, cochlear implants, weight of more than 250 lbs or claustrophobia. Those who had been hospitalized and/or had surgery in the month prior to the MRI were also excluded. The University of Pittsburgh

Institutional Review Board approved the study and all subjects gave written informed consent. A total of 30 participants (mean age: 81.16 years, standard deviation: 3.55 years) were MRI eligible, agreed to participate and received a brain MRI and an in-person exam. These subjects had similar characteristics ($p>0.14$ for all comparisons) compared to the rest of the group interviewed (n=74) with the exception of race (african americans: 10 vs. 37% in the fMRI vs. not fMRI group, Fisher exact test: $p=0.004$).

7.1.2 Scanning protocol for Functional and structural MRI

The magnetic resonance (MR) images were acquired on a 3 T Siemens Trio MR scanner, using a Siemens 12-channel head coil. Functional MR images were acquired as whole-brain gradient-echo echoplanar images (EPIs) [repetition time (TR), 2 s; echo time (TE), 32 ms; resolution, 128 * 128; slice thickness, 3.0 mm; 29 axial slices; GRAPPA with acceleration factor of 2]. Each scanning session started with the acquisition of a three-dimensional MPRAGE high-resolution T1-weighted image (TR, 2.3 s; TE, 3.43 ms; slice thickness, 1 mm; 176 slices) for anatomical detail (gray matter measure, brain volume and atrophy) and FLAIR T2-weighted image (TR=9 s; TE= 102 ms; TI=2.5 s; slice thickness, 3 mm; 49 slices) for extracting the WMH burden.

7.1.3 Structural brain image analysis

Total volumes of gray matter, white matter, and cerebrospinal fluid were obtained using a previously validated procedure: the Automated Labeling Pathway (ALP) [95, 163]. ALP applies a nonlinear registration algorithm (a fully deformable automatic algorithm) to transform a template brain (the Montreal Neurological Institute Colin27 template) into the native anatomical

space of each individual's brain. Total gray matter volume, white matter volume, and cerebrospinal fluid volume were estimated in cubic millimeters by summing all voxels classified as these tissue types and multiplying it by one voxel volume (i.e., 1mm*1mm*1mm for T1-weighted image). Atrophy index was calculated as the ratio of cerebrospinal fluid volume and gray matter volume. White matter hyperintensity (WMH) volume was obtained using an automated method previously published [100, 101]; and it was normalized for brain volume.

7.1.4 fMRI paradigm

Participants were asked to perform Digit Symbol Substitution Test (DSST) in the scanner. The DSST is a test of psychomotor performance, which requires incidental memory, perceptual organization, visuomotor coordination, and selective attention to filter out irrelevant information (for example, symbols that may look alike) and to perform successfully [34, 51]. The test has high test–retest reliability [35, 52]. The DSST is particularly sensitive to cognitive changes associated with aging, especially working memory, information processing speed, and executive control function. In addition to the computerized version of the Salthouse DSST (sDSST) performed during fMRI, participants also performed the pencil and paper version of the DSST, frequently employed in epidemiological studies of older adults [53].

7.1.4.1 sDSST task parameters during fMRI acquisition

The computerized version of the sDSST is a validated test [35, 52]. In this study, the sDSST was adapted for the fMRI scanning procedure (Figure 4) to test the working memory domain. As illustrated in Figure 4, the subject sees on a computer screen one number–symbol matching pair (cue). After the cue disappears, an answer key (probe) appears containing a grid of four number–

symbol matching pairs. The subject is instructed to push the right-finger button if the probe contains one number–symbol that matches the cue, and to push the left-index finger button if the probe does not contain any number–symbol that matches the cue. Instructions are to respond “as fast as you possibly can”. Accuracy and response time during the task were obtained. Accuracy was computed as number of correct responses/total number of responses. Response time was computed as the interval of time between appearance of the probe and the subject's response. Overall, this version of the DSST can be viewed as a working memory task with one item as the cue and four items as the probe. Thus, unlike the standard DSST, which uses RT as the primary outcome measure, we have chosen in this case to use accuracy, which is often the primary outcome measure for working memory tasks. Participants were instructed on the task outside the magnet for as long as needed to familiarize them with the task (usually 5–10 min). The sDSST was presented using a block design with 8 trials/block, in which a block of the experimental sDSST condition is alternated with control condition for a total of 10 blocks (Figure 4). Each block lasted for 56 s including 8 s of instructions at the start of each block to remind the subjects of the task. The 8 s of instruction and the first trial of each block were excluded from the analyses (see ‘fMRI data analysis’ below). The different task conditions (matching vs. non-matching) were randomized 1:1 across the block. The task consisted of a total of 5 sDSST-blocks alternating with 5 control-blocks for a total of 9min and 20 s. The control condition was designed to account for the non task-specific brain activation (frontal eye field and visual cortex for eye movements, and motor cortex for the index fingers movements) that are likely to be elicited during sDSST performance in addition to the task-specific activation of the executive control function network.

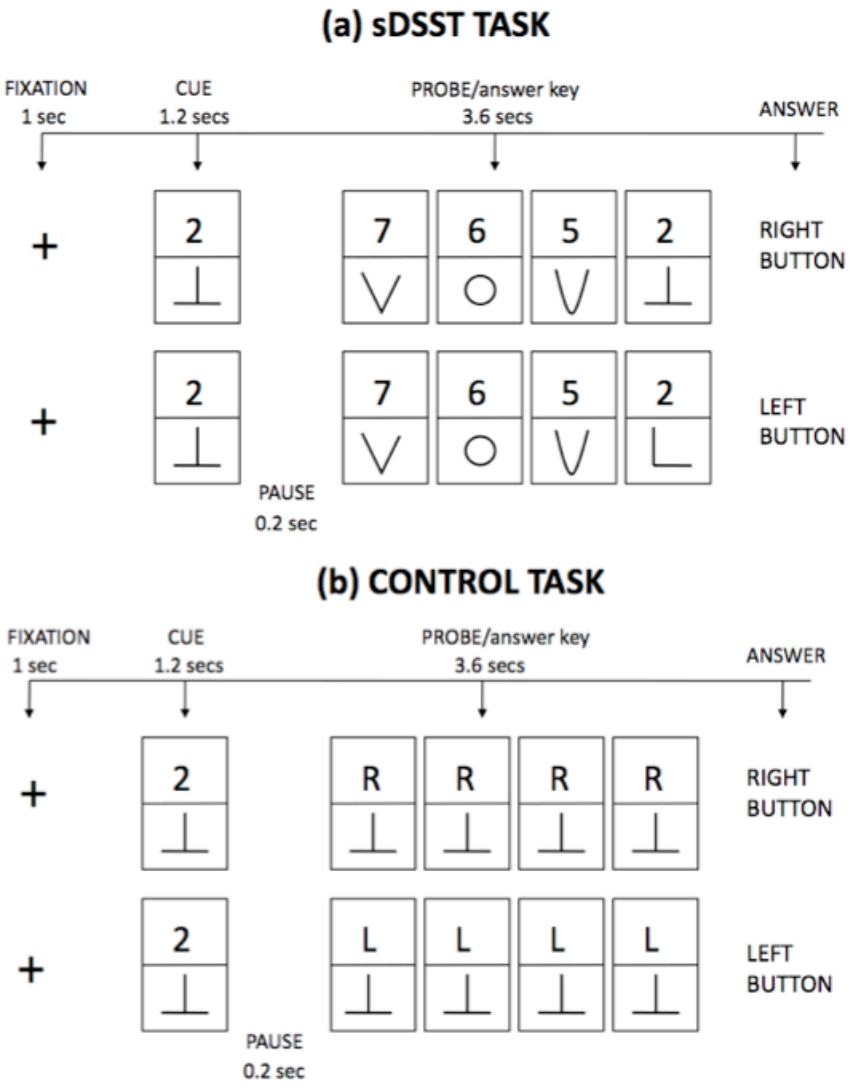

Figure 4. Schematic diagram illustrating (a) sDSST (b) control condition tasks.
Schematic representation of the tasks that the participants were administered during the brain fMRI scanning session. Two examples are shown for the sDSST (matching right button and not matching left button) and for the control condition (right button and left button).

Responses occurring after the probe disappeared (after 3.6 s) were termed as "no response" and were omitted from the calculation of accuracy and response time. In additional sensitivity analyses, the "no response" were coded as "wrong" with a response time of 3.6 secs, and were thus included in the computation of accuracy and response time.

7.1.5 fMRI data processing

Functional imaging data was analyzed with Statistical Parametric Mapping 5 (SPM5) [94] (Wellcome Department of Imaging Neuroscience, London, UK) implemented in MatLab (MathWorks, Natick, MA). For each subject, all EPI volumes were realigned to the first volume of the time series, and a mean image of the realigned volumes was created. Standard SPM high pass filter was applied to address low-frequency scanner drift that could potentially contaminate the signal. The realigned images were co-registered to the anatomical T1-weighted image. To normalize the anatomical image as well as the EPIs to a standard SPM reference system the following procedure was applied. First, the anatomical image and a representative template image [Montreal Neurological Institute (MNI)] was segmented into gray matter, white matter, and CSF. Then, the gray matter of the anatomical image was normalized to the gray matter of the MNI brain image. Subsequently, the derived normalization parameters were applied to the EPIs, which were subsampled to a voxel size of 2 * 2 * 3 mm and smoothed with a Gaussian kernel of 8 mm FWHM.

7.1.6 Analyses

All analyses were adjusted for group assignment. Participants' characteristics were compared using non-parametric tests. Mann–Whitney test and Fisher exact tests were used to compare differences in means and proportion between groups for continuous and categorical variables, respectively. Non-parametric correlation coefficients were computed to test the association of atrophy index and WMH volume with accuracy.

Based on sample size computations for fMRI BOLD signal, [164] this study had adequate power of 80% to detect an effect size of at least 0.72 or a significant mean difference of 0.18% with power alpha=0.05 with a sample size of n=25. Analyses were performed in the context of the general linear model [94]. Each condition was modeled using a delayed boxcar function. Block length was of 42 s, after excluding the first 8 s (instructions) and the first trial. The first trial was excluded to address variability in the hemodynamic response due to saturation after the initial hemodynamic up-swing, which should occur by the end of the first trial in a block design. Additionally, movement parameters derived from realignment were added as covariates of no interest to correct for confounding effects induced by head movement. Two contrasts of interest were used: sDSST>Control condition and Control condition>sDSST. These were first estimated for each subject individually (averaging activation across runs), and then subjected to a second-level random-effects analysis. For all analyses, the t values were thresholded at a minimal voxel entry value of $t>1.71$ ($p<0.05$ uncorrected) and then corrected for multiple comparison using AlphaSim (gray matter mask, 1000 Monte Carlo simulation, and smoothness obtained using 3dFWHMx) [91]. In all analyses, the clusters with cluster probability (alpha) of 0.001 (extent threshold: 433 voxels) were accepted and identified using WFU_Pickatlas [165].

7.1.6.1 sDSST-related brain fMRI activation and its relationship with accuracy

Second-level analyses were performed over all subjects to obtain the two contrasts of interest (sDSST>Control condition and Control condition>sDSST), which were modeled using a one-sample t-test, adjusted for group assignment and atrophy index. The mean group activation maps were estimated at each voxel and restricted to gray matter. Subsequently, the association of fMRI mean signal with accuracy (continuous measure) adjusted for group assignment, sDSST response

time and atrophy index was estimated. An activation map was obtained for positively and negatively correlated regions with accuracy.

7.1.6.2 Relationship between fMRI activation, accuracy, and brain structural abnormalities

In subsequent analyses, we tested the associations of WMH volume (or atrophy index) with the mean group activation maps obtained from the sDSST>Control condition contrast. Associations were estimated for each voxel and restricted to gray matter. To investigate the interrelationship between brain structure, brain activation and performance; we also examined the fMRI patterns of interaction of accuracy by WMH volume. Specifically, the model included terms for accuracy, WMH, and accuracy * WMH (interaction term). The analyses were adjusted for group assignment, atrophy index, and sDSST response time. In additional exploratory analyses, we further examined the association of accuracy with fMRI activation in subjects with WMH measure above the median.

7.2 RELATIONSHIP OF MACRO- AND MICRO- STRUCTURAL CHANGES

7.2.1 Participants

Participants were selected from the parent Health ABC (Health, Aging and Body Composition) study. Health ABC study is a longitudinal, observational cohort study of 3,075 well-functioning older Caucasian and African-American men and women from Pittsburgh, PA and Memphis, TN aged 70-79 when enrolled in 1997-1998. The parent Health ABC study was designed to determine the relationship of changes in body composition, weight, and related health conditions

to incident mobility disability. In 2006-07, 325 Health ABC participants who were interested, eligible for a brain 3T MRI, and able to walk 20 meters, participated in the BRAIN-MRI ancillary study at Pittsburgh (Table 2). Participants received a brain MRI, neurocognitive testing, and detailed neurological and gait exams in addition to in person health ABC assessments. Each subject's medical history was reviewed to rule out endocrinal, neurological, and/or psychiatric illnesses. The BRAIN-MRI subcohort is representative of the existing Health ABC cohort with some expected differences in age, and it maintains a substantial racial diversity (42% African Americans). Due to the exclusions for the MRI testing, we expected this age difference. All subjects provided written informed consent. The University of Pittsburgh institutional review board approved the protocol. Of the 325 subjects who received a brain MRI, 277 subjects had a complete dataset of MR measures and demographic information. In the analysis, only 272 subjects were used; five subjects were removed due to poor MR image quality.

Table 2. Population characteristics of the HABC cohort

	N=390 (No MRI)	N=277 (All MRI variables)	N=272 (Used in the analysis)
Outcome			
DSST, number correct, mean (SD)	34.15 (13.66)	36.76 (13.55)	36.61 (13.6)
Demographics			
Age, yrs, mean (SD)	83.79 (2.85)	83.26 (2.71)	83.25 (2.71)
Male, N (%)	188 (48.2)	117 (42.24)	116 (42.6)
African-American, N (%)	127 (32.6)‡	113 (40.79) ‡	110 (40.4)‡
TENG 3MS, 0-100, mean (SD)	92.41 (7.49)	92.92 (6.71)	92.85 (6.73)

DSST: Digit Symbol Substitution Test; TENG 3MS: Modified Mini-Mental State Examination
‡ Age-adjusted differences of men vs. women significant at ($p<0.05$).
* Age- and gender-adjusted differences of included (n=272) vs. excluded (n=390) significant at ($p <0.05$).

7.2.2 Cognitive Test - DSST

The DSST is a pencil and paper test of psychomotor performance [51] in which the subject is given a key grid of numbers and matching symbols, and a test section with numbers and empty boxes. The test consists of filling as many empty boxes as possible with a symbol matching each number. Time is 90 seconds, and the score is the number of correct number–symbol matches. The strategy to solve the DSST consists of sequential encoding, and retrieval of numbers and matching symbols. First, the number in the test section is encoded in the individual's short-term memory and temporarily stored. Then, while the subject visually scans the key grid to search for the number–symbol match, each number is retrieved from his or her short-term memory and compared with the numbers on the key grid. Once a number is recognized, the matching symbol is encoded in individual's short-term memory. Finally, the attention is turned toward the test section again, and the symbol is retrieved from short-term memory and written below the number. Incidental memory, perceptual organization, visuomotor coordination, and selective attention are important factors that affect the final score [51]. The ability to filter out irrelevant information (for example, symbols that may look alike) also influences performance. This test has high test–retest reliability [52]. It was used as an outcome variable in this study.

7.2.3 Image Acquisition

All MRI scanning was performed on a 3T Siemens Tim Trio MR scanner at MR Research Center in University of Pittsburgh, using a Siemens 12-channel head coil. Four series of MRI images were acquired on the MR scanner. Magnetization-prepared rapid gradient echo (MPRAGE) T1-weighted images were acquired in the axial plane with TR=2300 ms, TE=3.43 ms, TI=900 ms,

Flip angle= 9 deg, Slice Thickness= 1mm, FOV= 256*224 mm, pixel size= 1mm*1mm, matrix size= 256*224, number of slices=176. Fluid-attenuated inversion recovery (FLAIR) images were acquired in the axial plane with TR=9160 ms, TE=89 ms, TI=2500 ms, FA=150 deg, FOV= 256*212 mm**,** slice thickness=3 mm, matrix size=256*240, number of slices=48 slices, pixel size= 1mm*1mm.Diffusion Weighted Images (DTI) were acquired using single-short spin-echo sequence with the parameters TR=5300 ms, TE=88 ms, TI=2500 ms, Flip angle= 90 deg, FOV= 256*256 mm, two diffusion values of b=0 and 1000 s/mm, 12 diffusion directions, 4 repeats, 40 slices, matrix size =128*128, pixel size= 2mm*2mm, slice thickness= 3mm, GRAPPA=2. Two series of sagittal scans (with and without the an off-resonance saturation pulse with offset frequency=1.5 kHz) were obtained for the MT acquisition across 120 slices with matrix size=256*192, TR=35ms, TE=2.86 ms, TI=300 ms, Flip angle= 15 deg, slice thickness: 1.5mm, pixel size= 0.89 mm*0.89 mm, FOV= 230*230 mm. The MR images used in this study were checked by a radiologist for any unexpected findings and were excluded from the study.

7.2.4 Image Processing and Analysis

The brain tissue segmentations (gray matter (GM), white matter (WM) and CSF) were obtained by segmenting each individual's skull-stripped T1-weighted image in native anatomical space using FAST - FMRIB's Automated Segmentation Tool [166]. Total GM volume, WM volume and CSF volume were estimated in cubic millimeters by summing all voxels classified as these tissue types and multiplying it by one voxel volume (i.e., 1mm*1mm*1mm for T1-weighted image). Total brain volume including CSF volume within the entire skull is often referred to as total intracranial volume (TICV). Brain segmentation software usually includes the CSF between the surface of the brain and the interior of the skull, but not necessarily all of the CSF between

the inner skull and the brain. In order to measure TICV using T1-weighted image, BET was used with an advanced option to extract additional skull and scalp surfaces (−A) [167]. A volume measure qualitatively equivalent to TICV was calculated as the volume contained within BET's 'inner skull' segmentation. The accuracy of using BET to approximate TICV was qualitatively assessed to be reasonable for the purposes of this paper. Atrophy index (AI) was calculated as ratio of non-gray matter (TICV minus GM volume) and TICV. The white matter hyperintensities (WMH) volume was obtained from T2-weighted FLAIR image using an automated method for quantification and localization of WMH. The WMH quantification was done using a fuzzy connected algorithm with automated seed selection [100]. The total WMH volume was estimated by summing all the voxels classified as WMH and multiplying it by one voxel volume. The total WMH volume was normalized for brain volume.

The diffusion-weighted images were preprocessed to remove unwanted distortions due to eddy currents. The DTI maps were computed [76] and diagonalized to determine the eigenvalues from which the FA and MD maps were computed [134] using FMRIB's Diffusion Toolbox [92]. The FA map was registered to the FMRIB58_FA template [92] using FMRIB's Non-linear Image Registration Tool (FNIRT) [168], similar to Tract-based Spatial Statistics (TBSS) [105]. The transformation was also applied to the MD map. Then, using the segmentation of WM, GM and WMH, the FA and MD maps were restricted to normal appearing WM and normal appearing GM. Mean MD and Relative peak height FA (100 bins, FA between 0.2 and 1.22 with bin size: 0.010303) were calculated for the normal appearing WM. Mean MD was calculated for normal appearing GM. Magnetization transfer images were reoriented from sagittal to axial plane then skull stripped using the skull stripped T1-weighted images. Then, the images were used to generate the MT ratio (MTR): the ratio between the signal intensities obtained presaturation (M_o)

and postsaturation (M_s). This was calculated using the equation $MTR = 100*(M_o - M_s)/ M_o$. The values with MTR less than 20% were excluded since it is indicative of CSF. The MTR was restricted using the individual's WM and GM masks. Then, MTR whole brain histograms (256 bins, MT ratio between 20 and 100 with bin size: 0.313726) were computed for GM and WM separately. To obtain the relative peak height MTR for WM and GM separately, the histogram bin with the peak frequency was normalized by the total number of voxels in the segmented image.

7.2.5 Analyses

A total of 277 of 325 persons had the complete dataset of MRI markers (microstructural and macrostructural measures), TENG 3MS, and DSST score. Five subjects were removed because of bad tissue segmentation. There were no age- adjusted statistical differences ($p>0.05$) between men and women for DSST and TENG 3MS scores but race was statistical difference. There were no age- and gender- adjusted statistical differences ($p>0.05$) in race, TENG 3MS score or DSST score (Table 9) between subject included in this analysis (n=272) and subjects excluded from MRI scanning (n=390).

Age- and gender-adjusted Pearson correlations of potential covariates (brain MRI measures) and DSST were used to identify the covariates that would be retained for the multivariable linear regression models. Age- and gender-adjusted Pearson correlations were also used to test the associations between MRI variables.

Using age-, gender- and TENG 3M score- adjusted multivariable two-stage linear regression models, we tested the hypothesis that the MRI measures were associated with the DSST score independently of each other and to characterize the relative strengths of their

associations with the DSST score. In the first stage, age, gender and TENG 3MS score variables were entered using the forced entry method and in the second stage the MR measures were entered using the stepwise method. The age-adjusted associations between DSST score and micro-structural markers of white and gray matter abnormalities were also tested after stratification by gender-specific tertiles of brain atrophy and of WMH. All analyses were done using SPSS version 18.0 (SPSS, Inc. Chicago, IL).

7.3 COMPARISON OF DTI ANALYSIS METHODS

7.3.1 Participants

This analysis uses the same dataset that was analyzed in the study of relationship between micro-structural and macro-structural relationship (Section 7.2.1). These subjects were selected from 272 subjects who are part of Health ABC (Health, Aging and Body Composition) Study. The dataset used for empirical analysis (dataset A: 30 subjects) was randomly picked from the larger dataset and the subjects with lowest WMH were selected as part of the simulated dataset (dataset B: 25 subjects).

7.3.2 Image acquisition

All MRI scanning was performed on a 3T Siemens Tim Trio MR scanner at MR Research Center in University of Pittsburgh, using a Siemens 12-channel head coil. Magnetization-prepared rapid gradient echo (MPRAGE) T1-weighted images were acquired in the axial plane with TR=2300

ms, TE=3.43 ms, TI=900 ms, Flip angle= 9 deg, Slice Thickness= 1mm, FOV= 256*224 mm, voxel size= 1mm*1mm, matrix size= 256*224, number of slices=176. Fluid-attenuated inversion recovery (FLAIR) images were acquired in the axial plane with TR=9160 ms, TE=89 ms, TI=2500 ms, FA=150 deg, FOV= 256*212 mm**,** slice thickness=3 mm, matrix size=256*240, number of slices=48 slices, voxel size= 1mm*1mm. Diffusion Weighted Images (DTI) were acquired using single-short spin-echo sequence with the parameters TR=5300 ms, TE=88 ms, TI=2500 ms, Flip angle= 90 deg, FOV= 256*256 mm, two diffusion values of b=0 and 1000 s/mm, 12 diffusion directions, 4 repeats, 40 slices, matrix size =128*128, voxel size= 2mm*2mm, slice thickness= 3mm, GRAPPA=2. The MR images used in this study were checked by a radiologist for any unexpected findings and were excluded from the study.

7.3.3 DTI Preprocessing

Eddy current related distortion and head motion of each data set were corrected using an affine registration to a reference volume using tools available in FMRIB's Diffusion Toolbox (FDT; http://www.fmrib.ox.ac.uk/fsl/) [92]. Then, the tensor was diagonalized to estimate the three eigenvectors and the corresponding eigenvalues using DTIFIT tool in FDT. Maps of the DTI FA and MD were subsequently calculated [134].

7.3.3.1 FA Template

For this comparison, we used a standard-space image (FMRIB58-FA; http://www.fmrib.ox.ac.uk/fsl/) as the template [92]. The FMRIB58_FA is a high resolution average of 58 well-aligned good quality FA images of healthy subjects aged between 20-50. The image is available in 2*2*2 mm and 1*1*1mm resolution, we used the 1*1*1mm resolution which is in same space as commonly used template MNI152.

7.3.3.2 JHU white matter tract atlas

The JHU white-matter tractography atlas [169] was used in this comparison. Twenty different tracts were identified probabilistically by averaging the results of running deterministic tractography on 28 normal subjects (mean age 29, M: 17, F: 11). The JHU template is in MNI 152 template space. The other available atlases include the ICBM-DTI-81 white matter label atlas with 50 tracts identified using hand segmentation of tensor maps from 81 subjects. The ICBM-DTI-81 atlas was not used in this comparison.

7.3.3.3 Segmentation

Tissue segmentation was done using the FAST algorithm [167] in the FMRIB software library (http://www.fmrib.ox.ac.uk/fsl/). The high-resolution MPRAGE image is used as input for the segmentation process. The segmentation algorithm was based upon a hidden Markov random field model and the expectation–maximization algorithm [167].

7.3.3.4 Normalization

The FA maps for each subject were spatially normalized to the chosen FA template using FMRIB's Nonlinear Image Registration Tool (http://www.fmrib.ox.ac.uk/fsl/) [168]. This is done using a Levenberg-Marquardt modification of the Gauss-Newton method and by optimizing the registration problem.

7.3.4 Tissue-specific approach using linear registration

In this approach Figure 5, the high-resolution T1-weighted image (MPRAGE) is registered using linear 12-parameter affine transformation with FLIRT (http://www.fmrib.ox.ac.uk/fsl/) [92] to the b_o image. The linear registration was used for inter-subject registration and then the normalized T1-weighted image was segmented into tissue classes. The mask is then used to obtain diffusion measures (such as mean, median or histogram measures) from the calculated maps. For this comparison, we obtained mean fractional anisotropy for white matter without an FA threshold and with FA > 0.2.

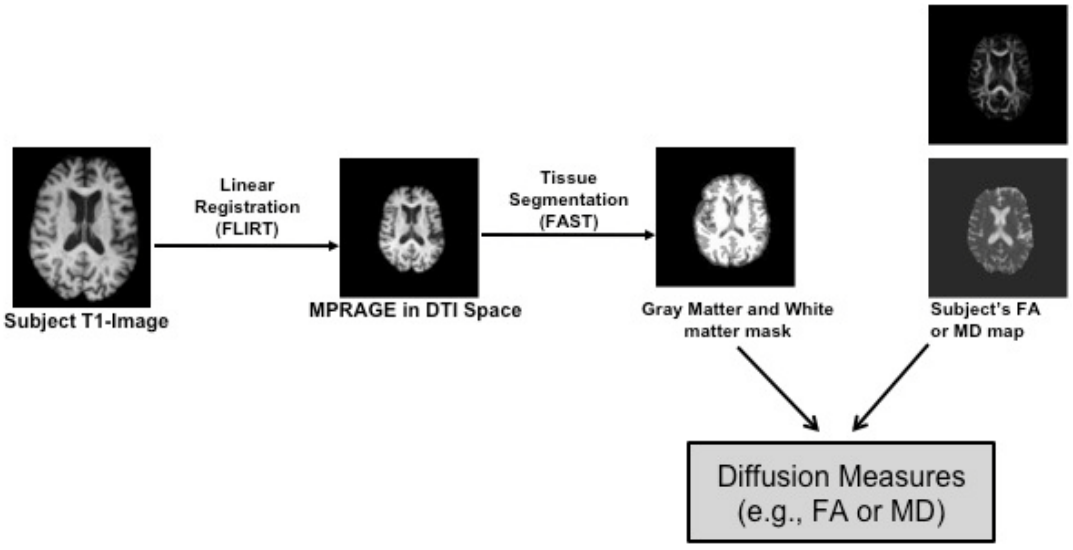

Figure 5. Scheme for tissue-specific approach using linear registration

7.3.5 Skeleton- based approach

Figure 6 shows the various steps used in this approach. The overall approach uses the framework of TBSS [105]. The T1-weighted image is registered to the b_o image using the linear registration. Then, the subject's FA image is registered to the template FA image using FNIRT registration. The transformation to the template is applied on the coregistered T1-weighted image and then segmentation is performed for localizing. The segmented mask is used on the skeleton with projected FA to obtain the diffusion measures (such as mean fractional anisotropy) with and without FA threshold. As the skeleton is in MNI 152 template space, other white matter templates such as the JHU white matter atlas can be used to localize specific tracts and obtain mean fractional anisotropy.

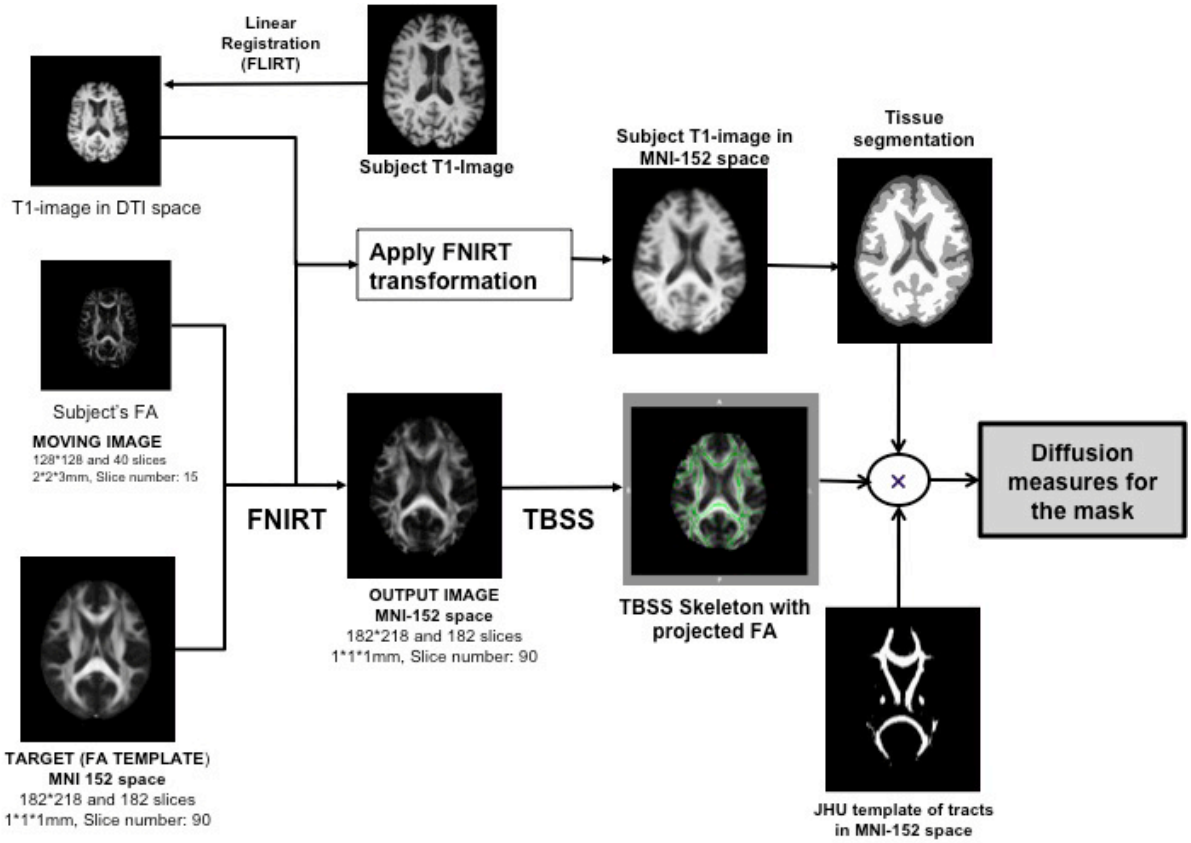

Figure 6. Scheme for skeleton-based approach

7.3.6 Automated template-based approach

This approach (Figure 7) follows the same framework of TBSS (Figure 6) so that the results can be compared. The T1-weighted image is registered to the b_o image using the linear registration. Then, the subject's FA image is registered to the template FA image using FNIRT registration. The transformation to the template is applied on the coregistered T1-weighted image and then segmentation is performed for localizing. The segmented mask is then used on the normalized subject's FA to obtain the diffusion measures (such as mean fractional anisotropy) with and without FA threshold. Other white matter atlases can be used for this approach also.

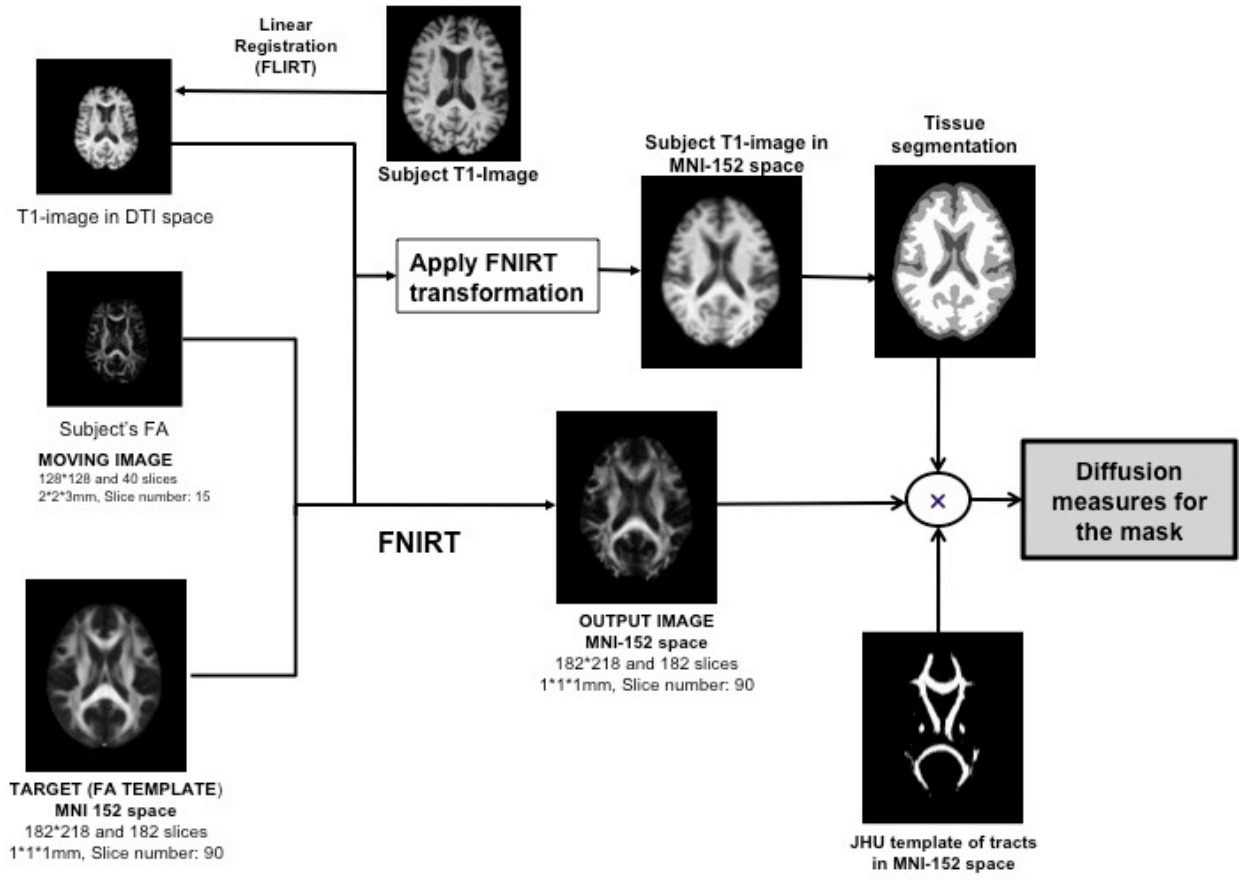

Figure 7. Scheme for automated template-based approach.

7.3.7 WMH simulation

WMH extraction was done using the method explained in section 5.6. The FLAIR image and WMH mask were linearly registered to individual subject's b_o image using 12-parameter affine transformation (FLIRT; http://www.fmrib.ox.ac.uk/fsl/)[92]. Using 24 subjects from dataset A with highest WMH, we obtained the mean and standard deviation of eigen values (λ_1, λ_2, λ_3) from CSF, white matter, and WMH. Alexander et al. 2001 [170] defined eigen values using synthetic data as normally distributed. Thus, normal distribution was assumed for distribution of eigen values (λ_1, λ_2, λ_3) for various tissue types in this study. We looked at the mean graphs from the data obtained from 24 subjects, but statistical testing to prove normal distribution was not done. Then, white noise with gaussian/normal distribution using parameters estimated for WMH from dataset A with M=0 was added to normal appearing WM in dataset B. The noise was added to the eigen value images in dataset B to simulate WMH features in eigen value images. Spherical shaped noise is added to the 3D image in a manually selected location and the size is randomized across dataset B. The size distribution was similar to dataset A. So, the noise image with normally distributed white noise can be defined as: $\mathrm{Im}g_n = \mathrm{Im}g_o + \sqrt{\mathrm{var}} * rand(size) + M$, where $\mathrm{Img_n}$ is noise image, $\mathrm{Img_o}$ is original image, var is the variance of the noise distribution, size is the size of the matrix and M is the mean of the noise distribution. The noise distribution was thresholded using the upper and lower limits for 99% of area under the normal distribution curve. The maps of the FA and MD were calculated using the noise added eigen value images and number of voxels with added noise were measured. Finally, the image analysis (skeleton based and automated template-based approach) was repeated on dataset B with noise.

7.3.8 Analyses

The mean fractional anisotropy from dataset A and the mean fractional anisotropy from dataset B with noise were calculated as a measure of whole brain white matter integrity. The mean fractional anisotropy was obtained with and without FA threshold from the three approaches explained above. Then, the FA diffusion measures were correlated with the WMH measures in both datasets. Pearson's correlation coefficients were reported with significant differences for both datasets. All analyses were done using SPSS version 18.0 (SPSS, Inc. Chicago, IL).

8.0 RESULTS

8.1 EFFECT OF STRUCTURAL DAMAGE ON FUNCTIONAL ACTIVATION

Of the thirty participants who received a brain fMRI, two were excluded from this analysis due to incomplete behavioral data and three were excluded for excessive motion artifacts (±3.5 mm in x, y, or z translation or ±3° pitch, roll or yaw). Table 3 shows characteristics for the participants included in this analysis. Associations of accuracy with other measures (Table 3) were in the expected direction, but were not significant ($p>0.05$). Accuracy and response time of the sDSST were significantly correlated with score on the pencil and paper DSST test (Spearman ρ: 0.36, $p=0.03$ and 0.66, $p<0.0001$).

8.1.1 Spatial distribution of sDSST-related brain fMRI activation and relationship with accuracy

Brain peak activation while performing the sDSST was significantly greater than brain peak activation while performing the control condition (cluster probability α <0.001) for ECF regions within the prefrontal cortex bilaterally, and for left posterior parietal regions (BA 7,40) independent of group assignment and atrophy index (Table 4, Figure 8). Analyses to test the

opposite direction of association (main effect of control condition>sDSST) were all not significant.

Table 3. Participant's characteristics (n=25)

Measure	Mean (SD)	Correlations with imaging markers of brain structure Spearman ρ (p value)	
		Atrophy index[1]	**WMH[2]**
Age, years	81.67 (3.47)	0.58 (p=0.001)	0.61 (p<0.0001)
Minimental Score	27.52 (1.9)	0.04 (p=0.4)	-0.26 (p=0.09)
Pencil and Paper DSST, correct points	53.48 (17.12)	-0.48 (p=0.005)	-0.49 (p=0.004)
sDSST Accuracy, %	0.90 (0.13)	-0.17 (p=0.2)	-0.77 (p<0.0001)
sDSST response time, milliseconds	1640.56 (314.87)	0.29 (p=0.07)	0.62 (p<0.0001)
IMAGING MARKERS OF BRAIN STRUCTURE			
Atrophy index[1]	0.72 (0.08)	-	0.16 (p=0.2)
WMH[2]	0.50 (0.61)	0.16 (p=0.2)	-

1. Atrophy index: (Gray Matter volume/Cerebrospinal fluid volume)$^{-1}$
2. White Matter Hyperintensities Measure (WMH): WMH voxel count divided by sum of gray matter and white matter voxel counts.

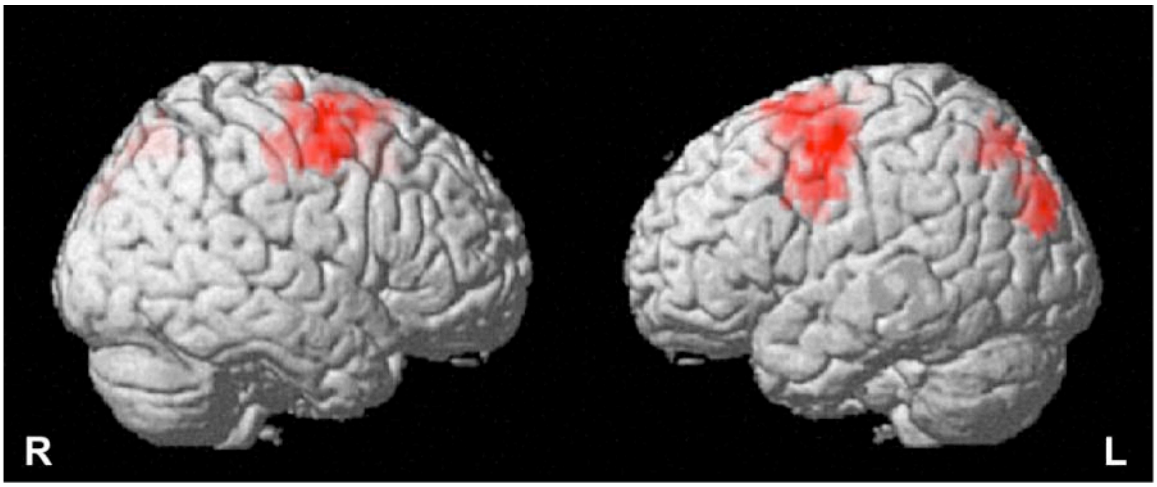

Figure 8. Spatial distribution of brain functional MRI activation for sDSST > Control condition.
T maps of analysis of task-related activity adjusted for group assignment and atrophy index. Threshold was at t=1.71 and cluster probability (α) < 0.001. See **Table 4** for list of regions.

Table 4. Spatial distribution of brain functional MRI activation for task-related activity.

Regions	Cluster Size	Peak Z-Score	Talairach Coordinate for Peak Z-Score
Regions during sDSST>Control Condition (task-related)			
Left posterior parietal cortex	480	2.76	-19.8, -63.53, 50.15[1]
Right prefrontal cortex	770	4.15	23.76. 5.11, 63.30[2]
Left prefrontal cortex and anterior cingulate cortex	1367	4.58	-29.7. 2.62, 52.37[3]
Regions during Control>sDSST Condition			
No significant voxels			

This table reports the spatial distribution of task-related activity (the sDSST > control condition contrast) with the mean group activation including the size of cluster, the maximum Z statistic for the cluster, and the location of the maximum Z statistic in Talairach coordinates. The analyses were adjusted for group assignment and atrophy index. The corrected alpha is the probability of a false positive detection based on the combination of individual voxel probability thresholding and minimum cluster size thresholding.
1. This cluster had its peak in the left precuenus (BA 7) extended to superior parietal gyrus (BA 7,40) and angular gyrus (BA 39).
2. This cluster had its peak in the right superior frontal gyrus (BA 6) and covered the middle frontal gyrus (BA6, 9) and precentral gyrus (BA 4,6)
3. This cluster had its peak in the left middle frontal gyrus (BA 6) and covered the anterior cingulate cortex (BA 24, 32) extended to medial frontal and precentral gyrus (BA 6), and inferior frontal gyrus (BA 9).

The correlation of fMRI signal with accuracy was positive and significant (Figure 9 and Table 5). For greater accuracy, the fMRI activation was significantly greater within ECF-related regions: left prefrontal cortex and right parietal cortex. Activation also extended caudally to the left sensori-motor cortex (pre- and post-central gyri) and left superior temporal gyrus. All analyses were independent of group assignment, sDSST response time, and atrophy index. Analyses repeated using a voxel-wise and region-of-interest approach consistently showed similar results.

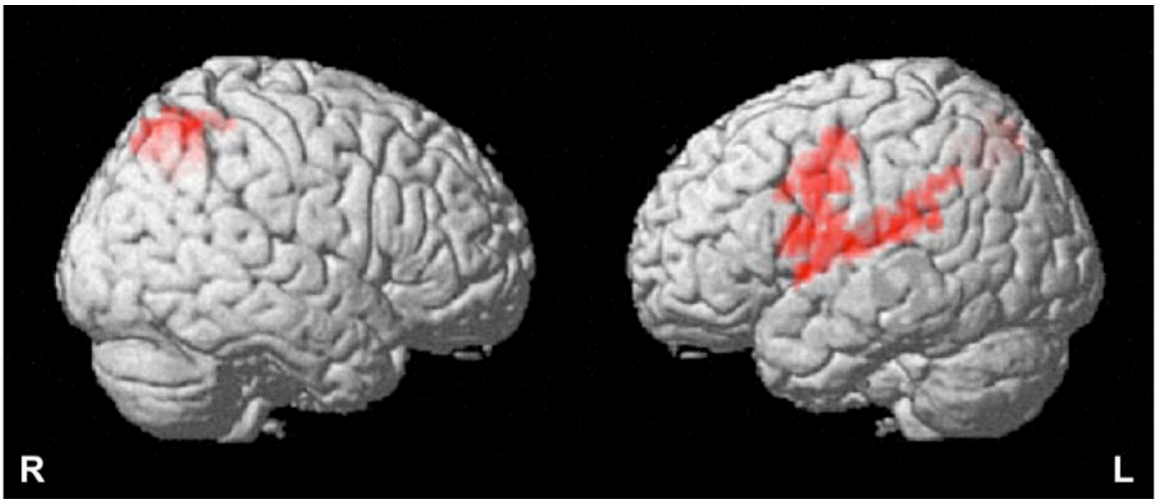

Figure 9. Spatial distribution of brain functional MRI activation that were positively correlated with accuracy during sDSST task performance.
T maps of task-related activity analysis positively correlated with accuracy during sDSST task performance. Adjusted for group assignment, atrophy index and sDSST response time. Threshold was at t= 1. 71 and cluster probability (α) < 0.001. See **Table 5** for list of regions.

8.1.2 Relationship of fMRI activation, accuracy and connectivity abnormalities

Greater WMH volume and atrophy index were significantly associated with older age and lower score on the pencil and paper DSST (Table 3). Greater WMH was also associated with lower accuracy and longer response times on the sDSST. The sDSST association with atrophy index was in the expected direction though not statistically significant (Table 3). WMH volume was inversely correlated with the fMRI signal in ECF-related regions bilaterally (anterior cingulate

cortex), as well as bilateral sensori-motor and right superior temporal gyrus (Figure 10 and Table 6). Atrophy index was not associated with fMRI brain activation during sDSST performance.

Table 5. Spatial distribution of correlation of accuracy with brain functional MRI activation during sDSST task performance.

Regions	Cluster Size	Peak Z-Score	Talairach Coordinate for Peak Z-Score
Regions positively correlated with accuracy during sDSST performance			
Left prefrontal cortex	968	3.25	-45.54, -8.17, 30.8[1]
Right posterior parietal cortex	451	2.84	35.64. -53.56, 55.18[2]
Regions negatively correlated with accuracy during sDSST performance			
No significant voxels			

This table reports the spatial distribution of the association of accuracy with the mean group activation (obtained from the sDSST > control condition contrast) including the size of cluster, the maximum Z statistic for the cluster and the location of the maximum Z statistic in Talairach coordinates. The analyses were adjusted for group assignment, atrophy index, and sDSST response time. The corrected alpha is the probability of a false positive detection based on the combination of individual voxel probability thresholding and minimum cluster size thresholding.

1. This cluster had its peak in the left precentral gyrus (BA 6) and extended to middle and prefrontal gyri (BA 4, 9,44), and covered postcentral gyrus (BA 40,43), and superior temporal gyrus (BA 42).
2. This cluster had its peak in the right precuneus (BA 7) and extended to the inferior parietal gyrus (BA 40).

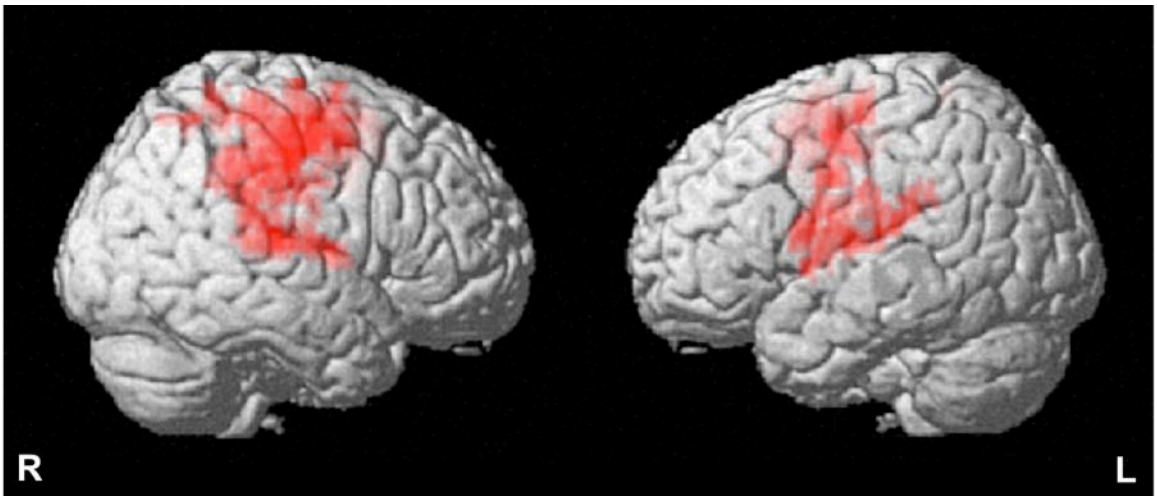

Figure 10. Spatial distribution of functional brain MRI activation showing negative correlation with WMH burden. T maps of analysis to identify the regions that showed negative correlation between WMH burden and functional MRI activation (sDSST > control condition); adjusted for atrophy index and group assignment. Threshold was at t= 1. 71 and cluster probability (α) < 0.001. See **Table 6** for list of regions.

There was a significant and positive interaction (Figure 11 and Table 7) between accuracy and WMH volume within specific ECF-related (left posterior parietal) and non ECF-related (left sensori-motor regions) regions. The association of WMH with fMRI activation varied with accuracy. Specifically, there was a positive correlation between WMH and fMRI signal as accuracy increased. In additional exploratory analyses within the group with WMH volume above the median, greater accuracy was associated with greater bilateral activation in ECF regions (posterior parietal and cingulate cortex), and it extended to sensori-motor regions (Figure 12 and Table 8).

Table 6. Spatial distribution of correlation of WMH volume with brain functional MRI activation during sDSST task performance.

Regions	Cluster Size	Peak Z-Score	Talairach Coordinate for Peak Z-Score
Regions Negatively Correlated with WMH burden			
Left anterior cingulate cortex	524	4.05	-3.96, -1.25, 52.56[1]
Right anterior cingulate cortex	561	3.95	19.8, -17.58, 36.8[2]
Left prefrontal and parietal cortex	885	4.19	-23.76, -7.61,41.83[3]
Right prefrontal and parietal cortex	1976	4.63	29.7, -9.55, 41.93[4]
Regions positively correlated with WMH burden			
No significant voxels			

This table reports the regions that show correlation between the structural measure (WMH measure) and task (sDSST > control condition) adjusted for atrophy index and group assignment, including the size of cluster, the maximum Z statistic for the cluster, and the location of the maximum Z statistic in Talairach coordinates. The corrected alpha is the probability of a false positive detection based on the combination of individual voxel probability thresholding and minimum cluster size thresholding.

1. This cluster had its peak in the left medial frontal gyrus (BA 6) and covered the cingulate gyrus (BA 24, 32) and superior frontal gyrus (BA 6).
2. This cluster had its peak in the right cingulate gyrus (BA 24, 32) and extended to medial frontal gyrus and superior frontal gyrus (BA 6).
3. This cluster had its peak in the left middle frontal gyrus (BA 6) and covered the precentral gyrus (BA 44), postcentral gyrus (BA 3, 40, 43) and inferior parietal gyrus (BA 40).
4. This cluster had its peak in the right middle frontal gyrus (BA 6) and covered the precentral gyrus (BA 4, 6, 44), superior frontal gyrus (BA 6), postcentral gyrus (BA 3,40,43) and superior temporal gyrus (BA 42).

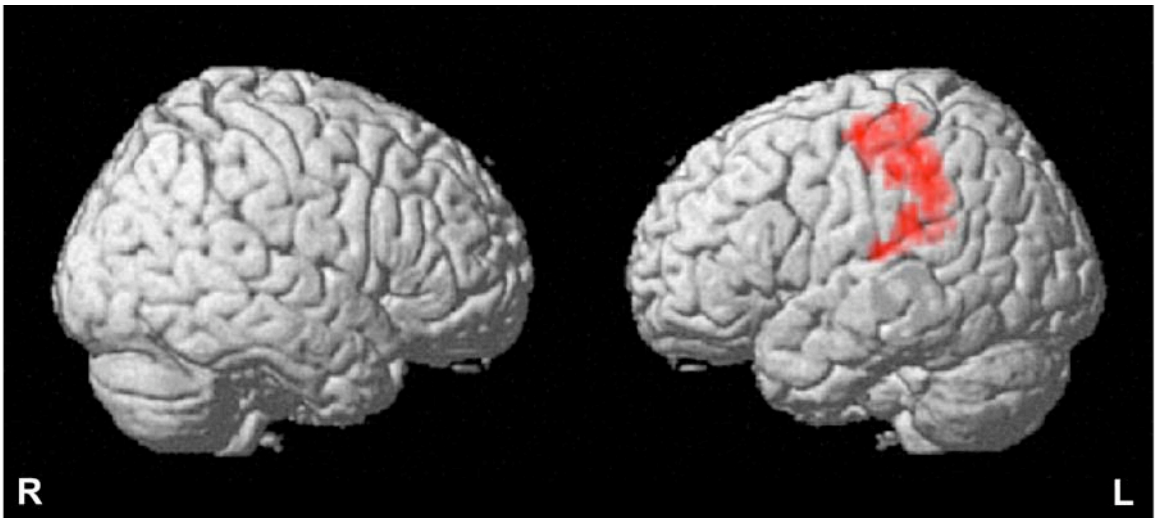

Figure 11. Spatial distribution of functional brain MRI activation showing positive interaction of WMH burden by accuracy during sDSST task.
T maps of analysis to identify the regions that showed interaction of WMH volume by accuracy during sDSST task. Analyses were adjusted for group assignment, atrophy and sDSST response time. Threshold was at t= 1. 71 and cluster probability (alpha) < 0.001. See **Table 7** for list of regions.

Table 7. Spatial distribution of functional brain MRI activation showing significant interaction of WMH burden by accuracy during sDSST task.

Regions	Cluster Size	Peak Z-Score	Talairach Coordinate for Peak Z-Score
Regions with positive interaction term (Accuracy by WMH)			
Left posterior parietal cortex	777	3.08	-37.62, -27.96, 62.19[1]
Regions with negative interaction term (Accuracy by WMH)			
No significant voxels			

This table reports the regions that showed interaction of WMH volume by accuracy during the sDSST task, including the size of cluster, the maximum Z statistic for the cluster and the location of the maximum Z statistic in Talairach coordinates. Analyses were adjusted for group assignment, atrophy index and sDSST response time. The corrected alpha is the probability of a false positive detection based on the combination of individual voxel probability thresholding and minimum cluster size thresholding.
1. This cluster had its peak in the left postcentral gyrus (BA 3) covered the inferior parietal cortex (BA 40) and postcentral gyrus (BA 2 and 3) extended to precentral gyrus (BA 4).

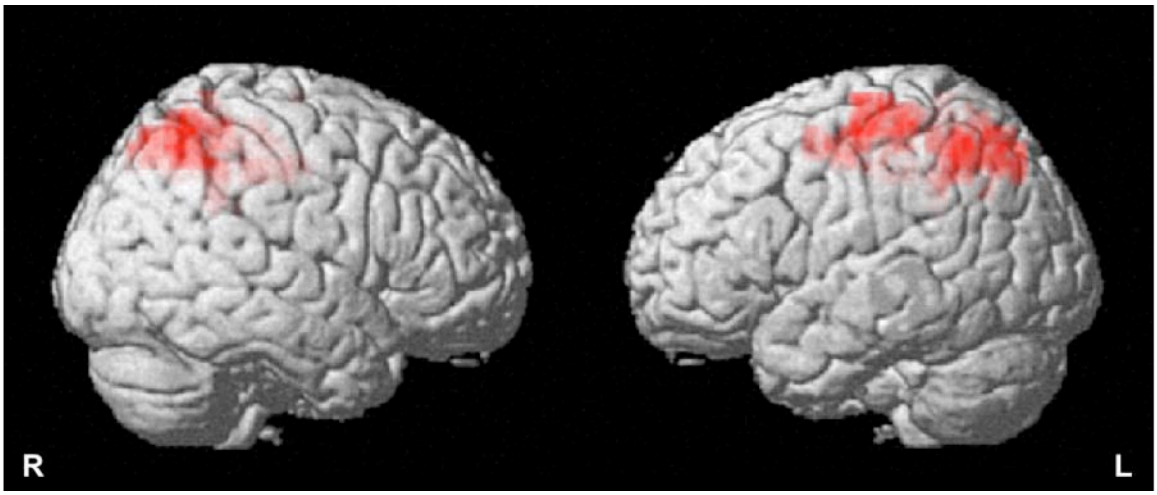

Figure 12. Spatial distribution of brain functional MRI activation that were positively correlated with accuracy during sDSST task performance in a group with greater WMH (> median).
T maps of analysis of task-related activity positively correlated with accuracy during sDSST task performance performance in a group with greater WMH (> median). Adjusted for group assignment, atrophy index and sDSST response time. Threshold was at t= 1. 71 and cluster probability (alpha) < 0.001. See **Table 8** for list of regions.

Table 8. Spatial distribution of correlation of accuracy with brain functional MRI activation during sDSST task performance in a group with greater WMH (>median).

Regions	Cluster Size	Peak Z-Score	Talairach Coordinate for Peak Z-Score
Regions positively correlated with accuracy during sDSST performance			
Left posterior parietal cortex	970	4.21	-5.94, -53.7, 52.42[1]
Right posterior parietal cortex	1266	3.17	13.86, -49.83, 52.23[2]
Left sensorimotor area	454	2.99	-33.66. -20.07, 64.56[3]
Regions negatively correlated with accuracy during sDSST performance			
No significant voxels			

This table reports the spatial distribution of the association of accuracy with the mean group activation (obtained from the sDSST > control condition contrast) in a group with greater WMH (>median), including the size of cluster, the maximum Z statistic for the cluster and the location of the maximum Z statistic in Talairach coordinates. The analyses were adjusted for group assignment, atrophy index and sDSST response time. The corrected alpha is the probability of a false positive detection based on the combination of individual voxel probability thresholding and minimum cluster size thresholding.
1. This cluster had its peak in the left precuneus (BA 7) extended to inferior parietal gyrus (BA 40) and superior parietal gyrus (BA7) covered cingulate gyrus.
2. This cluster had its peak in the right precuneus (BA 7) and extended to the inferior parietal gyrus (BA 40) and superior parietal gyrus (BA 7) covered cingulate gyrus.
3. This cluster had its peak in the left precentral gyrus (BA 6) and extended to postcentral gyrus (BA 2,3) and precentral gyrus (BA 4,6).

8.2 RELATIONSHIP OF MACRO- AND MICRO- STRUCTURAL CHANGES

Table 9 shows the MRI characteristics of MRI markers (macro- and micro- structural abnormalities). Age-adjusted significant differences between men and women were seen in atrophy index, white matter micro-structural MRI markers (WM_FRPH and WM_MRPH), and gray matter micro-structural MRI markers (GM_MD and GM_MRPH). The MRI indices (GM_AI, GM_MD) were significantly greater in men than women.

Table 9. MRI characteristics of the 272 subjects

			N= 272 Subjects **Mean of MRI index (SD)**
MRI markers of macro-structural abnormalities	*White Matter*	**Normalized White Matter Hyperintensities (WM_WMH)** [a]	0.0063 (0.0079)
	Gray Matter	**Brain Atrophy Index (GM_AI)** [b]	0.6999 (0.0212)‡
MRI markers of micro-structural abnormalities	*White Matter*	**Relative Peak Height FA (WM_FRPH)**	0.0413(0.0058)‡
		Mean Diffusivity (WM_MD)	0.0008 (0.00003)
		Relative Peak Height MTR (WM_MRPH)	0.0385 (0.007)‡
	Gray Matter	**Mean Diffusivity (GM_MD)**	0.0013(0.0001)‡
		Relative Peak Height MTR (GM_MRPH)	0.0276 (0.0042)‡

‡Age-adjusted differences of men vs. women significant at $p < 0.05$ (Two-tailed t-test).
[a] Computed as WMH voxel count divided by sum of gray matter and white matter voxel counts.
[b] Computed as (intracranial volume – gray matter volume)/intracranial volume.

Table 10 shows the correlation between MRI measures and DSST when adjusted for age and gender. When controlled for age and gender, all the MRI measures showed significant correlations with DSST in the expected direction. Thus, all the MRI measures are potential covariates in the regression model with DSST as the outcome variable. In a stepwise regression of all MR indices controlled for age and gender, the MRI indices (WM_MRPH and WM_FRPH) were significantly related with DSST. WM_MRPH and WM_FRPH accounted for 9.6% and 2% of DSST variability respectively when controlled for age and gender, which accounted for 5.1% of DSST variability. Table 11 shows a cross-correlation matrix of all the MRI measures used to characterize the degree to which the different MRI measures correlate with each other. The table indicates that all but one of the pair-wise correlations showed a significant relationship. These correlations were all significant when controlled for age and gender. The only exception was the gray matter MTR RPH (GM_MRPH), which was not correlated with WMH.

Table 10. Relationship between MRI measures and DSST controlled for age and gender

			DSST		
			R*	**Standardized beta****	**Standard Error****
MRI markers of macro-structural abnormalities	*White Matter*	**WM_WMH**	-0.190†		
	Gray Matter	**GM_AI**	-0.211‡		
MRI markers of micro-structural abnormalities	*White Matter*	**WM_FRPH**	-0.257‡	-0.157†	145.29
		WM_MD	-0.204‡		
		WM_MRPH	0.317‡	0.255‡	120.32
	Gray Matter	**GM_MD**	-0.170†		
		GM_MRPH	0.161†		

*Pearson's correlation coefficient; ** Stepwise regression of all MRI measures with DSST, controlled for age and gender.‡: p<=0.001; †: 0.01<=p<0.001 (Two-tailed t-test)

Table 11. Interrelationship of MRI measures controlled for age and gender

		MRI markers of macro-structural abnormalities		MRI markers of micro-structural abnormalities				
		WM WMH	**GM AI**	**WM FRPH**	**WM MD**	**WM MRPH**	**GM MD**	**GM MRPH**
MRI markers of macro-structural abnormalities	**WM WMH**		0.176†	0.524‡	0.361‡	-0.215‡	0.232‡	-0.065
	GM AI			0.275‡	0.334‡	-0.280‡	0.478‡	-0.283‡
MRI markers of micro-structural abnormalities	**WM FRPH**				0.772‡	-0.395‡	0.420‡	-0.144†
	WM MD					-0.418‡	0.664‡	-0.209‡
	WM MRPH						-0.418‡	0.458‡
	GM MD							-0.258‡
	GM MRPH							

Pearson's correlation coefficient, ‡: p<=0.001; †: 0.05<=p<0.001 (Two-tailed t-test)

To further analyze the relationship of macro-structural and micro-structural MRI markers for gray and white matter separately, standardized Z-scores of the micro- and macro- structural indices were plotted. Figure 13 shows that subjects having lower WMH (close to zero) have considerable variability in their whole-brain micro-structural MRI markers. This suggests that for individuals with low WMH burden, the micro-structural abnormalities of white matter could be a better indicator of cognitive aging than white matter hyperintensities. As shown in Figure 13, the plot of gray matter measures shows a linear change with increasing atrophy index.

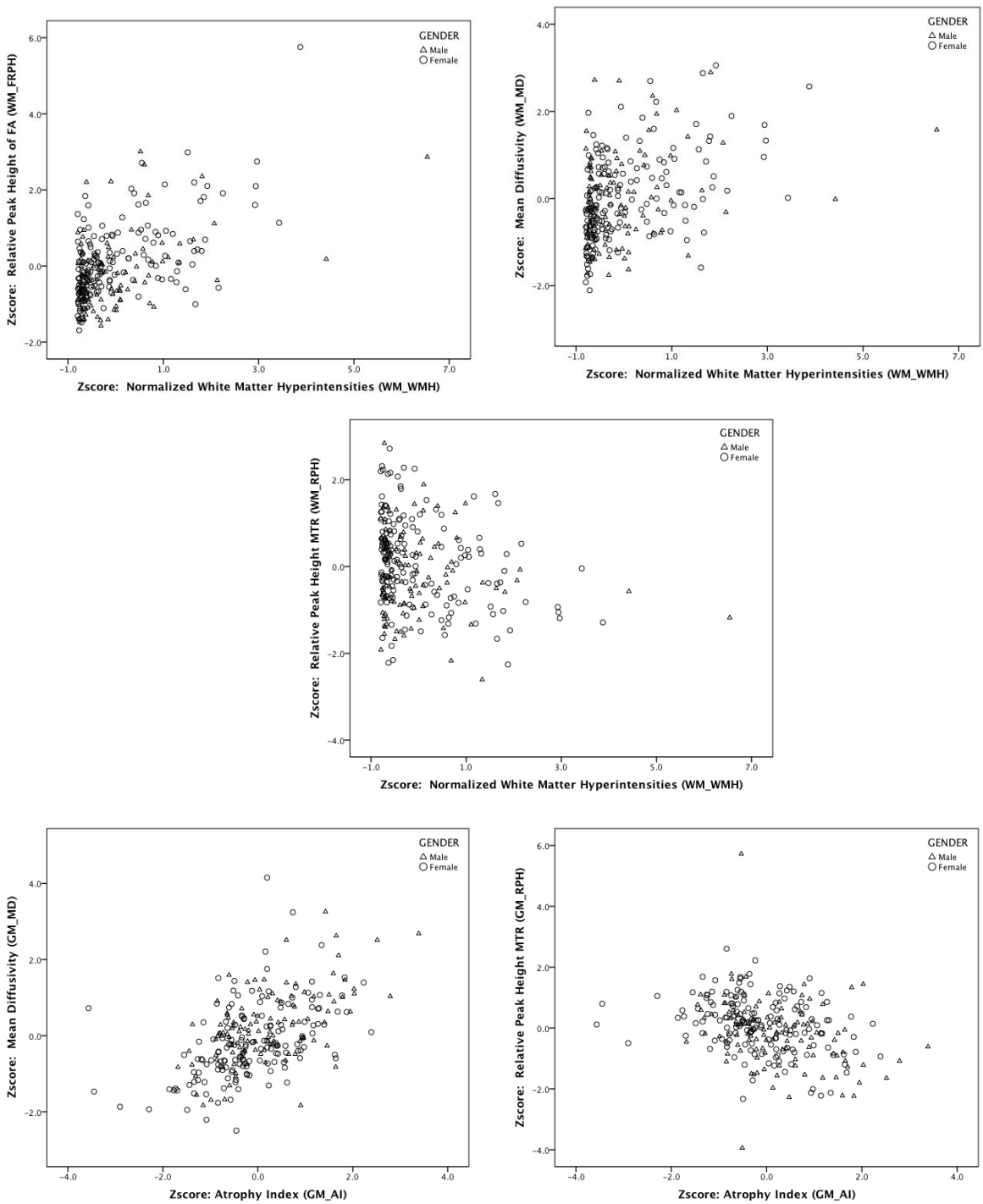

Figure 13. Plot of MRI markers of macro-structural and micro-structural abnormalities.

Another way to look at these relationships is to use all the MRI markers in a two-stage multivariable linear regression models and see which MRI markers account for the greatest variance in DSST. Age, gender, and TENG 3MS score were entered as variables using the forced

entry method in the first stage. Then, in the second stage these MRI measures were entered using the stepwise method. The stepwise regression model was used over other regression models (such as forced entry model), as it uses an automated procedure to choose the predictive variables. Table 12 shows three models: age adjusted in model 1, age and TENG 3MS adjusted in model 2; and age, gender, and TENG 3MS adjusted in model 3. Age, gender, and TENG 3MS score account for 26.6% of variability in DSST, with TENG 3MS contributing about 21.5%. According to the automatic step-wise procedure, the white matter MRI micro-structural measures (MTR RPH 8.4% and FA RPH 0.9%) accounted for the greatest variance of DSST suggesting that these markers are the most sensitive to information processing speed changes in aging.

Then, we looked at the relationships between all MRI markers to observe how the markers are associated with DSST in the different groups divided by gender specific tertiles based on their WMH burden (Table 13) and atrophy index (AI) (Table 14) adjusted for age. For both WMH and atrophy index based gender specific tertile groups, only the most sensitive MRI marker (WM_MRPH) from the linear regression was significantly correlated in all tertiles. All other MRI variables were significantly correlated in one or two tertiles. For example, in WMH gender specific tertiles, the WM_FRPH was significantly correlated in 1st and 3rd tertile groups; and in AI gender specific tertiles the WM_FRPH was significantly correlated in 2nd and 3rd tertile. However, GM_MD was not significant in any of the AI groups. This further shows a pattern of how these markers are related to each other, since certain micro-structural markers pick up stronger associations when there is very little macro-structural WMH change and vice versa. This also shows how these measures may be particularly useful at complementing the atrophy index.

Table 12. Two-stage regression result of MRI indices and DSST

	Variable	*Standardized beta*	*(95% CI) Standard Error**	R^2	R^2 *Change*
Model 1 **First Stage:** Age **Second Stage:** All MRI indices (stepwise)	AGE	-0.16	(-1.36, -0.24) 0.28	0.051	**0.051**
	WM_MRPH	0.254	(260.42, 721.12) 116.99	0.144	**0.094**
	WM_FRPH	-0.158	(-640.77, -91.74) 139.42	0.166	**0.021**
Model 2 **First Stage:** Age, TENG 3MS **Second Stage:** All MRI indices (stepwise)	AGE	-0.097	(-0.98, 0.01) 0.25	0.265	**0.265**
	TENG 3MS	0.459	(0.72, 1.12) 0.10		
	WM_MRPH	0.295	(379.77, 760.30) 96.63	0.349	**0.084**
Model 3 **First Stage:** Age, Gender, TENG 3MS **Second Stage:** All MRI indices (stepwise)	AGE	-0.090	(-0.95,0.04) 0.254	0.266	**0.266**
	GENDER	0.017	(-2.31,3.26) 1.417		
	TENG 3MS	0.449	(0.70, 1.1) 0.101		
	WM_MRPH	0.254	(282.27, 698.46) 105.689	0.349	**0.084**
	WM_FRPH	-0.110	(-506.62, -1.76) 128.207	0.359	**0.009**

* Unstandardized Coefficients; Dependent Variable: Digit Symbol Substitution Score

Model 1: Age was entered at the first stage, followed by step-wise of MRI indices at the second stage.

Model 2: Age and TENG 3MS was entered at the first stage, followed by step-wise of MRI indices at the second stage.

Model 3: Age, Gender and TENG 3MS was entered at the first stage, followed by step-wise of MRI indices at the second stage.

Table 13. Relationship between MRI markers and DSST within gender specific WMH tertiles controlled for age

		Pearson's Correlation Coefficient					
		White Matter MRI measures			Gray Matter MRI measures		
		WM FRPH	**WM MD**	**WM MRPH**	**GM AI**	**GM MD**	**GM MRPH**
Lowest WMH 1st WMH Tertile (91 subjects)	**DSST**	-0.249*	-0.234*	0.274**	-0.209*	-0.205*	0.050
2nd WMH Tertile (90 subjects)	**DSST**	-0.069	-0.089	0.229*	-0.146	-0.045	0.206*
Highest WMH 3rd WMH Tertile (91 subjects)	**DSST**	-0.283**	-0.183	0.414***	-0.282**	-0.215*	0.227*

*: 0.01<p<=0.05; **: 0.001<p<=0.01; ***: p<=0.001 (Two-tailed t-test)

Table 14. Relationship between MRI markers and DSST within gender specific AI tertiles controlled for age

		Pearson's Correlation Coefficient					
		White Matter MRI measures				Gray Matter MRI measures	
		WM WMH	**WM FRPH**	**WM MD**	**WM MRPH**	**GM MD**	**GM MRPH**
Lowest AI 1st AI Tertile (90 subjects)	**DSST**	-0.171	-0.086	-0.076	0.249*	0.012	0.035
2nd AI Tertile (91 subjects)	**DSST**	-0.079	-0.309**	-0.191	0.301**	-0.159	-0.018
Highest AI 3rd AI Tertile (91 subjects)	**DSST**	-0.256*	-0.251*	-0.2	0.309**	-0.157	0.307**

*: 0.01<p<=0.05; **: 0.001<p<=0.01; ***: p<=0.001 (Two-tailed t-test)

8.3 COMPARISON OF DTI ANALYSIS METHODS

Table 15 provides demographics for both the datasets (A and B). Both datasets have similar parameters, but significantly different WMH measures as expected.

Table 15. Demographic data for the subjects

	Dataset A	**Dataset B**
Number of subjects	30	25
Age	83.301 (2.354)	82.504 (1.541)
DSST	38.433 (12.031)	39.280 (12.208)
TENG-3MS	92.567 (6.937)	94.440 (4.727)
Race	14 White	14 White
Gender	15 Female	18 Female
White matter hyperintensities (WMH)	0.0046 (0.0054)	0.00027(0.00018)

Table 16 shows the correlation between mean FA as a measure of white matter integrity and WMH measure. The measures compared were obtained for a whole-brain and JHU atlas using the tissue-specific with linear registration, skeleton-based and automated template-based approaches. The automated template-based approach showed the best correlation with and without FA threshold in dataset A.

Table 16. Correlation between FA measures and WMH in dataset A

	Mean FA for WM using TS *	Mean FA for WM using TS **	Mean FA for WM using AT *	Mean FA for WM using AT **	Mean FA for JHU atlas using AT*	Mean FA for WM using SB *	Mean FA for WM using SB **	Mean FA for JHU atlas using SB*
WMH burden (Pearson's Coefficient and p-value)	-0.305 < .051	-0.266 < .078	-0.444 < .007	-0.344 < .031	-0.412 < .012	-0.045 < .407	-0.031 < .435	-0.016 < .466

Pearsons coefficient and one-tailed t-test
*: Voxel included in mean FA calculation was restricted using white matter mask
**: Voxel included in mean FA calculation was restricted using white matter mask and FA> 0.2
TS: Tissue-specific approach using linear registration
AT: Automated template-based approach
SB: Skeleton-based approach

Figure 14 shows the comparison of eigen values (λ_1, λ_2, λ_3) for CSF, normal appearing WM, and WMH. The primary eigen value (λ_1) is greater than the other two eigen values, and the second eigen value (λ_2) is greater than the third eigen value (λ_3). Also, the whole-brain CSF has highest eigen values (λ_1, λ_2, λ_3), and WMH has higher eigen values than the normal appearing WM.

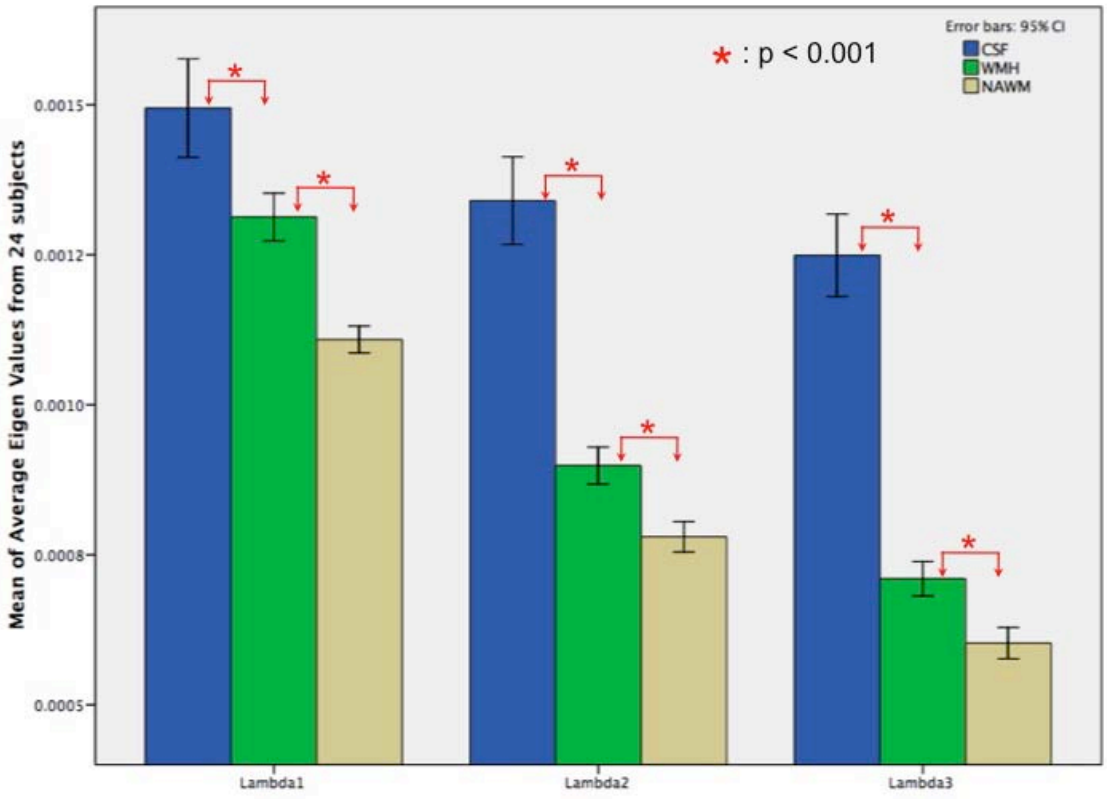

Figure 14. Comparison of eigen values (λ_1, λ_2, λ_3) in CSF, normal appearing WM, WMH

Figure 15 shows the comparison of mean FA and MD before and after noise in a region where noise was added in a subject's eigen value image. It shows decreased FA and increased MD as expected in WMH voxels. This supports that adding noise to eigen value images in a specific location can recreate eigen values similar to voxels in subject's with WMH.

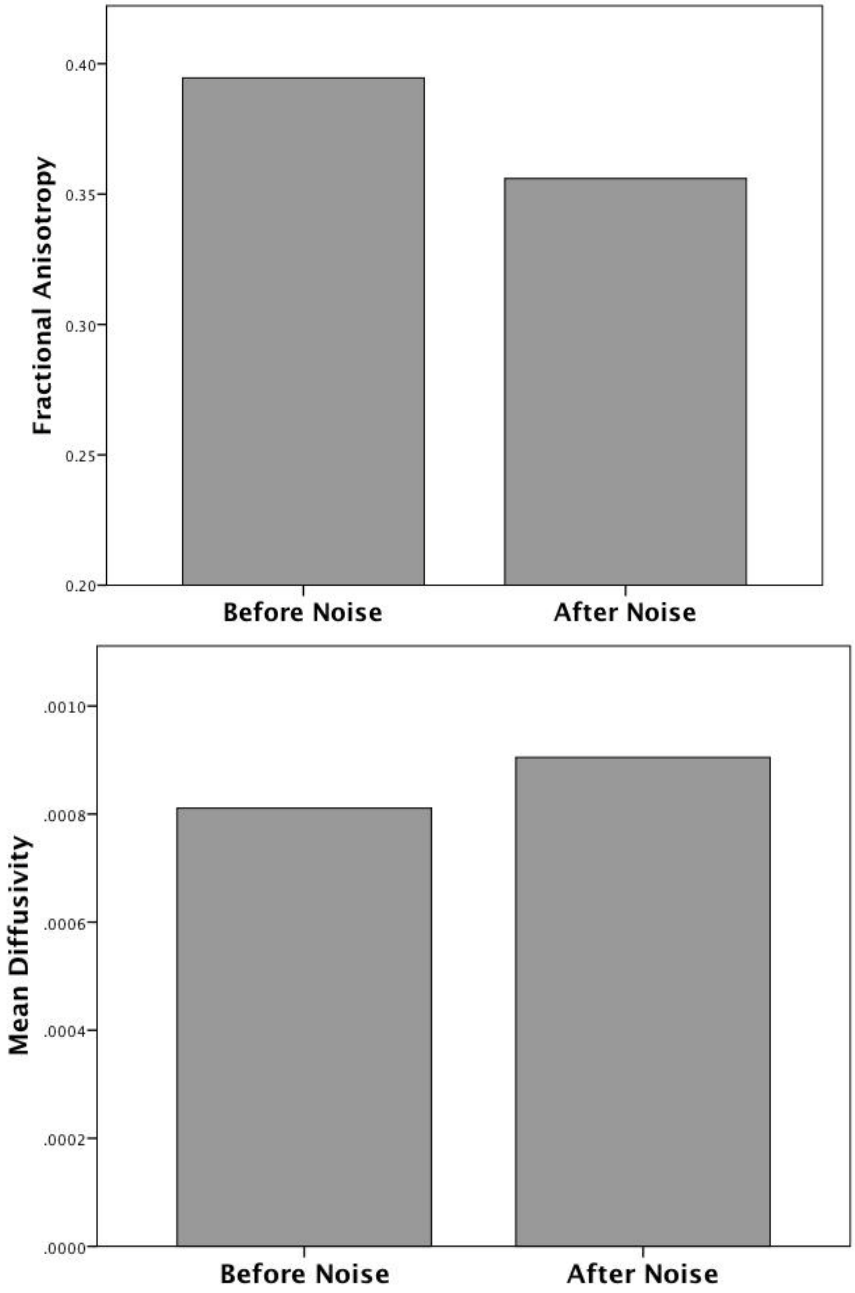

Figure 15. Fractional Anisotropy and Mean Diffusivity measures before and after noise

Table 17 shows the correlation between mean FA as a measure of white matter integrity obtained after adding noise and WMH measure. The measures compared were obtained from a whole-brain and JHU atlas using the tissue-specific with linear registration, skeleton-based, and automated template-based approaches. The automated template-based approach showed the best correlation with or without FA threshold in dataset B (similar to dataset A; see Table 16).

Table 17. Correlation between FA measures and WMH in dataset B after noise

	Mean FA for WM using TS *	Mean FA for WM using TS **	Mean FA for WM using AT *	Mean FA for WM using AT **	Mean FA for JHU atlas using AT*	Mean FA for WM using SB *	Mean FA for WM using SB **	Mean FA for JHU atlas using SB*
WMH burden (Pearson's Coefficient and p-value)	-0.265 < .04	-0.242 < .08	-0.465 < .006	-0.376 < .02	-0.424 < .012	-0.047 < .427	-0.038 < .355	-0.038 < .356

Pearsons coefficient and one-tailed t-test
*: Voxel included in mean FA calculation was restricted using white matter mask
**: Voxel included in mean FA calculation was restricted using white matter mask and FA> 0.2
TS: Tissue-specific approach using linear registration
AT: Automated template-based approach
SB: Skeleton-based approach

9.0 DISCUSSION

9.1 EFFECT OF STRUCTURAL DAMAGE ON FUNCTIONAL ACTIVATION

The results of this functional neuroimaging study support the compensation model of cognitive aging in several ways. First, greater accuracy was associated with greater fMRI activation, mainly from ECF regions. Specifically, prefrontal cortices showed greater fMRI activation during sDSST performance with higher accuracy. Second, we found that higher WMH was associated with lower activation in regions that were also important for accuracy and that the accuracy related networks (Figure 9), seemed to partially overlap, mainly within the left hemisphere, with the networks affected by higher WMH (Figure 10). While the negative correlation of WMH measure with accuracy was expected, the association of greater WMH with lower fMRI signal within the ECF-related regions (Figure 10) is a novel finding, which indicates that WMH may be an important determinant of brain functional activation patterns and of behavioral responses. These findings indicate that WMH may affect behavioral performance through reduction of activation within regions that are important to execute this task. Thirdly, there was a significant interaction between WMH and accuracy. The study of the spatial distribution of this interaction (Figure 11 and Table 7) indicates that there is an anterior to posterior progression and that the regions showed interaction (Figure 11, Figure 12) only partially overlapped with the regions that showed a main effect of accuracy and WMH (Figure 9

and Figure 10). The significant interaction between WMH and accuracy within the left posterior parietal lobe suggests that this interference is focal and specific for ECF-networks that are not associated with the WMH burden. The processes underlying this selected spatial distribution and antero-posterior shift will need to be further investigated. Overall, our findings indicate that for greater brain damage, the activation in regions important for accurately performing the DSST decreases and activation in additional extraneous-regions increases, specifically within regions that would not routinely be recruited during this task and are spared by the WMH degenerative process as observed in the main effect analyses. Thus, higher performance in older adults may be achieved through greater and more spread brain activation to counteract greater structural abnormalities or reduced "reserve".

The activation of non-ECF regions (example, sensori-motor regions) to complete ECF tasks may also indicate a less efficient or "nonfunctional" usage of neural activation, and it is consistent with the notion of de-dedifferentiation in the older brain [30, 58, 114]. A potential additional pathway linking WMH with more diffuse activation is that increased WMH burden would lead to less activation in voxels associated with good performance at the group level and spread to other voxels. Importantly, in this study only some older adults with WMH above the median had greater performance and greater fMRI activation within the posterior parietal lobe. Future studies are needed to investigate the reasons why some older adults with WMH perform better than others. It is possible that the spatial distribution of WMH is more important than its total volume in impairing performance and brain activation. It is also possible that those with greater WMH volume and greater fMRI signal achieved greater performance because they had been exposed to other protective factors. For example, education and various lifestyle factors have been identified as surrogate markers of inherent neural resources. While the participants of

this study completed a comprehensive lifestyle factor assessment, the exploratory sub-analyses of fMRI, structural images measure, and behavioral performance for those within the intervention and control group yielded very small numbers. The small number may impair the ability to examine group differences with adequate statistical power. Future studies examining indicators of brain reserve and the spatial distribution of structural integrity in large groups of older adults are warranted to elucidate the mechanisms underlying a sustained successful performance late in age. Other abnormalities, in addition to those affecting brain connectivity, include neuronal metabolism and neurotransmission, which also need to be explored. In this fMRI study of aging, we used standard registration methods and smoothing parameters, which may be a potential limitation as some have suggested that structural variability in older adults limits the registration and can confound the interpretation of the fMRI results. One would expect this confound to lead to decreased activation in subjects with greater atrophy. In this study, we found no difference in activation that correlated atrophy index, thus we suspect that our results are not confounded by differences in brain registration. Another limitation in the study is that we have used a standard HRF for the fMRI analysis, whereas it is possible that the characteristics of the HRF are altered with age.

9.2 RELATIONSHIP OF MACRO- AND MICRO- STRUCTURAL CHANGES

The primary aim of this study was to characterize the relative sensitivities of macro-structural & micro-structural brain MRI indices in measuring cognitive aging. The study is based on an epidemiologic cohort of the oldest old. Our primary findings were that all of the measures we assessed (Atrophy index, WMH, DTI, and MTI) were significantly correlated with information

processing speed, as measured by the DSST. Further, we found that the measures were significantly correlated with each other. However, there were also independent, complimentary, components to the measures (as illustrated in Table 12, Table 13, Table 14 and Figure 13). A regression model was used to show that the white microstructural measures (MTI & DTI) accounted for the greatest independent variance in information processing speed. Thus, indicating that these measures are most sensitive to the information processing changes associated with cognitive aging.

Previous studies have shown that DTI of the white matter is a sensitive marker for age-related cognitive decline [140]. These studies have demonstrated that FA and MD correlate with cognition more strongly than T2 white matter lesion volume. Kochunov et al. [158] showed that MRI/MRS-based indices of the white matter were sensitive to processing speed decline in healthy aging individuals. Up to 58% of variability in psychomotor- processing speed and 21% of variability in the psychophysical-processing speed was explained by changes in white matter DTI measures. Schiavone et al. [157], showed that all MRI measures correlated with various cognitive measures (information processing speed, episodic memory, and executive function). The FA measure correlated most strongly with all the cognitive measures. The DTI parameters explained 45%, 33%, and 25% of the variance in cognition for information processing speed, episodic memory, and executive function, respectively.

In our study, RPH of white matter MTR and FA explained 8.4% and 0.9%, of the variance in DSST performance respectively. These percentages are notably lower than those found in some of the previous studies. We believe that this is likely due to the very tight age range in the current study (79-90 years old). The age range in the other studies ranged from 50-90 years old. Another reason why our percentages are lower could be that we focused only on

full-brain white and gray matter measures rather than regional measures as used by the other studies. A strength of our study was that we examined a variety of measures, including both gray and white matter measures using macro- and micro-structural indices.

The relatively large sample that we used allowed us to explore the effect of gender specific WMH burden and atrophy index on MRI measures and DSST relationships in normal aging. Correlations of micro-structural within the specific macro-structural burden tertiles indicate that even in individuals with a small amount of macro-structural burden, there is still a significant correlation of micro-structural indices with information processing speed. These patterns illustrate how the macro- and micro-structural indices are complementary in their associations with cognitive aging. Further studies on the progression of altered brain integrity in cognitive aging are necessary to verify these relationships.

Studies have shown a decline with aging in cognitive functions particularly dependent on white matter integrity [135, 140, 171]. This is consistent with our observation that MTI and DTI white matter measures were most strongly associated with information processing speed, a function that is dependent on white matter connectivity and complex networks [172]. The sensitive markers (MTR RPH and FA RPH) as shown in this and other studies can be useful as clinical markers and as surrogate quantitative markers in larger and multicenter studies to assess the effect of interventions on progression of age-related white matter damage. To clarify whether white matter volume loss and formation of WMH lesions precede or follow micro-structural damage, a longitudinal study is necessary. Cross-sectional studies, such as this study, are limited to characterizing the relationships between the macro- and micro- structural indices. Our results can help guide future studies in the selection of neuroimaging indices for aging populations.

9.3 COMPARISON OF DTI ANALYSIS METHODS

We have shown initial evidence that the white matter integrity measure (example, mean fractional anisotropy), obtained using automated template-based approach, shows better correlation with WMH in the oldest old. As expected, this correlation is negatively related: FA values reduce with increasing WMH lesions in older adults. The results are based on a comparison with the skeleton-based approach using empirical and simulated dataset. In this study, we have used a unique dataset of healthy older adults (80+ years). This provides subjects with various degrees of white matter damage (measured in this study as WMH), cognitive performance, gender, and other imaging measures. This work is limited to the DTI analysis of clinical datasets typically with 13 gradient directions. With no standard procedure for obtaining diffusion measures, it is important to compare results, especially in the aging population. The micro-structural measures are considered as sensitive measures of aging. So, it is very important to use a method that would measure subtle changes associated with aging. Future studies are required to understand the reason why the automated template-based approach performs better. In this study, we have used correlation coefficient and significance with WMH as an indicator of performance. Other comparison metrics can be explored [173].

Similar steps were followed for the automated template-based and skeleton-based approaches were kept very similar so that direct comparisons of their results can be made. Some of the steps in this framework can be improved. Instead of the younger adult FA template for our analysis, one could generate a study specific template using TBSS tools, or use an age-specific FA or T1-weighted template. This would improve the anatomical correspondence caused by using a “representative” template. The segmentation step can be enhanced by using multi-channel methods such as using eigen values (λ_1, λ_3) with T1-weighted image to give a better

segmentation of WM and similarly the mean diffusivity can be used for gray matter segmentation. In this study, we have used a non-linear registration method (FNIRT), which provides good registration outputs. Because of variability involved in older adults, better registration methods can be tested for to further improve results.

The results shown in Figure 14 are similar to those by Alexander et al. [170], who have shown that CSF in the ventricles have greater eigen values than gray matter and prolate or oblate white matter. The distribution of eigen values is defined as a normal distribution with a mean and standard deviation. So, in this study we assumed WMH to be normally distributed with a mean and standard deviation. Our mean eigen values for isotropic CSF are slightly different from those obtained from synthetic data by Alexander et al. [170] (normally distributed eigen values with a mean of 3200 $\mu m^2/s$ and standard deviation 100 $\mu m^2/s$). The difference may be due to various reasons. The synthetic data eigen values leads to a FA value of zero for CSF in the ventricles, but in the real data the FA values in isotropic CSF is close to zero (not exactly zero). The variation may be due to extraction of eigen values from whole-brain CSF instead of just CSF in ventricles and partly because of partial volume effects. We measured the mean and standard deviation eigen values of whole-brain normal appearing white matter and WMH, we did not separate white matter into prolate and oblate.

In this study, we used the mean and standard deviation obtained from our dataset and added noise on the existing eigen value images. However, improvements can be made to our approach for future studies. Instead of using mean and standard deviation for adding noise, monte-carlo simulation can be performed using estimates of eigen values for WMH. This would also provide a standard deviation cut-off (for normal distribution) that would differentiate between WMH and white matter and can be used as a measure to compare approaches. In this

study, we have used the eigen value images directly for adding noise. Instead of this, the DWI images can be used. This would further provide an understanding of how noise addition would propagate from DWI to FA changes. This requires future studies to investigate the contribution of noise addition to each gradient direction towards DTI measures. This comparison can be extended to other diffusion measures (such as mean diffusivity for gray and white matter) and also region specific analysis.

10.0 CONCLUSIONS AND FUTURE WORK

In recent years, medical imaging has provided insight about the brain and its various functions. Neuroimaging has progressed rapidly to help comprehend cognitive aging. The goals of this dissertation were to characterize the relationships between different functional and structural MRI markers (for example: macro-structural, micro-structural, physiologic) with respect to cognitive aging and to improve the neuroimaging toolset for oldest old. The results have provided valuable information to improve the current neurocognitive model of aging. Understanding the structural MRI indices is essential for enhancing the current model and also important for the development of better prevention and treatment strategies for cognitive aging in late-life. The structural MRI indices are related to information processing speed and related to each other. Micro-structural MRI indices of white matter integrity were shown as a strong indicator of information processing speed in the oldest old. Another important contribution is the effect of structural changes on functional activation. Apart from supporting the compensation model of aging, we have also shown that structural damage affects task-related activation pattern. The ‘resilient group’ showed additional parietal activation in order to maintain the performance. The structural damage is associated with both decreases in functional activation and different patterns of activation. This work also provides initial evidence that the mean fractional anisotropy using automated template-based approach is better than skeleton-based approach for analysis of diffusion tensor imaging.

10.1 CLAIMS REVISITED

We revisit the goals of this dissertation that were outlined in the introduction.

Aim 1: Identify and characterize the structural MRI indices associated with cognitive aging in the oldest old.

Hypothesis I: Micro- and macro-structural brain MRI markers are independently associated with DSST.

When controlled for age and gender, all the MRI measures showed significant correlations with DSST in the expected direction. For example, the relative peak height of white matter fractional anisotropy showed negative correlation with DSST and relative peak height of white matter magnetization transfer ratio showed positive correlation with DSST.

Hypothesis II: Micro- and macro-structural brain MRI markers correlated with each other.

Micro- and Macro- structural indices were significantly correlated with each when controlled for age and gender. The only exception was the relationship between gray matter magnetization transfer ratio relative peak height (MTR RPH) and white matter hyperintensities.

Hypothesis III: Microstructural brain MRI markers are better predictor of DSST independent of other MRI markers and factors.

According to plots of micro- and macro- structural measures and by using regression model, the white matter MRI micro-structural measures are the most sensitive to information processing speed changes in aging. The white matter MRI micro-structural measures (MTR RPH 8.4% and fractional anisotropy RPH 0.9%) accounted for the greatest variance of DSST. This was further verified using the gender specific tertiles. These results show the complementary information that the MRI measures provide.

Aim 2: Identify patterns of functional MR brain changes associated with cognitive aging.

Hypothesis I: In older adults with greater task performance, the greater brain activation will be associated within task-related regions.

Greater accuracy was significantly associated with greater peak fMRI activation in executive control function regions, including left prefrontal cortex and right posterior parietal cortex.

Hypothesis II: Greater brain structural abnormalities will be associated with lower activation within task-related regions.

Greater white hyperintensities was associated with lower activation within accuracy-related regions such as bilateral anterior cingulate cortex and prefrontal cortex. Associations of fMRI activation with brain atrophy were not significant.

Hypothesis III: Older adults above median WMH and greater performance ('Resilient' group) will recruit additional areas in the posterior parietal regions.

There was a significant and positive interaction between accuracy and WMH volume within specific ECF-related (left posterior parietal) and non ECF-related regions (left sensori-motor regions). In older adults with above median WMH and greater performance, greater accuracy was associated with greater bilateral activation in ECF regions (posterior parietal and cingulate cortex), which extended to sensori-motor regions.

Aim 3: To develop and improve neuroimaging toolset for MR imaging contrasts.

Objective I: Compare diffusion tensor imaging (DTI) analysis methods within groups with various degrees of macrostructural damage using empirical and simulated data in the oldest old.

We showed initial evidence that the white matter integrity measure (example, mean fractional anisotropy) obtained using automated template-based approach shows better correlation with WMH in the oldest old than the skeleton based approach.

10.2 FUTURE WORK

The major objective of this dissertation was to characterize the relationships between different functional and structural MRI markers with respect to information processing speed and compare diffusion tensor image analysis approaches. The limitations are discussed in detail in sections 9.2, 9.1 and 9.3. Some of these limitations are related to image analysis improvements needed in the geriatric population such as age-specific template. An age-specific template generated from a specific dataset or a common template would help alleviate some of the variability involved in geriatric datasets. Image analysis steps such as segmentation and registration can be improved by using multi-contrast approaches, which could improve the results in the elderly. In functional MRI analysis of the elderly, we addressed the neurovascular coupling as boxcar function instead of standard HRF. Temporal derivatives can be used in the analysis to address neurovascular coupling to aging. The current study was performed using whole-brain analysis for structural and functional MRI. Future studies are needed to explore these relationships within structural MRI markers, and between structural and functional MRI markers using regional specific MRI measures. These studies should also include physiologic measures such as parenchymal

perfusion in the analysis. The cardiometabolic and inflammatory risk factors (such as blood pressure, fasting glucose, interleukine-6), and the corresponding rate of accrual of structural abnormalities need to be further probed. Our goal to understand the structural MRI markers is limited to characterizing the relationships between the macro- and micro- structural indices using cross-sectional studies. Longitudinal studies are needed to assess the effect of interventions on progression of age-related white matter damage and to clarify whether white matter volume loss and formation of WMH lesions precede or follow micro-structural damage. Further examination of brain reserve indicators and the spatial distribution of structural integrity in large groups of elderly are warranted to elucidate the mechanisms underlying a sustained successful performance late in age. This would provide insight to the reasons why some elderly with WMH perform better than others. Longitudinal studies would provide an opportunity to inspect the progress of functional changes due to structural damage over a time period due to normal aging. This would help create a major breakthrough for modifying the current neurocognitive model. Based on the initial evidence from the comparison of DTI approaches for analyzing clinical datasets, future studies need to address the limitations addressed in section 9.3. Further studies are required to perform monte-carlo simulations to verify the current results and provide why one of the approaches performs better than the other in the aging population. Measures to compare DTI analysis approaches are required. This would also provide an understanding of parameters that can be used to differentiate between white matter and white matter hyperintensities.

BIBLIOGRAPHY

1. AOA, A Profile of Older Americans: 2009. Administration on Aging, U.S. Department of Health and Human Services, 2009.

2. Population Division of the Department of Economic and Social Affairs of the United Nations Secretariat World Population Prospects: : The 2008 Revision. http://esa.un.org/unpp.

3. He, W., et al., 65+ in the United States: 2005. U.S. Department of Health and Human Services, 2006.

4. Ahmed, N., R. Mandel, and M.J. Fain, Frailty: an emerging geriatric syndrome. Am J Med, 2007. 120(9): p. 748-53.

5. Inouye, S.K., et al., Geriatric syndromes: clinical, research, and policy implications of a core geriatric concept. J Am Geriatr Soc, 2007. 55(5): p. 780-91.

6. Reuben, D., Geriatric syndrome. In: Beck AC, ed. Geriatrics Review Syllabus. 2nd ed. New York, NY: American Geriatrics Society, 1991: p. 117-231.

7. Rowe, J.W. and R.L. Kahn, Human aging: usual and successful. Science, 1987. 237(4811): p. 143-9.

8. van Buchem, M.A., Introduction: Successful, Usual, and Pathological Aging. Top Magn Reson Imaging, 2004. 15(6): p. 341.

9. Kemper, T., Neuroanatomical and neuropathological changes during aging and dementia, in Clinical neurology of aging, M.L. Albert and J. Kusefel, Editors. 1994, Oxford: New York. p. 3-67.

10. Raz, N., et al., Selective aging of the human cerebral cortex observed in vivo: differential vulnerability of the prefrontal gray matter. Cereb Cortex, 1997. 7(3): p. 268-82.

11. Raz, N., Aging of the brain and its impact on cognitive performance: Integration of structural and functional findings., in Handbook of Aging and Cognition- II, F.I.M. Craik and T.A. Salthouse, Editors. 2008, Erlbaum: Mahwah, NJ. p. 1-90.

12. Martin, W.R., F.Q. Ye, and P.S. Allen, Increasing striatal iron content associated with normal aging. Mov Disord, 1998. 13(2): p. 281-6.

13. Schochet, S.S., Jr., Neuropathology of aging. Neurol Clin, 1998. 16(3): p. 569-80.

14. Strong, R., Neurochemical changes in the aging human brain: implications for behavioral impairment and neurodegenerative disease. Geriatrics, 1998. 53 Suppl 1: p. S9-12.

15. Wang, G.J., et al., Evaluation of age-related changes in serotonin 5-HT2 and dopamine D2 receptor availability in healthy human subjects. Life Sci, 1995. 56(14): p. PL249-53.

16. Lee, K.S., et al., In vivo quantification of cerebral muscarinic receptors in normal human aging using positron emission tomography and [11C]tropanyl benzilate. J Cereb Blood Flow Metab, 1996. 16(2): p. 303-10.

17. Dennis, N.A. and R. Cabeza, Neuroimaging of healthy cognitive aging. , in Handbook of aging and cognition, F.I.M. Craik and T.A. Salthouse, Editors. 2008, Erlbaum: Mahwah, NJ.

18. Lindenberger, U. and P.B. Baltes, Sensory functioning and intelligence in old age: a strong connection. Psychol Aging, 1994. 9(3): p. 339-55.

19. Fischer, H., et al., Age-differential patterns of brain activation during perception of angry faces. Neurosci Lett, 2005. 386(2): p. 99-104.

20. Grady, C.L., et al., Age-related changes in cortical blood flow activation during visual processing of faces and location. J Neurosci, 1994. 14(3 Pt 2): p. 1450-62.

21. Schneider, B.A., & Pichora-Fuller, M. K., Implications of perceptual deterioration for cognitive aging research. In: Handbook of Cognitive Aging II, Eds: F. I. M. Craik & T. A. Salthouse, 2000. Mahwah, NJ: Lawrence Erlbaum Associates, Inc.: p. 155-219.

22. Madden, D.J., et al., Adult age differences in regional cerebral blood flow during visual world identification: evidence from H215O PET. Neuroimage, 1996. 3(2): p. 127-42.

23. Tulving, E., Elements of Episodic Memory. Oxford University Press, New York, 1983.

24. Roediger, H.L., & McDermott, K. B. , Implicit memory in normal subjects. In H. Spinnler & Boller (Eds.), Handbook of Neuropsychology. Amsterdam: Elsevier. , 1993.

25. Zacks, R.T., Hasher, L., & Li, K. Z. H. , Human memory. In: Handbook of aging and cognition II , Eds: F. I. M. Craik & T. A. Salthouse ,Mahwah, NJ: Erlbaum, 2000: p. 293-357.

26. La Voie, D. and L.L. Light, Adult age differences in repetition priming: a meta-analysis. Psychol Aging, 1994. 9(4): p. 539-53.

27. Baddeley, A., The episodic buffer: a new component of working memory? Trends Cogn Sci, 2000. 4(11): p. 417-423.

28. Verhaeghen, P., A. Marcoen, and L. Goossens, Facts and fiction about memory aging: a quantitative integration of research findings. J Gerontol, 1993. 48(4): p. P157-71.

29. Cabeza, R., et al., Task-independent and task-specific age effects on brain activity during working memory, visual attention and episodic retrieval. Cereb Cortex, 2004. 14(4): p. 364-75.

30. Baltes, P.B. and U. Lindenberger, Emergence of a powerful connection between sensory and cognitive functions across the adult life span: a new window to the study of cognitive aging? Psychol Aging, 1997. 12(1): p. 12-21.

31. Kahneman, D., Attention and effort. Prentice-Hall, Englewood Cliffs, NJ, 1973.

32. Craik, F.I.M., A functional account of age differences in memory. In: Human memory and cognitive capabilities: Mechanisms and performances, Eds:F. Klix& H. Hagendorf, Amsterdam: Elsevier, 1986: p. 409-422.

33. Anderson, N.D., F.I. Craik, and M. Naveh-Benjamin, The attentional demands of encoding and retrieval in younger and older adults: 1. Evidence from divided attention costs. Psychol Aging, 1998. 13(3): p. 405-23.

34. Salthouse, T.A., The role of memory in the age decline in digit-symbol substitution performance. J Gerontol, 1978. 33(2): p. 232-8.

35. Salthouse, T.A., The processing-speed theory of adult age differences in cognition. Psychol Rev, 1996. 103(3): p. 403-28.

36. Salthouse, T.A., Aging and measures of processing speed. Biol Psychol, 2000. 54(1-3): p. 35-54.

37. Kail, R. and T.A. Salthouse, Processing speed as a mental capacity. Acta Psychologica, 1994. 86: p. 199-255.

38. Birren, J.E., Translations in gerontology--from lab to life. Psychophysiology and speed of response. Am Psychol, 1974. 29(11): p. 808-15.

39. Salthouse, T.A., Age and memory: Strategies for localizing the loss., in New directions in memory and aging, L.W. Poon, et al., Editors. 1980, Erlbaum: Hillsdale, NJ.

40. Salthouse, T.A. and R.L. Babcock, Decomposing adult age differences in working memory. . Developmental Psychology, 1991. 27: p. 763-776.

41. Salthouse, T.A., Mechanisms of age-cognition relations in adulthood. 1992, Erlbaum: Hillsdale, NJ.

42. Schaie, K.W. and S.L. Willis, Age difference patterns of psychometric intelligence in adulthood: generalizability within and across ability domains. Psychol Aging, 1993. 8(1): p. 44-55.

43. Salthouse, T.A. and E. Ferrer-Caja, What needs to be explained to account for age-related effects on multiple cognitive variables? Psychology and Aging, 2003. 18: p. 91-110.

44. Finkel, D., et al., Age changes in processing speed as a leading indicator of cognitive aging. Psychology and Aging, 2007. 22(3): p. 558-568.

45. Lemke, U. and D. Zimprich, Longitudinal changes in memory performance and processing speed in old age. Aging, Neuropsychology and Cognition, 2007. 12: p. 57-77.

46. Madden, D.J., Speed and timing of behavioral processes, in Handbook of the psychology of aging, J.E. Birren and K.W. Schaie, Editors. 2001.

47. Deary, I.J., W. Johnson, and J.M. Starr, Are processing speed tasks biomarkers of cognitive aging? Psychol Aging, 2010. 25(1): p. 219-28.

48. Deary, I.J., Looking down on human intelligence: From psychometrics to the brain. Oxford, United Kingdom: Oxford University Press, 2000.

49. Grudnik, J.L. and J.H. Kranzler, Meta-analysis of the relationship between intelligence and inspection time. Intelligence, 2001. 29: p. 523-535.

50. Salthouse, T.A., Mediation of adult age differences in cognition by reductions in working memory and speed of processing. Psychological Science, 1991. 2: p. 179-183.

51. Wechsler, D., Wechsler Adult Intelligence Scale - Revised Manual. New York: Psychological Corporation, 1981.

52. Matarazzo, J.D. and D.O. Herman, Base rate data for the WAIS-R: test-retest stability and VIQ-PIQ differences. J Clin Neuropsychol, 1984. 6(4): p. 351-66.

53. Rosano, C., et al., Association between lower digit symbol substitution test score and slower gait and greater risk of mortality and of developing incident disability in well-functioning older adults. J Am Geriatr Soc, 2008. 56(9): p. 1618-25.

54. Cabeza, R., Neuroscience Frontiers of Cognitive Aging: Approaches to Cognitive Neuroscience of Aging, in New frontiers in cognitive aging, R.A. Dixon, L. Backman, and L.G. Nilsson, Editors. 2004, Oxford University Press.

55. Prull, M.W., J.D.E. Gabrieli, and S.A. Bunge, Memory and aging: A cognitive neuroscience perspective, in Handbook of Aging and Cognition- II, F.I.M. Craik and T.A. Salthouse, Editors. 2000, Erlbaum: Mahwah, NJ.

56. Gunning-Dixon, F.M. and N. Raz, Neuroanatomical correlates of selected executive functions in middle-aged and older adults: a prospective MRI study. Neuropsychologia, 2003. 41(14): p. 1929-41.

57. Cabeza, R., Cognitive neuroscience of aging: contributions of functional neuroimaging. Scand J Psychol, 2001. 42(3): p. 277-86.

58. Cabeza, R., Hemispheric asymmetry reduction in older adults: the HAROLD model. Psychol Aging, 2002. 17(1): p. 85-100.

59. Grady, C.L., Cognitive neuroscience of aging. Ann N Y Acad Sci, 2008. 1124: p. 127-44.

60. Venkatraman, V.K., et al., Executive control function, brain activation and white matter hyperintensities in older adults. Neuroimage, 2010. 49(4): p. 3436-42.

61. Damoiseaux, J.S., et al., Reduced resting-state brain activity in the "default network" in normal aging. Cereb Cortex, 2008. 18(8): p. 1856-64.

62. Backman, L., et al., The correlative triad among aging, dopamine, and cognition: Current status and future prospects. Neuroscience & Biobehavioral Reviews, 2006. 30: p. 791-807.

63. Braver, T.S., et al., Flexible neural mechanisms of cognitive control within human prefrontal cortex. Proc Natl Acad Sci U S A, 2009. 106(18): p. 7351-6.

64. Reuter-Lorenz, P.A. and K. Cappell, Neurocognitive aging and the compensation hypothesis. Current Directions in Psychological Science, 2008. 18: p. 177-182.

65. Park, D.C. and P. Reuter-Lorenz, The adaptive brain: aging and neurocognitive scaffolding. Annu Rev Psychol, 2009. 60: p. 173-96.

66. Reuter-Lorenz, P.A. and D.C. Park, Human neuroscience and the aging mind: a new look at old problems. J Gerontol B Psychol Sci Soc Sci, 2010. 65(4): p. 405-15.

67. Liang, Z.P. and P.C. Lauterbur, Principles of Magnetic Resonance Imaging: A Signal Processing Perspectve. 2000: IEEE Press.

68. Mitchell, D.G., MRI Principles. 1999: Elsevier.

69. Dolan, R.J., Neuroimaging of cognition: past, present, and future. Neuron, 2008. 60(3): p. 496-502.

70. Brant-Zawadzki, M., G.D. Gillan, and W.R. Nitz, MP RAGE: a three-dimensional, T1-weighted, gradient-echo sequence--initial experience in the brain. Radiology, 1992. 182(3): p. 769-75.

71. Mugler, J.P., 3rd and J.R. Brookeman, Three-dimensional magnetization-prepared rapid gradient-echo imaging (3D MP RAGE). Magn Reson Med, 1990. 15(1): p. 152-7.

72. De Coene, B., et al., MR of the brain using fluid-attenuated inversion recovery (FLAIR) pulse sequences. Am J Neuroradiol., 1992. 13: p. 1555-1564.

73. Wolff, S.D. and R.S. Balaban, Magnetization transfer imaging: practical aspects and clinical applications. Radiology, 1994. 192(3): p. 593-9.

74. Tofts, P.S., S.C.A. Steens, and M.A. van Buchem, MT: Magnetization Transfer, in Quantitative MR I of the B r ain: Measuring Changes Caused by Disease, P.S. Tofts, Editor. 2003, John Wiley & Sons, Ltd.

75. Henkelman, R.M., G.J. Stanisz, and S.J. Graham, Magnetization transfer in MRI: a review NMR Biomed, 2001. 14: p. 57-64.

76. Basser, P.J., J. Mattiello, and D. LeBihan, Estimation of the effective self-diffusion tensor from the NMR spin echo. J Magn Reson B, 1994. 103(3): p. 247-54.

77. Pierpaoli, C., et al., Diffusion tensor MR imaging of the human brain. Radiology, 1996. 201(3): p. 637-48.

78. Wheeler-Kingshott, C.A.M., et al., D: the Diffusion of Water, in Quantitative MR I of the B r ain: Measuring Changes Caused by Disease., P.S. Tofts, Editor. 2003, John Wiley & Sons,Ltd.

79. Hagmann, P., et al., Understanding diffusion MR imaging techniques: from scalar diffusion-weighted imaging to diffusion tensor imaging and beyond. Radiographics, 2006. 26 Suppl 1: p. S205-23.

80. Mukherjee, P., et al., Diffusion tensor MR imaging and fiber tractography: theoretic underpinnings. AJNR Am J Neuroradiol, 2008. 29(4): p. 632-41.

81. Buxton, R.B., Introduction to functional magnetic resonance imaging: principles and techniques. 2002: Cambridge University Press.

82. Friston, K., et al., Statistical Parametric Mapping: The Analysis of Functional Brain Images. 2006: Academic Press.

83. Ogawa, S., et al., Brain magnetic resonance imaging with contrast dependent on blood oxygenation. Proc Natl Acad Sci U S A, 1990. 87(24): p. 9868-72.

84. D'Esposito, M., E. Zarahn, and G.K. Aguirre, Event-related functional MRI: implications for cognitive psychology. Psychol Bull, 1999. 125(1): p. 155-64.

85. Friston, K.J., et al., Stochastic designs in event-related fMRI. Neuroimage, 1999. 10(5): p. 607-19.

86. Detre, J.A., et al., Perfusion imaging. Magn Reson Med, 1992. 23(1): p. 37-45.

87. Yoo, T.S., Insight into images: principles and practice for segmentation, registration, and image analysis. 2004: A.K.Peters.

88. Duncan, J.S. and N. Ayache, Medical Image Analysis: Progress over Two Decades and the Challenges Ahead. IEEE Trans on Pattern Analysis and Machine Intelligence, 2000. 22(1): p. 85-106.

89. Inglese, M. and Y. Ge, Quantitative MRI: hidden age-related changes in brain tissue. Topics in Magnetic Resonance Imaging, 2004. 15(6): p. 355-63.

90. Armitage, P., J.N.S. Matthews, and G. Berry, Statistical Methods in Medical Research. 2001, Oxford: Blackwell.

91. Cox, R.W., AFNI: software for analysis and visualization of functional magnetic resonance neuroimages. Comput Biomed Res, 1996. 29(3): p. 162-73.

92. Smith, S.M., et al., Advances in functional and structural MR image analysis and implementation as FSL. Neuroimage, 2004. 23 Suppl 1: p. S208-19.

93. Woods, R.P., et al., Automated Image Registration: I. General Methods and Intrasubject, Intramodality Validation. Journal of Computer Assisted Tomography, 1998. 22(1): p. 139-152.

94. Friston, K.J., et al., Statistical parametric maps in functional imaging: A general linear approach. Human Brain Mapping, 1994. 2(4): p. 189-210.

95. Wu, M., et al., Quantitative comparison of AIR, SPM, and the fully deformable model for atlas-based segmentation of functional and structural MR images. Hum Brain Mapp, 2006. 27(9): p. 747-54.

96. Aizenstein, H.J., et al., The BOLD hemodynamic response in healthy aging. J Cogn Neurosci, 2004. 16(5): p. 786-93.

97. Morcom, A.M., et al., Age effects on the neural correlates of successful memory encoding. Brain, 2003. 126(Pt 1): p. 213-29.

98. Aizenstein, H.J., et al., Prefrontal and striatal activation in elderly subjects during concurrent implicit and explicit sequence learning. Neurobiol Aging, 2006. 27(5): p. 741-51.

99. Ashburner, J. and K.J. Friston, Why voxel-based morphometry should be used. Neuroimage, 2001. 14(6): p. 1238-43.

100. Wu, M., et al., A fully automated method for quantifying and localizing white matter hyperintensities on MR images. Psychiatry Res, 2006. 148(2-3): p. 133-42.

101. Udupa, J.K. and S. Samarasekera, Fuzzy Connectedness and Object Definition: Theory, Algorithms, and Applications in Image Segmentation Graphical Models and Image Processing, 1996. 58(3): p. 246-261.

102. Mukherjee, P., et al., Diffusion tensor MR imaging and fiber tractography: technical considerations. AJNR Am J Neuroradiol, 2008. 29(5): p. 843-52.

103. Lehmbeck, J.T., et al., Combining voxel-based morphometry and diffusion tensor imaging to detect age-related brain changes. Neuroreport, 2006. 17(5): p. 467-70.

104. Lee, J.E., et al., A study of diffusion tensor imaging by tissue-specific, smoothing-compensated voxel-based analysis. Neuroimage, 2009. 44(3): p. 870-83.

105. Smith, S.M., et al., Tract-based spatial statistics: voxelwise analysis of multi-subject diffusion data. Neuroimage, 2006. 31(4): p. 1487-505.

106. Correia, S., et al., Quantitative tractography metrics of white matter integrity in diffusion-tensor MRI. Neuroimage, 2008. 42(2): p. 568-81.

107. Pereira, F., T. Mitchell, and M. Botvinick, Machine learning classifiers and fMRI: a tutorial overview. Neuroimage, 2009. 45(1 Suppl): p. S199-209.

108. Calautti, C., C. Serrati, and J.C. Baron, Effects of age on brain activation during auditory-cued thumb-to-index opposition: A positron emission tomography study. Stroke, 2001. 32(1): p. 139-46.

109. Heuninckx, S., et al., Neural basis of aging: the penetration of cognition into action control. J Neurosci, 2005. 25(29): p. 6787-96.

110. Mattay, V.S., et al., Neurophysiological correlates of age-related changes in human motor function. Neurology, 2002. 58(4): p. 630-5.

111. Persson, J., et al., Selection requirements during verb generation: differential recruitment in older and younger adults. Neuroimage, 2004. 23(4): p. 1382-90.

112. Rosano, C., et al., Functional neuroimaging indicators of successful executive control in the oldest old. Neuroimage, 2005. 28(4): p. 881-9.

113. Ward, N.S. and R.S. Frackowiak, Age-related changes in the neural correlates of motor performance. Brain, 2003. 126(Pt 4): p. 873-88.

114. Cabeza, R., et al., Aging gracefully: compensatory brain activity in high-performing older adults. Neuroimage, 2002. 17(3): p. 1394-402.

115. Reuter-Lorenz, P.A. and C. Lustig, Brain aging: reorganizing discoveries about the aging mind. Curr Opin Neurobiol, 2005. 15(2): p. 245-51.

116. Grady, C.L., Introduction to the special section on aging, cognition, and neuroimaging. Psychol Aging, 2002. 17(1): p. 3-6.

117. McIntosh, A.R., et al., Recruitment of unique neural systems to support visual memory in normal aging. Curr Biol, 1999. 9(21): p. 1275-8.

118. Reuter-Lorenz, P.A., Neurocognitive ageing of storage and executive processes. Eur. J Cogn. Psychol., 2001. 13: p. 257-278.

119. Grady, C.L., et al., Effect of task difficulty on cerebral blood flow during perceptual matching of faces. Hum Brain Mapp, 1996. 4(4): p. 227-39.

120. Rypma, B. and M. D'Esposito, The roles of prefrontal brain regions in components of working memory: effects of memory load and individual differences. Proc Natl Acad Sci U S A, 1999. 96(11): p. 6558-63.

121. Langenecker, S.A., K.A. Nielson, and S.M. Rao, fMRI of healthy older adults during Stroop interference. Neuroimage, 2004. 21(1): p. 192-200.

122. Persson, J. and L. Nyberg, Altered brain activity in healthy seniors: what does it mean? Prog Brain Res, 2006. 157: p. 45-56.

123. Persson, J., et al., Structure-function correlates of cognitive decline in aging. Cereb Cortex, 2006. 16(7): p. 907-15.

124. Gunning-Dixon, F.M. and N. Raz, The cognitive correlates of white matter abnormalities in normal aging: a quantitative review. Neuropsychology, 2000. 14(2): p. 224-32.

125. Brassen, S., et al., Structure-function interactions of correct retrieval in healthy elderly women. Neurobiol Aging, 2009. 30(7): p. 1147-56.

126. Nordahl, C.W., et al., White matter changes compromise prefrontal cortex function in healthy elderly individuals. J Cogn Neurosci, 2006. 18(3): p. 418-29.

127. Marner, L., et al., Marked loss of myelinated nerve fibers in the human brain with age. J Comp Neurol, 2003. 462(2): p. 144-52.

128. Meier-Ruge, W., et al., Age-related white matter atrophy in the human brain. Ann N Y Acad Sci, 1992. 673: p. 260-9.

129. Resnick, S.M., et al., Longitudinal magnetic resonance imaging studies of older adults: a shrinking brain. J Neurosci, 2003. 23(8): p. 3295-301.

130. Rovaris, M., et al., Age-related changes in conventional, magnetization transfer, and diffusion-tensor MR imaging findings: study with whole-brain tissue histogram analysis. Radiology, 2003. 227(3): p. 731-8.

131. Ge, Y., et al., Age-related total gray matter and white matter changes in normal adult brain. Part I: volumetric MR imaging analysis. AJNR Am J Neuroradiol, 2002. 23(8): p. 1327-33.

132. Le Bihan, D., et al., MR imaging of intravoxel incoherent motions: application to diffusion and perfusion in neurologic disorders. Radiology, 1986. 161: p. 401-407.

133. Bhagat, Y.A. and C. Beaulieu, Diffusion anisotropy in subcortical white matter and cortical gray matter: changes with aging and the role of CSF-suppression. J Magn Reson Imaging, 2004. 20(2): p. 216-27.

134. Pierpaoli, C. and P.J. Basser, Toward a quantitative assessment of diffusion anisotropy. Magn Reson Med, 1996. 36(6): p. 893-906.

135. Charlton, R.A., et al., White matter damage on diffusion tensor imaging correlates with age-related cognitive decline. Neurology, 2006. 66(2): p. 217-22.

136. Jones, D.K., et al., Characterization of white matter damage in ischemic leukoaraiosis with diffusion tensor MRI. Stroke, 1999. 30(2): p. 393-7.

137. Kochunov, P., et al., Can structural MRI indices of cerebral integrity track cognitive trends in executive control function during normal maturation and adulthood? Hum Brain Mapp, 2009. 30(8): p. 2581-94.

138. Kochunov, P., et al., Relationship among neuroimaging indices of cerebral health during normal aging. Hum Brain Mapp, 2008. 29(1): p. 36-45.

139. Salat, D.H., et al., Age-related alterations in white matter microstructure measured by diffusion tensor imaging. Neurobiol Aging, 2005. 26(8): p. 1215-27.

140. Deary, I.J., et al., White matter integrity and cognition in childhood and old age. Neurology, 2006. 66(4): p. 505-12.

141. Filippi, M., et al., A magnetization transfer imaging study of normal-appearing white matter in multiple sclerosis. Neurology, 1995. 45(3 Pt 1): p. 478-82.

142. Ge, Y., et al., Age-related total gray matter and white matter changes in normal adult brain. Part II: quantitative magnetization transfer ratio histogram analysis. AJNR Am J Neuroradiol, 2002. 23(8): p. 1334-41.

143. van der Flier, W.M., et al., Magnetization transfer imaging in normal aging, mild cognitive impairment, and Alzheimer's disease. Annals of Neurology, 2002. 52(1): p. 62-7.

144. Filippi, M., et al., Changes in the normal appearing brain tissue and cognitive impairment in multiple sclerosis. Journal of Neurology, Neurosurgery & Psychiatry, 2000. 68(2): p. 157-61.

145. Pantoni, L. and J.H. Garcia, The significance of cerebral white matter abnormalities 100 years after Binswanger's report. A review. Stroke, 1995. 26(7): p. 1293-301.

146. de Leeuw, F.E., et al., Prevalence of cerebral white matter lesions in elderly people: a population based magnetic resonance imaging study. The Rotterdam Scan Study. J Neurol Neurosurg Psychiatry, 2001. 70(1): p. 9-14.

147. Du, A.T., et al., White matter lesions are associated with cortical atrophy more than entorhinal and hippocampal atrophy. Neurobiol Aging, 2005. 26(4): p. 553-9.

148. Sachdev, P. and H. Brodaty, Quantitative study of signal hyperintensities on T2-weighted magnetic resonance imaging in late-onset schizophrenia. Am J Psychiatry, 1999. 156(12): p. 1958-67.

149. Esposito, G., et al., Context-dependent, neural system-specific neurophysiological concomitants of ageing: mapping PET correlates during cognitive activation. Brain, 1999. 122 (Pt 5): p. 963-79.

150. Grady, C.L., A.R. McIntosh, and F.I. Craik, Age-related differences in the functional connectivity of the hippocampus during memory encoding. Hippocampus, 2003. 13(5): p. 572-86.

151. Kennedy, K.M. and N. Raz, Pattern of normal age-related regional differences in white matter microstructure is modified by vascular risk. Brain Res, 2009. 1297: p. 41-56.

152. Raz, N., et al., Vascular health and longitudinal changes in brain and cognition in middle-aged and older adults. Neuropsychology, 2007. 21(2): p. 149-57.

153. Sullivan, E.V. and A. Pfefferbaum, Diffusion tensor imaging and aging. Neurosci Biobehav Rev, 2006. 30(6): p. 749-61.

154. Span, M.M., K.R. Ridderinkhof, and M.W. van der Molen, Age-related changes in the efficiency of cognitive processing across the life span. Acta Psychol (Amst), 2004. 117(2): p. 155-83.

155. Benedetti, B., et al., Influence of aging on brain gray and white matter changes assessed by conventional, MT, and DT MRI. Neurology, 2006. 66(4): p. 535-9.

156. Charlton, R.A., McIntyre, D.J.O., Howe,F.A., Morris, R.G., Markus,H.S., The relationship between white matter brain metabolites and cognition in normal aging: The GENIE study. Brain Research, 2007. 1164: p. 108-116.

157. Schiavone, F., Charlton,R.A., Barrick,T.R., Morris, R.G.,Markus, H.S., Imaging Age-Related Cognitive Decline: A Comparison of Diffusion Tensor and Magnetization Transfer MRI. Journal of Magnetic Resonance Imaging, 2009. 29: p. 23-30.

158. Kochunov, P., et al., Processing speed is correlated with cerebral health markers in the frontal lobes as quantified by neuroimaging. Neuroimage, 2010. 49(2): p. 1190-9.

159. Burgmans, S., et al., Multiple indicators of age-related differences in cerebral white matter and the modifying effects of hypertension. Neuroimage, 2010. 49: p. 2083-2093.

160. Ceritoglu, C., et al., Multi-contrast large deformation diffeomorphic metric mapping for diffusion tensor imaging. Neuroimage, 2009. 47(2): p. 618-27.

161. Charlton, R.A., et al., Diffusion tensor imaging detects age related white matter change over a 2 year follow-up which is associated with working memory decline. J Neurol Neurosurg Psychiatry, 2010. 81(1): p. 13-9.

162. Pahor, M., et al., Effects of a physical activity intervention on measures of physical performance: Results of the lifestyle interventions and independence for Elders Pilot (LIFE-P) study. J Gerontol A Biol Sci Med Sci, 2006. 61(11): p. 1157-65.

163. Rosano, C., et al., Morphometric analysis of gray matter volume in demented older adults: exploratory analysis of the cardiovascular health study brain MRI database. Neuroepidemiology, 2005. 24(4): p. 221-9.

164. Zandbelt, B.B., et al., Within-subject variation in BOLD-fMRI signal changes across repeated measurements: quantification and implications for sample size. Neuroimage, 2008. 42(1): p. 196-206.

165. Maldjian, J.A., et al., An automated method for neuroanatomic and cytoarchitectonic atlas-based interrogation of fMRI data sets. Neuroimage, 2003. 19(3): p. 1233-9.

166. Jenkinson, M., M. Pechaud, and S. Smith. BET2: MR-based estimation of brain, skull and scalp surfaces. in Eleventh Annual Meeting of the Organization for Human Brain Mapping. 2005. Toronto.

167. Zhang, Y., M. Brady, and S. Smith, Segmentation of brain MR images through a hidden Markov random field model and the expectation maximization algorithm. IEEE Trans Med Imaging, 2001. 20(1): p. 45-57.

168. Andersson, J.L.R., M. Jenkinson, and S. Smith, Non-linear registration, aka Spatial normalisation. 2007.

169. Wakana, S., et al., Reproducibility of quantitative tractography methods applied to cerebral white matter. Neuroimage, 2007. 36(3): p. 630-44.

170. Alexander, D.C., et al., Spatial transformations of diffusion tensor magnetic resonance images. IEEE Trans Med Imaging, 2001. 20(11): p. 1131-9.

171. O'Sullivan, M., et al., Evidence for cortical "disconnection" as a mechanism of age-related cognitive decline. Neurology, 2001. 57(4): p. 632-8.

172. Snyder, P.J. and J.C. Cappelleri, Information processing speed deficits may be better correlated with the extent of white matter sclerotic lesions in multiple sclerosis than previously suspected. Brain Cogn, 2001. 46(1-2): p. 279-84.

173. Heiervang, E., et al., Between session reproducibility and between subject variability of diffusion MR and tractography measures. Neuroimage, 2006. 33(3): p. 867-77.